Potential Detectability of Gamma-Ray Halos Around Spiral Galaxies

Master's Thesis in Physics

submitted by

Mario Engelmann

Date: November 15, 2023

Erlangen Centre for Astroparticle Physics
Department of Physics
Friedrich-Alexander-Universität Erlangen-Nürnberg

Supervisor: Dr. Alison Mitchell

Abstract

Evidence found in 2019 points to a gamma-ray halo around our nearest neighbouring galaxy, the Andromeda Galaxy. Two hypotheses for the halo origin are being discussed: either it is the result of cosmic rays interacting with the surrounding medium to produce gamma rays, or the self-annihilation of weakly interacting massive particles, a candidate for dark matter.

In this work, data from the Andromeda Galaxy collected by Fermi-LAT, a gamma-ray detection satellite, are analysed. The halo of the Andromeda Galaxy is modelled with different spectral models, a power law, a power law with exponential cutoff and a log parabola. A flat disk is assumed as the halo's morphology. It is shown that the best fitting spectral model is the log parabola model. The extracted flux points agree well at low energies ($< 10\,\mathrm{GeV}$), but deviate from the model at higher energies in the order of about 10^2. The flux points are compared with the two proposed gamma-ray origin models, cosmic rays and dark matter, showing that they can explain the observed phenomenon of the halo.

Afterwards, sensitivity curves for different neighbouring galaxies are estimated for Fermi-LAT and the future CTA experiment, a ground-based gamma-ray detector. The fluxes for different neighbouring galaxies are predicted. For CTA, it is not feasible to detect the halo structure for neighbouring galaxies, since the predicted fluxes are at least an order of 10^2 smaller than the predicted sensitivity curve, for an observation time of 100 h. However, the sensitivity estimation of Fermi-LAT lead to one candidate, the Triangulum Galaxy, with a detectable flux, at the lower energies.

An analysis of the gamma-ray data of the Triangulum Galaxy collected by Fermi-LAT is carried out. The logarithmic parabola spectral model with a flat disc as morphology is chosen as the halo model. The analysis of the cosmic ray origin of the halo of the Triangulum Galaxy is inconclusive, because of the low statistic of the source galaxy. The gamma-ray spectrum resulting from the dark matter annihilation was quantitatively compared to the flux points extracted from the log parabola model. The models show similar spectral shapes.

Zusammenfassung

Die 2019 gefundenen Beweise deuten auf einen Gammastrahlen-Halo um unsere nächste Nachbargalaxie, die Andromeda-Galaxie, hin. Zwei Hypothesen für den Ursprung des Halos werden diskutiert: entweder ist er das Ergebnis kosmischer Strahlung, die mit dem umgebenden Medium wechselwirkt und dabei Gammastrahlen erzeugt, oder das Ergebnis der Selbstvernichtung schwach wechselwirkender massiver Teilchen, ein Kandidat für dunkle Materie.

In dieser Arbeit werden Daten aus der Andromedagalaxie analysiert, die von Fermi-LAT, einem Gammastrahlensatelliten, gesammelt wurden. Der Halo der Andromeda-Galaxie wird mit verschiedenen Spektralmodellen modelliert, einem Power-Law, einem Power-Law mit Exponential-Cutoff und einer Log-Parabola. Als Morphologie des Halos wird eine flache Scheibe angenommen. Es wird gezeigt, dass das Log-Parabola-Spektralmodell am besten passt. Die extrahierten Flux-Points stimmen bei niedrigen Energien ($< 10\,\mathrm{GeV}$) gut überein, weichen aber bei höheren Energien in der Größenordnung von etwa 10^2 vom Modell ab. Die Flux-Points werden mit den beiden vorgeschlagenen Ursprungsmodellen der Gammastrahlung, der kosmischen Strahlung und der dunklen Materie, verglichen und zeigen, dass sie das beobachtete Phänomen des Halos erklären können.

Anschließend werden Sensitivity-Curves für verschiedene benachbarte Galaxien für Fermi-LAT und das zukünftige CTA-Experiment, einen bodengestützten Gammastrahlendetektor, abgeschätzt. Die Teilchenflüsse für verschiedene benachbarte Galaxien werden vorhergesagt. Für CTA ist es nicht möglich, die Halostruktur für benachbarte Galaxien zu erkennen, da die vorhergesagten Teilchenflüsse mindestens eine Größenordnung von 10^2 kleiner sind als die vorhergesagte Sensitivity-Curves für eine Beobachtungszeit von 100 h. Die Sensitivity-Curves Abschätzung von Fermi-LAT führte jedoch zu einem Kandidaten, der Triangulum-Galaxie, mit einem nachweisbaren Teilchenfluss bei den niedrigen Energien.

Eine Analyse der von Fermi-LAT gesammelten Gammastrahlendaten der Triangulum-Galaxie wird durchgeführt. Das Log-Parabola-Spektralmodell mit einer flachen Scheibe als Morphologie wird als Halo-Modell gewählt. Die Analyse des kosmischen Strahlungsursprungs des Halos der Triangulum-Galaxie ist aufgrund der niedrigen Statistik der Quellgalaxie nicht schlüssig. Das Gammastrahlenspektrum, das aus der Annihilation der dunklen Materie resultiert, wurde quantitativ mit den aus dem Log-Parabola-Spektralmodell extrahierten Flusspunkten verglichen. Die Modelle zeigen ähnliche Spektralformen.

Contents

Chapter 1

Introduction

One of the largest scaled structures in the universe are galaxies. Galaxies are a collection of stars, which are bound by gravity, due to their masses. Nevertheless, there is a problem: observations predict a higher mass for galaxies than would be assumed on the basis of visible matter. Therefore, several theories are developed to account for additional non-visible matter. These theories are referred to as dark matter (DM) theories, because they predict particles, which barely interact electromagnetically.

Galaxies are complex systems that are not yet fully understood. By observing their radiation, scientists try to understand them better. Additionally, cosmic rays (CR), which consist of protons, nuclei and electrons, can be studied. CRs travel through the universe and can even leave their origin galaxy. The CRs are charged and make the path reconstruction impossible, because they get deflected by magnetic fields. Also, CR can interact with their surrounding medium and produce radiation. Especially, photons at the highest energies, the so-called gamma rays with energies higher than 100 keV, describe the most extreme phenomena. Because photons are neutral, they can also be used to infer back to their origin. Likewise, the above-mentioned DM theories predict gamma-ray emission. There are two different methods for detecting gamma rays, ground-based and space-based telescopes. One can either measure them directly with space-based telescopes or indirectly by detecting interaction results from gamma rays interacting in the atmosphere with ground-based telescopes.

Recent evidence suggests that our neighbouring galaxy, the Andromeda Galaxy (M31), is surrounded by a gamma-ray halo [1]. The Andromeda Galaxy is a spiral galaxy, which is our closest neighbouring galaxy with a distance of 2 500 000 ly or 770 kpc, with a mass of $2.5 \times 10^{12}\,\mathrm{M}_{\odot}$. The Andromeda Galaxy resembles our own galaxy, the Milky Way, and they are both estimated to collide in about 5 Gyr [2]. In the paper, the halo is divided into three parts. Firstly, the inner galaxy, which resembles a circle with a radius of ~ 5.5 kpc centred around M31's centre. Secondly, the spherical halo (SH), resembling a ring extending from ~ 5.5 kpc to ~ 120 kpc. Lastly, the outer halo describes the remainder region up to a distance of ~ 200 kpc. In Figure 1.1 a schematic representation of the halo structure of the Andromeda Galaxy defined in Karwin et al. 2019 is shown.

Two ideas are proposed for explaining the halo. In the first case, the halo is a result of the CRs diffusing from the galaxy. During this diffusion process, protons or electrons interact with the surrounding medium and generate gamma rays through various interaction mechanisms. In the second case, DM was used as a possible ex-

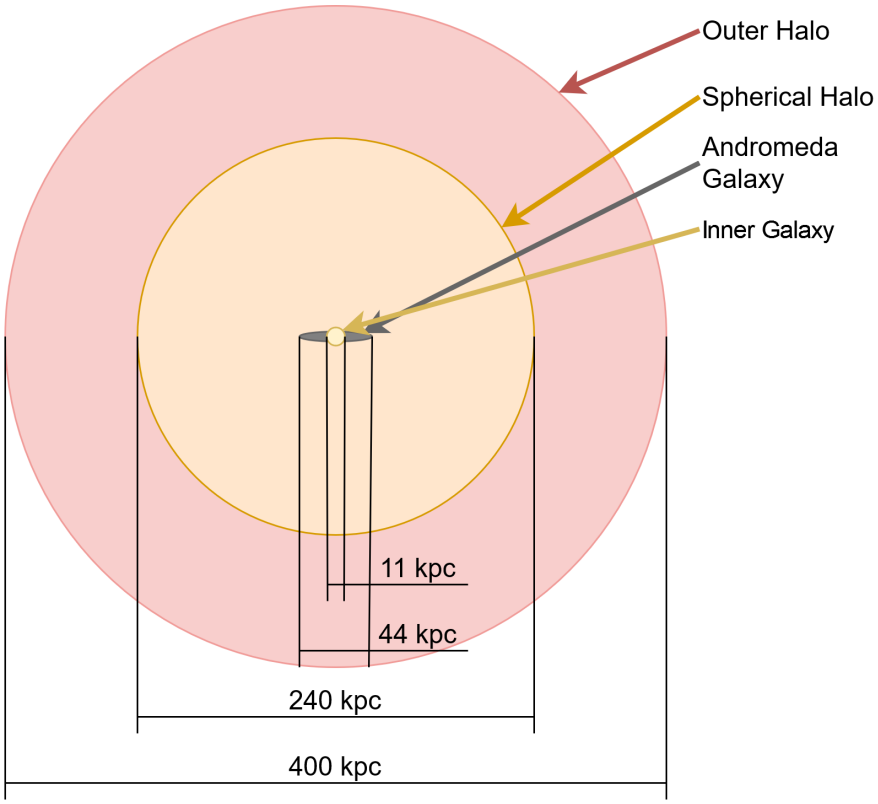

Figure 1.1: Schematic representation of the halo structure of the Andromeda Galaxy defined in Karwin et al. 2019.

planation. The DM theory of weakly interactive massive particles (WIMPs) predicts gamma rays, resulting from their annihilation.

To this day, the exact mechanism, which produces the halo, is not fully understood, let alone which of the previous mentioned cases is the origin. Also, it is unknown if this is a feature of the Andromeda Galaxy or if it is a general phenomenon for galaxies, which are similar to the Andromeda Galaxy.

In this work, I will focus on the SH of the Andromeda Galaxy and try to gain a deeper understanding of this phenomenon. By using data, which is collected by the Fermi-LAT detector, the gamma-ray emission is modelled and compared to two potential origins. Following this, the knowledge obtained is applied to M31-like galaxies in the local neighbourhood.

In this thesis, I will firstly explain the basic theory of gamma rays in chapter 2, how they are produced and how to detect them. Afterwards, I will introduce theoretical background of galaxies and cosmic rays and show first simulation results in chapter 3. Then, the dark matter theory, the second potential gamma-ray halo origin, is discussed, where I also show first simulation results in chapter 4. In the next part chapter 5, the SH of the Andromeda Galaxy is modelled with the data from Fermi-LAT and compared to the previous CR and DM models. Additionally, in chapter 6, potential galaxy candidates in the local neighbourhood are selected and also analysed. Finally, in the last chapter (chapter 7) a summary is provided, and I will draw my conclusions.

Chapter 2

Gamma Rays

To gain deeper insights into the functionality of galaxies or stars, astrophysicists analyse electromagnetic radiation in specific energy bands, e.g. gamma-rays ($E > 100\,\mathrm{keV}$). In contrast to charged CRs, they are unaffected by ambient magnetic fields. Thus, their trajectory traces back to the source of the emission.
Recently, a gamma ray halo around the Andromeda Galaxy was observed [1], which emits gamma rays in the range of roughly 1 GeV to 100 GeV. In this chapter, the most common gamma-ray production mechanisms, the detection of gamma rays and lastly the technical details of the detectors relevant for the thesis are discussed.

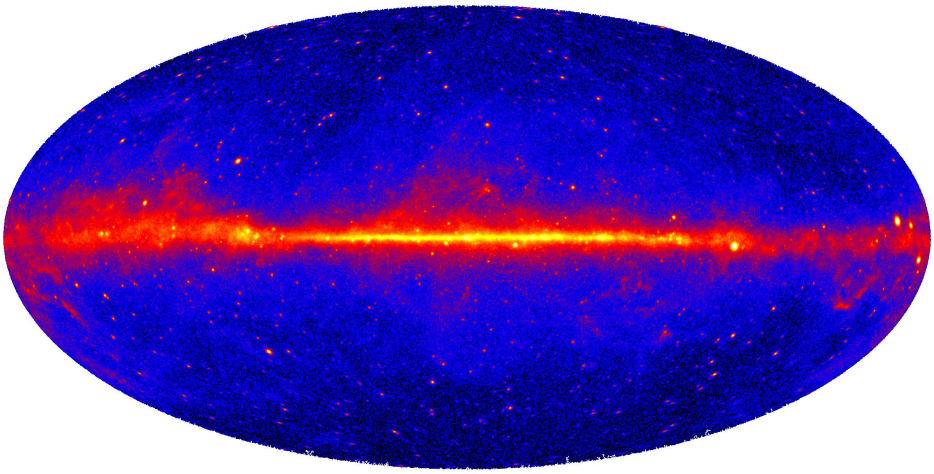

Figure 2.1: Gamma-ray emission ($E > 1\,\mathrm{GeV}$) background over the whole sky in galactic coordinates. The figure is based on five years of data from the Fermi Gamma-Ray Space Telescope. Brighter colours resemble higher gamma-ray flux. Adapted from [3].

2.1 Gamma-Ray Production Mechanism

By investigating gamma-ray spectra, the underlying CR interaction causing the gamma rays can be derived. A map of the gamma-ray emission is shown in Figure 2.1. CRs are produced in various galactic or extragalactic sources (e.g. stars, supernovae etc.) and can interact with gases (hadronic case) or electromagnetic

fields (leptonic case). Both cases create distinguishable observable gamma-ray spectra. In the next chapters, the hadronic and leptonic interactions are discussed in greater detail.

2.1.1 Hadronic Interaction

CRs interact with the atoms in gases and undergo proton-proton interactions. This interaction creates mostly pions (neutral π^0 or charged $\pi^{\pm}$). These pions have a short life span (mean lifetime $\tau \approx 2.2\,\mu s$ [4]) and decay. If the pion is neutral, it decays into photons (see Equation 2.1). If the pion is charged positively/negatively, it decays into an anti muon/muon and neutrino/anti neutrino. In addition, the decay may produce an additional photon, albeit with a very low probability ($6 \cdot 10^{-8}\,\%$ [4], see Equation 2.2 and Equation 2.3). This process is called radiative muon decay and results from the first order quantum electrodynamics correction, where an additional bremsstrahlung photon is emitted [5]. Due to this low probability, the gamma ray spectrum is dominated by the neutral pion decay. The schematic hadronic interaction is shown in the bottom left of Figure 2.2. The energy of the resulting photon, produced by the pions, can be approximated by $E_\gamma \sim 0.1 \cdot E_\pi$[6].

$$\pi^0 \rightarrow 2\gamma \tag{2.1}$$

$$\pi^+ \rightarrow \mu^+ + \nu_\mu \qquad \Rightarrow \qquad \mu^+ \rightarrow \mathrm{e}^+ + \nu_\mathrm{e} + \bar{\nu}_\mu (+\gamma\ (6 \cdot 10^{-8}\,\%)) \tag{2.2}$$

$$\pi^- \rightarrow \mu^- + \bar{\nu}_\mu \qquad \Rightarrow \qquad \mu^- \rightarrow \mathrm{e}^- + \bar{\nu}_\mathrm{e} + \nu_\mu (+\gamma\ (6 \cdot 10^{-8}\,\%)) \tag{2.3}$$

2.1.2 Leptonic Interaction

If CRs interact with an electromagnetic field, gamma rays can be created. The most dominant gamma-ray-producing interactions are Inverse Compton Scattering (ICS), bremsstrahlung and synchrotron radiation [7].

These interactions, the resulting gamma-ray spectra $\frac{\mathrm{d}N_\gamma}{\mathrm{d}E_\gamma}$ and the cooling time for electrons (τ_e) are discussed in greater detail in the following sections.

Inverse Compton Scattering

Electrons with energies in the ultra-relativistic regime can boost low-energy photons into the gamma-ray energy range. This process can be interpreted as an energy exchange, the electron loses energy which the photons gain. A schematic of the process is shown in Figure 2.2 top right corner. This process happens with photons from the cosmic microwave background (CMB). The resulting gamma-ray spectrum depends on the energy ratio of the incoming photon to the electron rest energy $m_e c^2 = 0.511\,\mathrm{MeV}$. The lower limit $E_\gamma \ll m_e c^2$ is referred to as Thomson limit, and the higher limit $E_\gamma \gg m_e c^2$ is called Klein-Nishina limit. In the Thomson limit the electron loses energy in big discreet portions and in Klein-Nishina limit the energy loss of the electron is much smaller for every scattering and therefore continuous. The resulting energy spectra are

$$\frac{\mathrm{d}N_\gamma}{\mathrm{d}E_\gamma} \propto \begin{cases} E_\gamma^{-(\alpha+1)/2} & \text{Thomson limit} \\ E_\gamma^{-(\alpha+1)} & \text{Klein-Nishina limit} \end{cases}, \tag{2.4}$$

where α represents the power of the underlying electron population. The resulting cooling times for the electrons are

$$\tau_e \propto \begin{cases} E_e^{-1} & \text{Thomson limit} \\ E_e & \text{Klein-Nishina limit} \end{cases} . \tag{2.5}$$

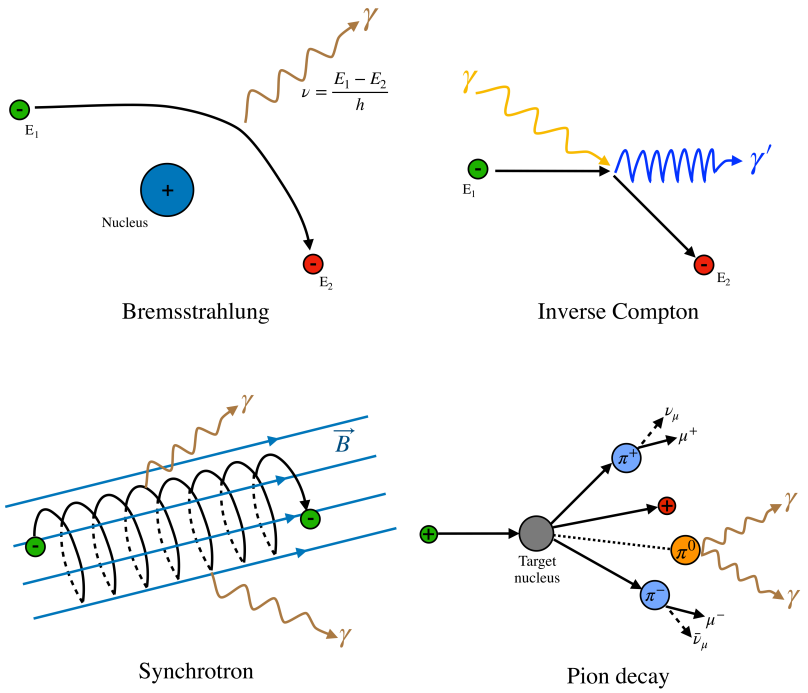

Figure 2.2: Schematic gamma-ray production mechanisms resulting from leptonic interactions (bremsstrahlung, inverse Compton and synchrotron radiation) and hadronic interaction (pion decay). Taken from [8].

Bremsstrahlung

Photons, which are emitted when an electron decelerates in a Coulomb field (atom nucleus), are called bremsstrahlung. A schematic interaction is shown in Figure 2.2 top left corner. For the SH considered in this work, the process is subdominant.

Synchrotron Radiation

Synchrotron radiation occurs when electrons are accelerated perpendicular to their current velocity by a magnetic field. The resulting photons possess energies in the keV energy range, but they may gain additional energy through ICS. This process is then referred to as synchrotron self-Compton scattering. In Figure 2.2 bottom left corner, a schematic synchrotron radiation process is shown. For the halo considered in this work, the process is not dominant (weak magnetic fields outside the galaxy [6]).

2.2 Detection

Two approaches are available to detect these cosmic gamma-rays: space-based telescopes and ground-based telescopes.

The atmosphere is opaque to gamma-rays, and thus, they cannot be observed directly by ground based experiments. Due to this fact, space-based detectors have been proposed. An example is the Fermi gamma-ray space telescope (see Figure 2.4), which will be explained in greater detail in subsection 2.2.1. Due to the power-law spectral energy distribution of CR, the rate of gamma-rays decreases with increasing energy. To maintain acceptable detection rates, larger detection areas are required. This, however, becomes increasingly unfeasible for satellites. Thus, one needs to rely on ground-based telescopes to detect higher energy gamma rays.

Even though the atmosphere is not transparent to gamma rays, one can detect gamma rays indirectly. The indirect detection method exploits the Cherenkov light of particle showers that result from interaction of gamma rays with the atmosphere. One example of such a telescope is the future Cherenkov Telescope Array (CTA) (see Figure 2.8), which will be discussed in greater detail in subsection 2.2.2.

2.2.1 Space-Based: Fermi-LAT

The Fermi Gamma Ray Space Telescope (formerly known as Gamma-ray Large Area Space Telescope) was launched on 11 June 2008 and started its mission one month later. The satellite orbits the earth at an altitude of $\approx$ 565 km with an orbital inclination of 25.6°. The Fermi gamma-ray space telescope is equipped with two different instruments, the Gamma-ray Burst Monitor (GBM) and the Large Area Telescope (LAT).

The first instrument is used to detect gamma-ray bursts. The second is detecting gamma-rays in an energy range of 20 MeV to 300 GeV. With a more sufficient analysis approach, gamma rays up to the 1 TeV range can be investigated (e.g. [9]).

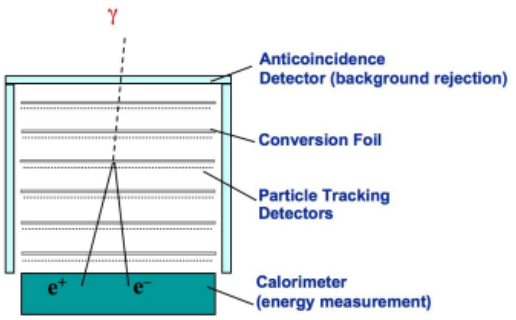

Figure 2.3: Schematic structure of the LAT [10].

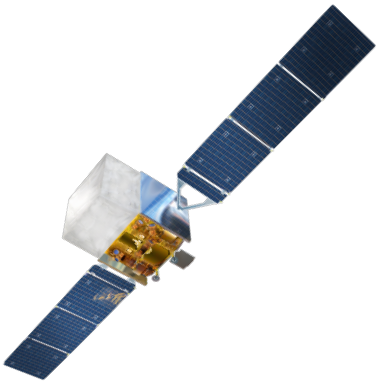

Figure 2.4: Artistic representation of the Fermi gamma-ray space telescope spacecraft [11].

Functionality

The general idea of the LAT is to detect particle tracks created by gamma rays. A schematic structure is shown in Figure 2.3. The four main parts are discussed in more detail.

Anticoincidence Detector Gamma rays are rare compared to CRs, which appear in the order of 10^2 to 10^5 times more often, depending on the energy range. Therefore, a good rejection is needed. The anticoincidence detector creates a light flash if it is hit by a CR. In comparison, the gamma rays can pass freely without any interaction.

Conversion Foil In the next step, the gamma rays interact with the conversion foil. The conversion foil is made out of tungsten (Z=74), because its high atomic number favours pair production ($\propto Z^2$). Thus, an electron-positron pair is created and travels further through the detector, creating ions.

Silicon Strip Detectors The silicon strip detectors (depicted as "Particle Tracking Detectors" in Figure 2.3) track the path of the ions. The detector alternates in the X and Y directions for better path reconstruction.

Calorimeter At last, the particles hit the caesium iodide calorimeter, which measures the total deposited energy. The caesium iodide produces a light flash when hit by particles. The intensity of the light flashes are proportional to the incoming particles' energy. By measuring the intensity of the light flashes, the deposed energy can be derived.

Instrument Response Functions

Before analysing the raw data of a telescope, one has to take into account, that no instrument detects events perfectly. Another problem is that, the instrument response function can not be modelled perfectly. These troubles lead to systematic errors, which are described by the individual instrumental response functions (IRF). In the following sections, the IRFs for the Fermi-LAT and CTA are discussed, whereas in the former case also the basic concept of the specific IRF is explained.

Sensitivity Curve The sensitivity curve of a telescope shows the minimal flux the telescope can detect. There are several reasons that limit the sensitivity of a telescope. One example are background events. For this case, a flux below the sensitivity curve means it can't be distinguished from the background events. There are other limiting factors, which are discussed for the individual telescopes

The sensitivity curve for Fermi-LAT can be found in [12]. In Figure 2.5a, the sensitivity curves for four different positions are shown. The difference stems from the emissions from our own Galaxy, the further away one looks from the galactic plane, the lower the sensitivity curve (less background events). For the future analysis of the Andromeda Galaxy, the north Celestial pole sensitivity curve is chosen (black line in Figure 2.5a) because it is the closest to the Andromeda Galaxy if one assumes mirror symmetry around the galactic plane (see Figure 2.6).

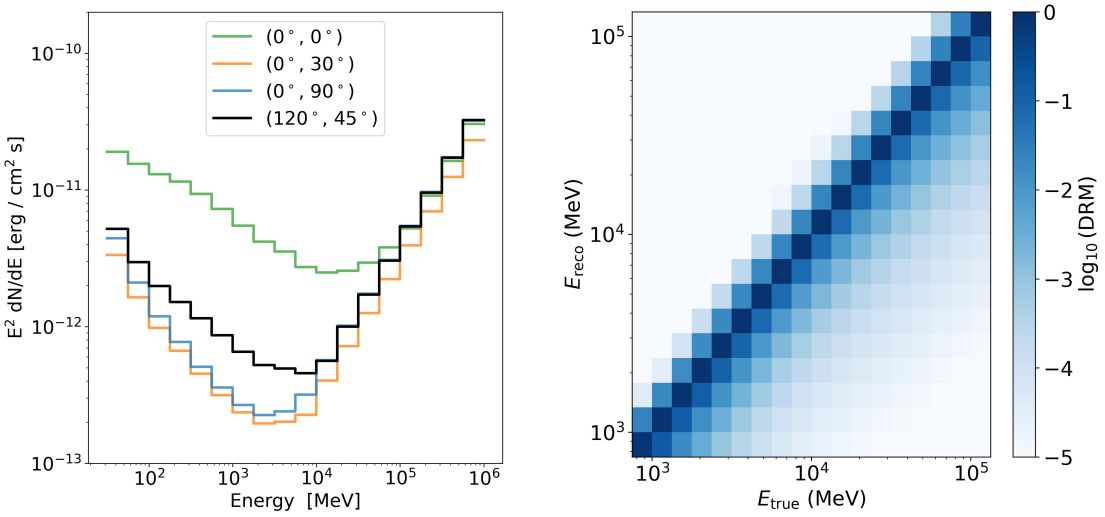

(a) Fermi-LAT PSF. **(b)** CTA PSF.

Figure 2.5: **(a)**: Sensitivity for Fermi-LAT for the galactic centre $(0°, 0°)$, intermediate latitudes $(0°, 30°)$, north Galactic pole $(0°, 90°)$ and north Celestial pole $(120°, 45°)$. The coordinates are given in galactic coordinates. **(b)**: Energy dispersion for Fermi-LAT in arbitrary scaling. The reconstructed energy follows a probability distribution, therefore the addition of a row results in 1.

Point Spread Function In gamma-ray astronomy, most sources are theoretically described as point sources. In a real measurement, the point sources get spread over an area, because of several physical processes, e.g. imaging errors. This broadening is described by the point spread function (PSF). The PSF depends on different parameters, e.g. the energy of the detected particle.

In Figure 2.7a the point spread function for Fermi-LAT is shown. For lower energies ($< 10\,\mathrm{GeV}$) the PSF increases strongly. This is a result of the secondary particle's multiple scattering [13]. Therefore, the track reconstruction is less accurate.

Energy Dispersion The energy of a particle has to be reconstructed. This process is error-prone and is described by a distribution of the reconstructed energy. This is represented as a matrix, the so-called energy dispersion matrix.

In Figure 2.5b is the energy dispersion matrix shown for Fermi-LAT. A bias to lower energy can be seen, this means the reconstructed energy underestimates the true energy.

2.2.2 Ground-Based detection methods: CTA

The Cherenkov Telescope Array is a stereoscopic Imaging Atmospheric Cherenkov Technique (IACT) telescope array planned to start operation in late 2020s [14]. CTA is planned to consist of more than 60 telescopes placed on the Northern and Southern Hemisphere. CTA detects gamma rays in an energy range of 20 GeV to 300 TeV. The telescopes are built in three different sizes, adapted to different energy ranges. An artistic representation of the southern station is shown in Figure 2.8. In the following chapters, the general functionality of CTA and afterwards the most important IRFs for CTA are discussed.

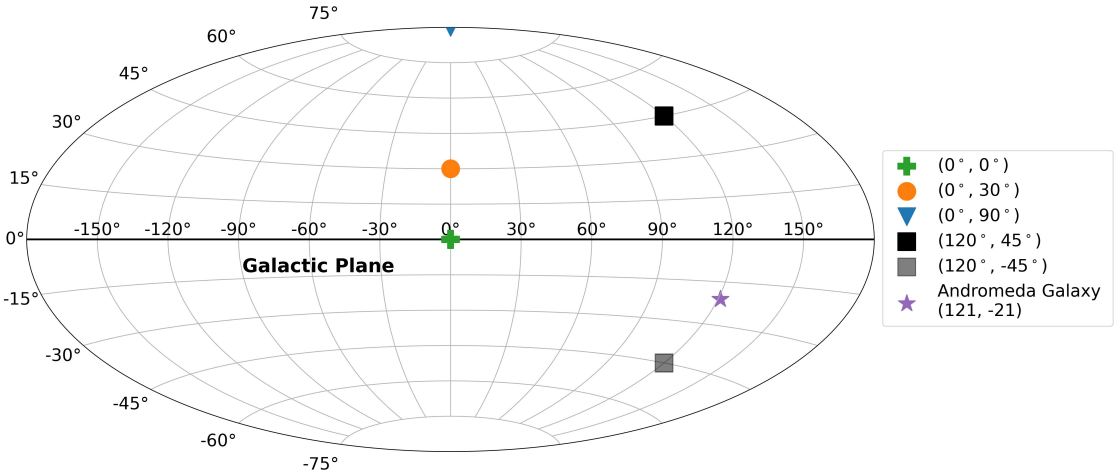

Figure 2.6: Position of the Fermi-LAT's sensitivity curves shown in Figure 2.5a on the sky in galactic coordinates. Also shown is the mirrored north Celestial pole $(120°, -45°)$, which is the closest to the Andromeda Galaxy $(121°, -21°)$.

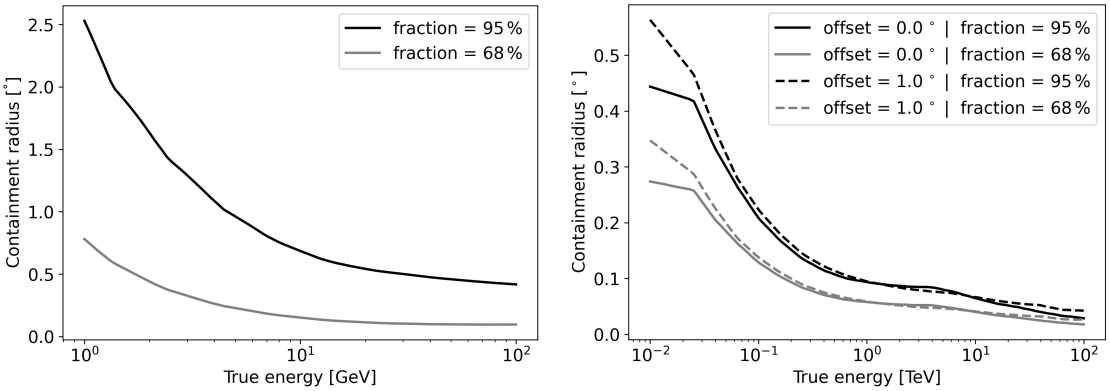

(a) Fermi-LAT PSF. **(b)** CTA PSF.

Figure 2.7: Point spread function for Fermi-LAT **(a)** and CTA **(b)**. In both figures are two containment radii 68 % and 95 % shown. In the case of CTA, the PSF also depends on the distance from the camera centre. The case for no offset and 1° are shown.

Imaging Atmospheric Cherenkov Technique

Imaging Atmospheric Cherenkov Technique (IACT) is used to detect gamma rays in the atmosphere. It is based on detecting air showers created by CRs or gamma rays.

Air Showers The Earth's atmosphere gets constantly bombarded by CRs and photons. If the CRs or photons' energy is high enough, they can produce an air shower. Both cases will be discussed briefly in the following section.

In the first case, a gamma ray can create an electron-positron pair in the vicinity of a nucleus of the atmosphere (pair production). The particles in turn emit bremsstrahlung as they travel through the coulomb fields of other nuclei in the atmosphere. The emitted photon can then again create an electron-positron pair, and the whole process repeats. After every cycle, the particles lose energy and at a certain energy (≈ 86 MeV) the pair production is not feasible any more and the cas-

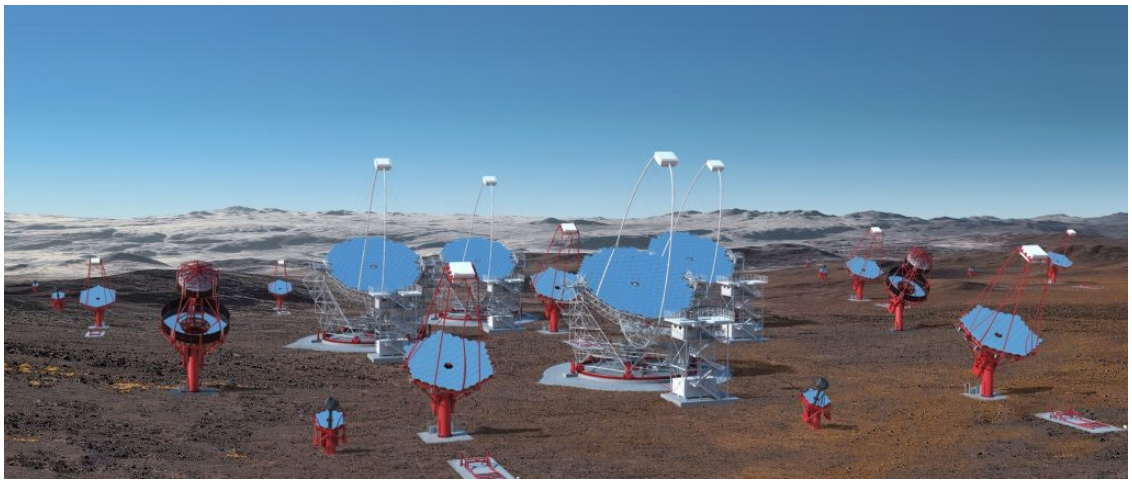

Figure 2.8: Artistic representation of CTA's Southern Station (located in the Southern Hemisphere) [15]. In the picture, the three different telescopes, medium-sized telescope (MST), small-sized telescope (SST) and large-sized telescope (LST), are shown (with preliminary positions). The Southern Station is located in the Atacama Desert in Chile.

cade stops. This process is referred to as electromagnetic air shower. A schematic representation for the gamma-ray induced air shower is shown on the left side of Figure 2.9.

In the second case, a CR hits the atmosphere and interacts with atoms, resulting in the creation of hadrons. The hadrons mostly consist of pions. These pions can interact in different ways or decay. The hadronic air showers can create electromagnetic sub-showers. The electromagnetic sub-showers from CRs can lead to wrongly labelled events. A schematic representation for the CR induced air shower is shown on the right side of Figure 2.9.

Cherenkov Radiation Particles travelling faster than the speed of light in a medium with the refractive index n ($v > c/n$) causes the medium to emit Cherenkov radiation. This is because, the particles polarize the medium and local dipole radiators are created. These dipole radiators create a light cone with expansion angle $\cos(\theta) = c_0/(nv)$, where c_0 is the speed of light in the vacuum.

The IACT is used to detect the faint Cherenkov light flashes resulting from air shower. Stereoscopic systems are used to reconstruct the direction of the event. Currently, there are two major IACT telescope MAGIC and H.E.S.S. For the future, the Cherenkov Telescope Array is planned, which will be used in this work and briefly discussed.

Sensitivity Curve The sensitivity of CTA is limited by three different factors

- background events
- low significance
- low statistic.

In the lower energy range, the background events are the limiting factor for CTA. The background consists mainly of the night sky background or events induced by

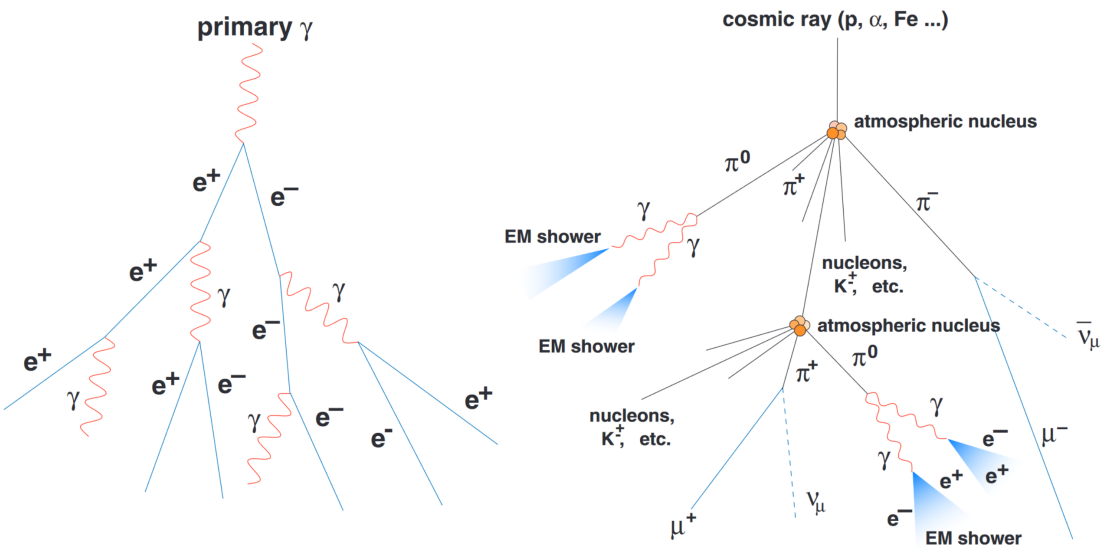

Figure 2.9: Schematic representation of a particle shower induced by a gamma ray (left side) or cosmic ray (right side). Taken from [16].

protons. If a source is below the sensitivity, it can not be distinguished from the background flux. The next limiting factor is low statistics. The source can be distinguished from the background, but the flux gets less significant (below 5σ). In the high energy limit, the events are getting sparse and fluxes with less than 5 counts are rejected. A schematic sensitivity curve is shown in Figure 2.10 with the three different criteria.

In the simulation of the sensitivity curve, four parameters need to be defined

- observation time
- background systematic fraction
- minimal sigma
- minimal gamma-ray count.

These parameters influence the sensitivity in different ways.

In the first case, a higher observation time increases the sensitivity of CTA by increasing the statistic and the gamma-ray count for higher energy bins. In Figure 2.11a one can see a lowering of the sensitivity curve for an increase in observation time. For the second situation, an increase in the background fraction decreases the sensitivity, because more events get rejected. This is shown in Figure 2.11b. The third case revolves around varying the significance level. The lower the significance, the better the sensitivity. In Figure 2.11c the sensitivity curves are shown. Lastly, the minimal gamma ray count is changed. The higher the limit, the worse the sensitivity gets for higher energies. In Figure 2.11d the increase can be seen.

The parameters used for the CTA's sensitivity used for further analysis are shown in Table 2.1.

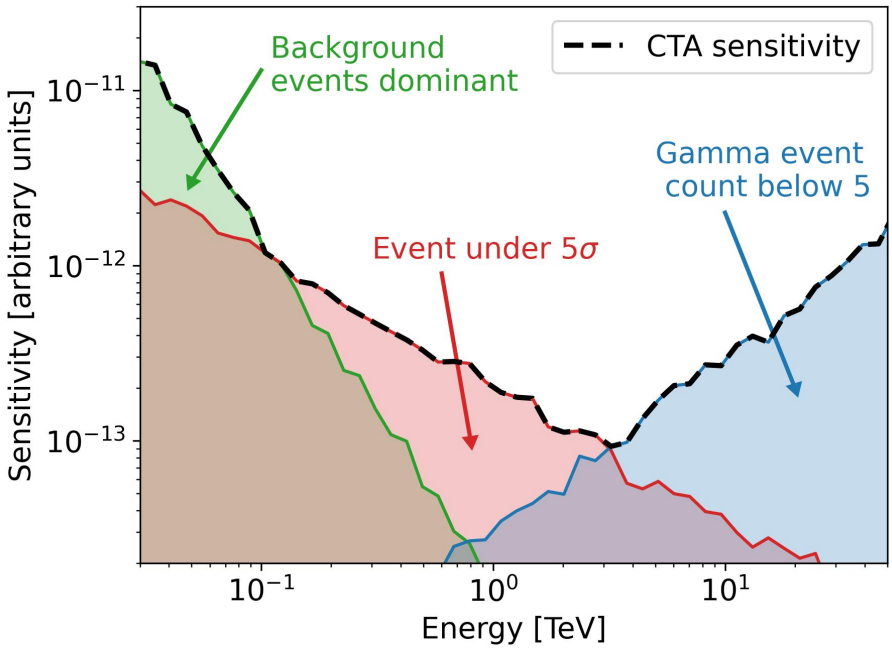

Figure 2.10: Schematic sensitivity curve for CTA in the TeV energy range for arbitrary sensitivity flux units. The three limiting factors for the sensitivity of CTA are shown. Firstly, in green is the sensitivity curve for the background rejection shown, Secondly, the rejection for flux with significance below 5σ and lastly the rejection for the case of low statistics (less than 5 gamma-ray counts). The resulting CTA significance is shown as a dotted, black line, which follows the highest sensitivity of the three different criteria for every energy bin.

Point Spread Function The PSF for CTA depends not only on the energy but also on the distance from the centre of the image. The further away a point source is or the lower the energy is, the higher the point spread function gets. In Figure 2.7b, the PSF for either a containment fraction of 68 % or 95 % and no offset or 1° offset are shown.

Parameters	**Values**
Observation time	100 h
Background systematic fraction	0.05
Minimal sigma	5
Minimal gamma-ray count	10

Table 2.1: Parameters used for simulation of CTA's sensitivity used for further analysis. For the time an optimistic value was chosen and for the remaining parameters the default values for CTA analysis were chosen (see [17]).

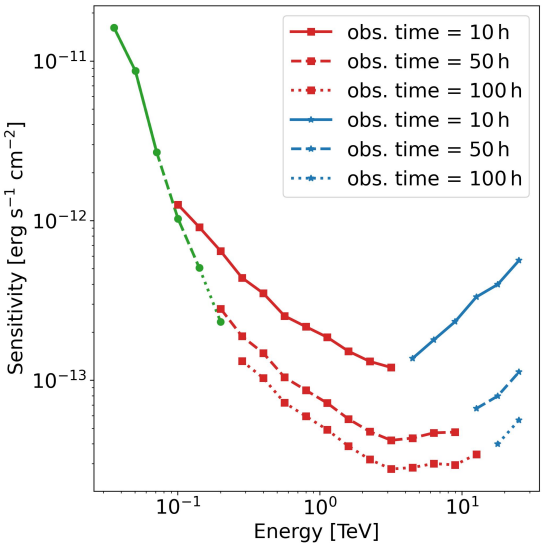

(a) Observation time dependency.

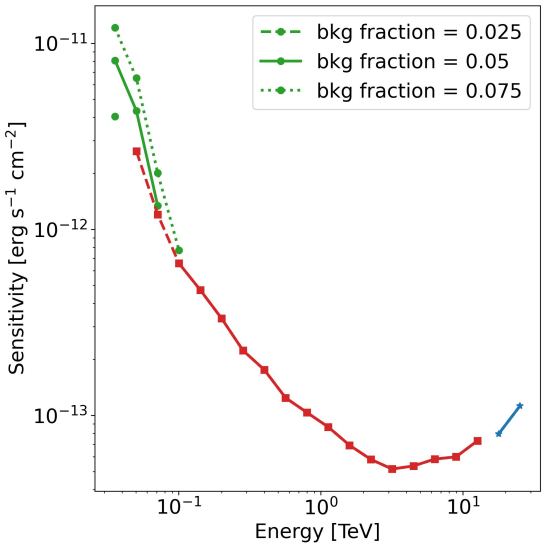

(b) Background fraction dependency.

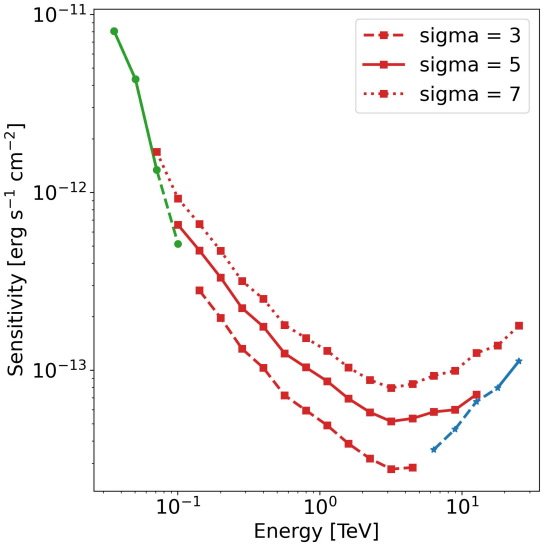

(c) Significance dependency.

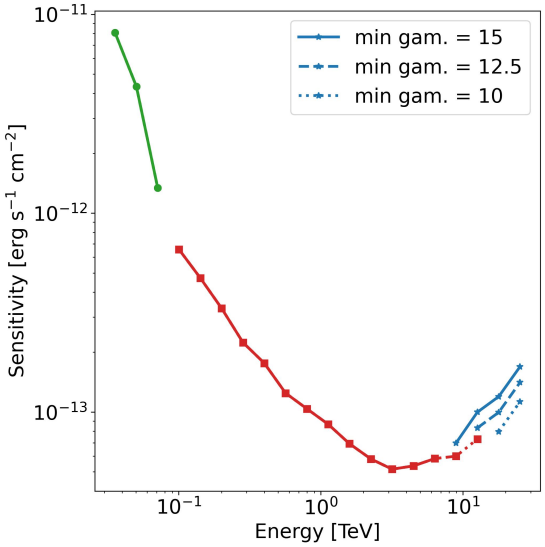

(d) Minimal gamma ray count dependency.

Figure 2.11: CTA's significance dependency on the different parameters: observation time **(a)**, background fraction **(b)**, significance **(c)** and minimal gamma ray count **(d)**. The remaining parameters are set to their default value for each case (sigma = 5, background fraction = 0.05, minimal gamma ray count = 5 and assumed observation time of 100 h).

Chapter 3

Galaxies and Halo Models

This chapter presents the potential galaxy candidates and the origin of the gamma rays caused by CRs.

3.1 Hubble Sequence

A way to categorise galaxies is by using the Hubble Sequence. It was first proposed by Edwin Hubble in 1926. Every galaxy can be put into one of the four categories

- Elliptical Galaxy (EG)
- Lenticular Galaxy (LG)
- Spiral Galaxy (SG)
- Irregular Galaxy (IG).

Galaxies classified as EG are typically observed as elliptical shapes, lacking any discernible disk and bulge structure. These EGs are denoted as E followed by a numeric value n, where the number n signifies the level of ellipticity, ranging from 0 (resembling a circle) to 7 (elongated). In Figure 3.1, a diagram depicting various galaxy forms, along with illustrative examples, is presented on the left side.

Likewise, LGs share a visual resemblance to EL galaxies, with the key distinction being the presence of both a bulge and a disk. However, the disk lacks any internal structure. LGs are designated as S0 in Figure 3.1.

Within the category of SGs, further subdivision is possible, separating them into two subcategories: regular spiral galaxies (seen Figure 3.1 upper fork) and barred spiral galaxies (see Figure 3.1 lower fork). Both types feature a bulge, disk, and spiral arms, but barred spiral galaxies exhibit a distinctive bar-like structure. Notable examples include the Andromeda Galaxy for regular SGs and the Milky Way for bar SGs.

Finally, the last category is known as IG, encompassing any galaxies that do not fit into the aforementioned categories.

The Hubble Sequence doesn't represent the evolution of galaxies. Nevertheless, In the early universe more SGs are observed and late universe more IGs. IGs are currently believed to be created in a collision of two SGs, which would explain the observations [18].

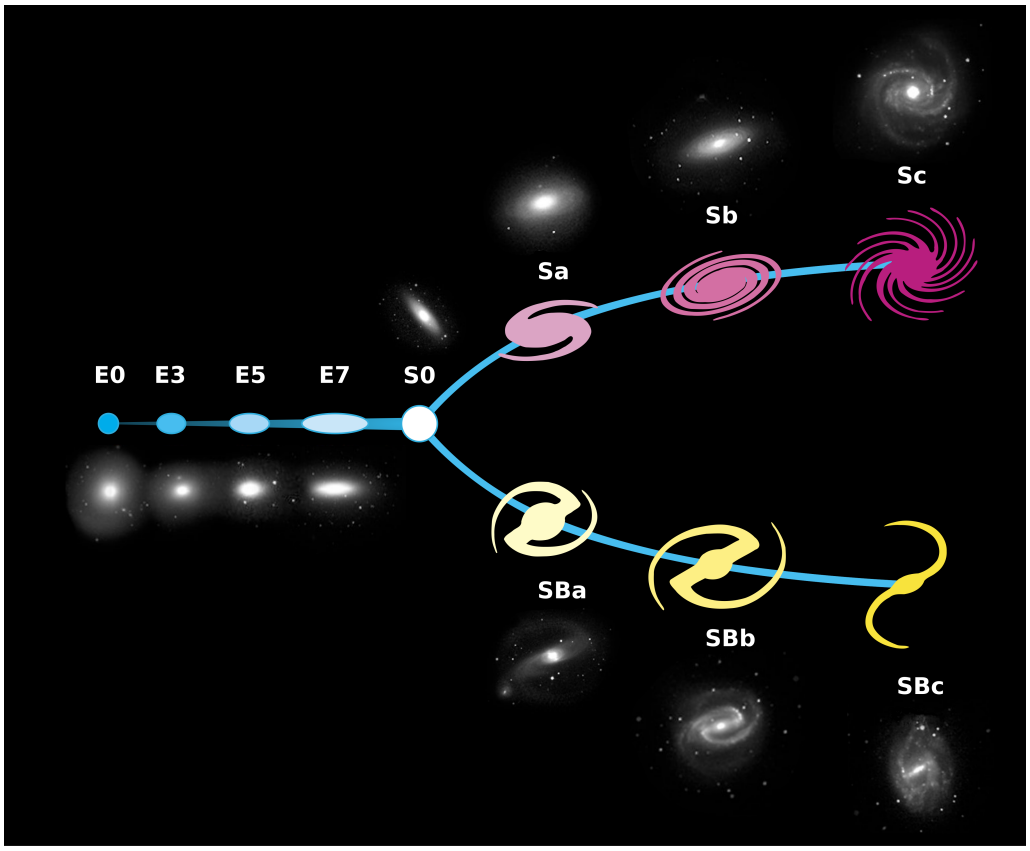

Figure 3.1: Schematic sketch of the Hubble Sequence with example galaxies [19].

3.2 Nearby Spiral Galaxies

Galaxies in the neighbourhood are listed in the Updated Nearby Galaxy Catalog (NEARGALCAT)[20]. It consists of galaxies with a maximum distance of 11 Mpc with a total count of 869. The catalogue includes different observable galaxy characteristics. For the thesis of most interest are:

- Position of the galaxy:
  The longitude and latitude (galactic frame) are given.

- Absolute magnitude:
  The absolute magnitude in the B-band (blue light 430 nm to 490 nm) is given. The absolute magnitude is defined as the magnitude one would measure in a 10 pc distance of the object.

- Linear diameter:
  The diameter at the Holmberg isophote is given in kpc. The Holmberg isophote is defined as an isophote with the surface brightness of $\mu_{\text{Holmberg}} = 26.5\,\text{mag}\,\text{arcsec}^{-2}$ in the B-Band [21]. The galactic extinction and inclination are taken into account.

- Galaxy mass:
  The mass of the galaxy is given as a power of ten of the mass of the sun ($M_\odot \approx 2 \cdot 10^{30}\,\text{kg}$).

- Distance:
  The distance to the galaxy is given in Mpc. The maximum distance in the NEARGALCAT is 11 Mpc.

This catalogue includes galaxies of all kinds, for this project only the SGs are of interest. By only selecting the SGs, the total number drops from 869 to 305. This number can be reduced further by excluding dwarf SGs, resulting in 200 galaxies left. For the project, only SG which are similar to the Andromeda Galaxy are required. Therefore, three cuts on the linear diameter, absolute magnitude and galaxy mass are performed. The specific cut criteria with the parameters of M31 are given in Table 3.1. By comparing the distribution of the parameter values of the SGs with dwarf SGs, the criteria were chosen to cut out almost all dwarf SGs (see Appendix A for more details).

Parameters	**Andromeda Galaxy**	**Cut criteria**
Linear diameter [kpc]	43.45	> 10
Absolute magnitude [mag]	-21.4	< -17
Mass [$M_\odot$]	$10^{11.5}$	$> 10^{9.5}$

Table 3.1: Values of the linear diameter, absolute magnitude and mass of the Andromeda Galaxy with their associated cutting criteria are shown.

These selection cuts reduce the total amount of galaxies to 97. The galaxies affected by the cuts are likely dwarf galaxies, which aren't labelled in the NEARGALCAT. The distribution of galaxies in the NEARGALCAT and the remainder galaxies on the sky are shown in Figure 3.2. In Figure 3.3 on the left side the diameter-mass relation of the remaining galaxies are shown. A linear trend in double logarithmic scaling can be seen. Additionally, one can see that the Andromeda Galaxy is an outlier for nearby SGs. It is one of the biggest and most massive galaxy. This is supported by Figure 3.3 where the difference between catalogue mass and the expected mass from the linear fit is shown.

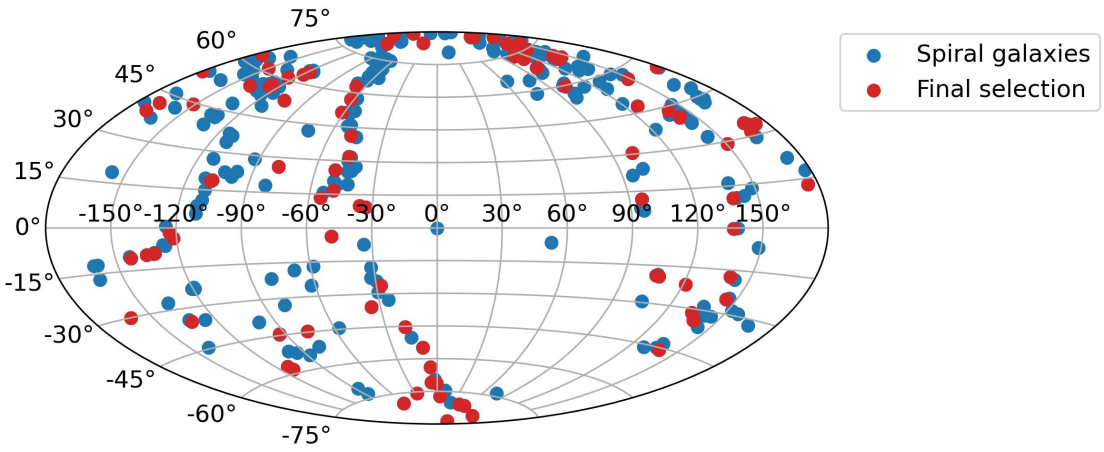

Figure 3.2: Distribution of galaxies in galactic coordinates from the updated nearby galaxy catalogue (blue dots) and the remainder spiral galaxies (red dots) after several selection cuts.

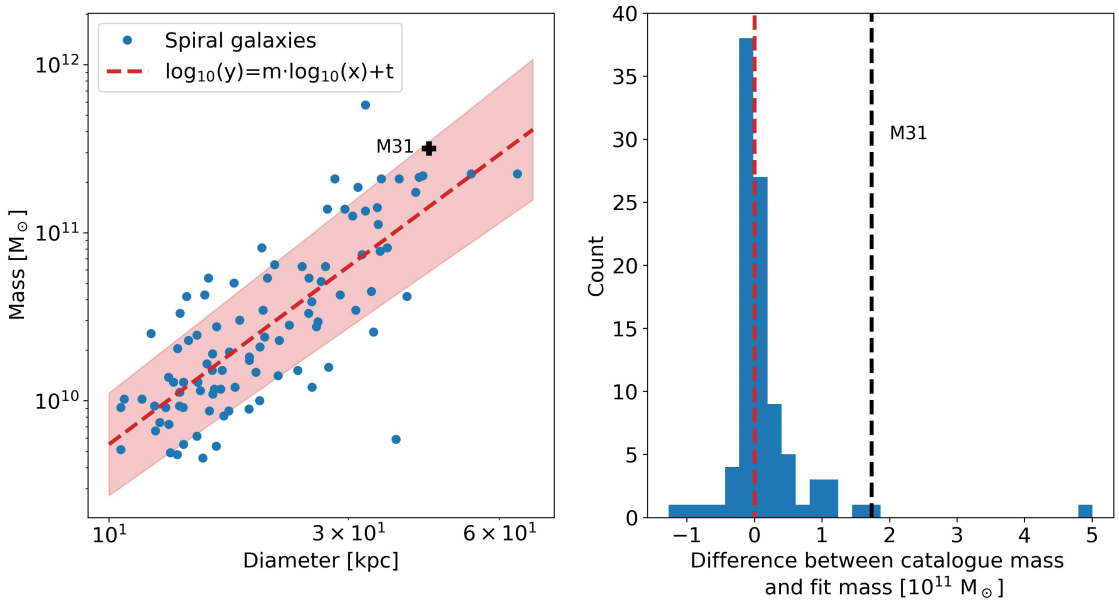

Figure 3.3: Left side: Linear fit to the diameter-mass relation in double logarithmic scale of the final spiral galaxies. Right side: Distribution of the difference of the fitted mass to the actual mass.

3.3 Cosmic Ray Halos

A way to explain the gamma-ray emission from the SH region, is by assuming a cosmic ray halo. The ability of cosmic rays to escape their originating galaxy can be inferred from the detection of extragalactic cosmic rays. In the following section, a simple CR Halo is introduced which is based on a transport equation. Two different scenarios are investigated, either with a leptonic or hadronic origin.

3.3.1 Transport Equation

The transport equation describes the time evolution of the total resulting particle spectrum $N(E,t)$ [22]

$$\frac{\partial N}{\partial t} = Q(E,t) - \frac{\partial(b(E,t)N(E,t))}{\partial E} - \frac{N(E,t)}{t_{\text{escape}}}, \tag{3.1}$$

where $Q(E,t)$ is the source spectrum, $b(E,t)$ is the energy loss rate of the particles and t_{escape} the escape time of the particles. For the simulation, only the source spectrum is needed.

To find the optimal source spectrum parameters, one can use a minimizer to minimize the χ^2 function. In the thesis, the spectrum is fitted to data with upper limits. To take this upper limits into account, an adjusted χ^2 function [23] is used:

$$\chi^2 = \sum_{\text{i}}^{\text{n}} \left(\frac{x_{\text{i}} - \hat{x}_{\text{i}}(\theta)}{\sigma_{\text{i}}} \right)^2 + \sum_{\text{j}}^{\text{m}} 2 \ln \left(\frac{1 + \text{erf}\left(\frac{x_{\text{j}} - \hat{x}_{\text{j}}(\theta)}{\sigma_{\text{j}}} / \sqrt{2} \right)}{2} \right), \tag{3.2}$$

where x_{i} represents data with an error σ_{i}, which appears n-times, where x_{j} represents upper limits with an error $\sigma_{\text{j}} = {}^{x_{\text{j}}}/_{2}$, where 2 comes from the 2nd confidence level,

which appears m-times, $\hat{x}_{\mathrm{i/j}}(\theta)$ represents the resulting values from the model with the parameters θ and the error function

$$\mathrm{erf}(x) = \frac{2}{\sqrt{\pi}} \int_0^x e^{-t} \mathrm{d}t. \tag{3.3}$$

For easier computation, the error function gets approximated for $x < 7.5$ as

$$f(x) = 15 \cdot x + 50. \tag{3.4}$$

The simulations are done with `GAMERA` [24], which is a package design to solve such transport equation for astrophysical sources. In the following sections, the two different cases are discussed.

3.3.2 Leptonic Case

In the first case, a leptonic source is considered. For that reason the source spectrum from [6] is adapted, with the following time independent proportionality

$$Q(E) \propto \left(\frac{E}{1\,\mathrm{GeV}}\right)^{-2} e^{-E/500\,\mathrm{GeV}}. \tag{3.5}$$

By using the luminosity of electrons L_e and average lifetime τ_e of electrons, the source spectrum can be defined as

$$Q(E) = \underbrace{\frac{L_e \tau_e}{\int E \cdot \left(\frac{E}{1\,\mathrm{GeV}}\right)^{-p} e^{-E/o} \mathrm{d}E}}_{\text{scale}} \cdot \left(\frac{E}{1\,\mathrm{GeV}}\right)^{-p} e^{-E/o}, \tag{3.6}$$

where p is called the power and o the energy cutoff. τ_e is defined as

$$\tau_e(E) \approx 1.3 \times 10^6 \cdot \left(\frac{E}{1\,\mathrm{TeV}}\right)^{-1} \mathrm{yr}. \tag{3.7}$$

The expected electron luminosity equals the observed gamma-ray luminosity $L_\gamma = 1.7 \times 10^{39}\,\mathrm{erg\,s^{-1}}$[6]. For the expected energy range of $(0.6 - 6)\,\mathrm{TeV}$ the scale results in

$$\mathrm{scale} \approx 1.4 \times 10^{58}\,\mathrm{erg}^{-1}. \tag{3.8}$$

For further analysis, Equation 3.6 is simplified to

$$Q(E|p, o, c) = c \cdot 1.4 \times 10^{58}\,\mathrm{erg}^{-1} \cdot \left(\frac{E}{1\,\mathrm{GeV}}\right)^{-p} e^{-E/o} \tag{3.9}$$

where c represents an additional scaling factor.

Additional parameters needed for the simulation, e.g. the magnetic field, are shown in Table 3.2.

Firstly, the spectrum from Karwin et al. 2019 is recreated with the initial parameters given in Recchia et al. 2021(see Table 3.3). The result is shown in Figure 3.4a. In the case of leptonic source spectrum for the SH, the resulting spectrum is only dominated by ICS (see Appendix B for more information).

Simulation parameter	Value
Ambient density [cm^{-3}]	0.5×10^{-3}
Magnetic field [G]	1×10^{-10}
Temperature [K]	2.7
Energy density [$\mathrm{erg\,cm}^{-3}$]	$0.25 \cdot 1.602\,18 \times 10^{-12}$
Distance [pc]	765×10^{3}

Table 3.2: Simulation parameters needed for `GAMERA` describing the surrounding area.

Secondly, the parameters are fitted to the spectrum from Karwin et al. 2019. For the fitting, the package `iminuit` [25] is used. The error bands are approximated by `iminuit`, which uses the following equation

$$\sigma_f = \left(\frac{\partial f}{\partial \vec{q}}\right)^{\mathrm{T}} \cdot \mathrm{cov}_{\vec{q}} \cdot \frac{\partial f}{\partial \vec{q}}, \tag{3.10}$$

where $\vec{q}$ represent the different simulation parameter p, o and c, $\mathrm{cov}_{\vec{q}}$ the covariance matrix resulting from the optimization and f the function for which the error bands are calculated. The resulting best-fit spectrum is shown in Figure 3.4b and the best-fit parameters are shown in Table 3.3. The best-fit parameters differ from the initial parameters.

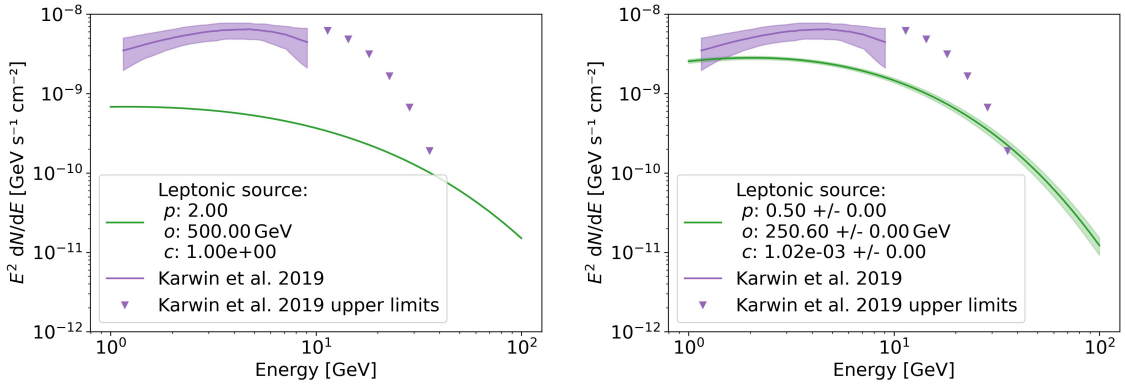

(a) Initial parameters from Recchia et al. 2021. **(b)** Best-fit parameters.

Figure 3.4: Best-fit spectral model for the SH from Karwin et al. 2019. The shaded region show the 1σ error band and downward pointing triangles give upper limits. The spectrum is compared to **a**: Resulting gamma-ray spectrum from a leptonic source spectrum simulated with the initial parameters given in Recchia et al. 2021. **b**: Resulting gamma-ray spectrum from a leptonic source spectrum simulated with the best-fit parameters resulting from a fit to Karwin et al. 2019.

Fit parameter	Initial values	Fit results
p	2	0.50 ± 0.06
o [GeV]	500	250 ± 11
c	1	$(1.0 \pm 0.3) \times 10^{-3}$

Table 3.3: Parameter values for the leptonic source spectrum before (initial values) and after the fit to the spectrum from Karwin et al. 2019 are shown.

3.3.3 Hadronic Case

For the hadronic case, the same assumption for its source spectrum is made, just with different values:

$$Q \propto \left(\frac{E}{1\,\mathrm{GeV}}\right)^{-2} e^{-E/110\,\mathrm{GeV}}. \tag{3.11}$$

For an expected luminosity of $L_p = 1.8 \times 10^{41}\,\mathrm{erg\,s^{-1}}$, an expected lifetime of $\tau_p = 2 \times 10^9\mathrm{yr}$ scale can be calculated for an expected energy range of $(10 - 1000)\,\mathrm{GeV}$

$$\mathrm{scale} \approx 2.3 \times 10^{63}\,\mathrm{erg}^{-1}. \tag{3.12}$$

The resulting hadronic source spectrum is

$$Q(E|p,o,c) = c \cdot 2.3 \times 10^{63}\,\mathrm{erg}^{-1} \cdot \left(\frac{E}{1\,\mathrm{GeV}}\right)^{-p} e^{-E/o}. \tag{3.13}$$

The same simulation parameters are used as in the leptonic case (see Table 3.2).

Again, the spectrum from Karwin et al. 2019 is reproduced with the initial parameters given in Recchia et al. 2021. The spectra are shown in Figure 3.5a with the corresponding parameters listed in Table 3.4. The spectrum can not be reproduced for unknown reasons.

Next, source spectrum is fitted to the data from Karwin et al. 2019. The resulting spectra are shown in Figure 3.5b with the best-fit parameters shown in Table 3.4.

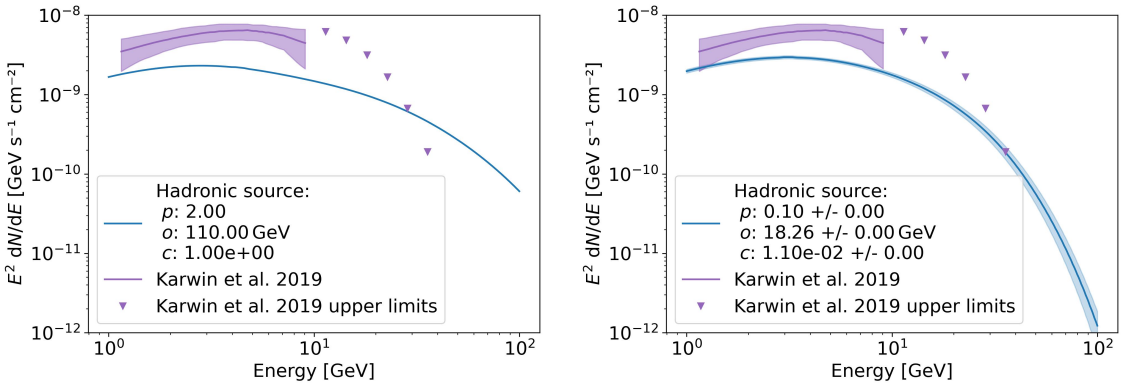

(a) Initial parameters from Recchia et al. 2021.

(b) Best-fit parameters.

Figure 3.5: Best-fit spectral model for the SH from Karwin et al. 2019. The shaded region show the 1σ error band and downward pointing triangles give upper limits. The spectrum is compared to **a**: Resulting gamma-ray spectrum from a hadronic source spectrum simulated with the initial parameters given in Recchia et al. 2021. **b**: Resulting gamma-ray spectrum from a hadronic source spectrum simulated with the best-fit parameters resulting from a fit to Karwin et al. 2019.

Lastly, the best-fit source spectra are compared with their initial spectra. In spectra are shown in Figure 3.6a for the leptonic case and in Figure 3.6b the hadronic case. The leptonic source spectrum has a higher flux at lower energies but stronger drop at higher (inflection point $\sim 3\,\mathrm{erg} = 1.8\,\mathrm{TeV}$). The hadronic source spectrum expects an earlier cutoff and higher drop in flux ($\sim 10^{20}$).

Fit parameter	Initial values	Fit results
p	2	0.10 ± 0.17
o [GeV]	110	18.3 ± 1.8
c	1	$(1.1 \pm 0.5) \times 10^{-2}$

Table 3.4: Parameter values for the hadronic source spectrum before (initial values) and after the fit to the spectrum from Karwin et al. 2019 are shown.

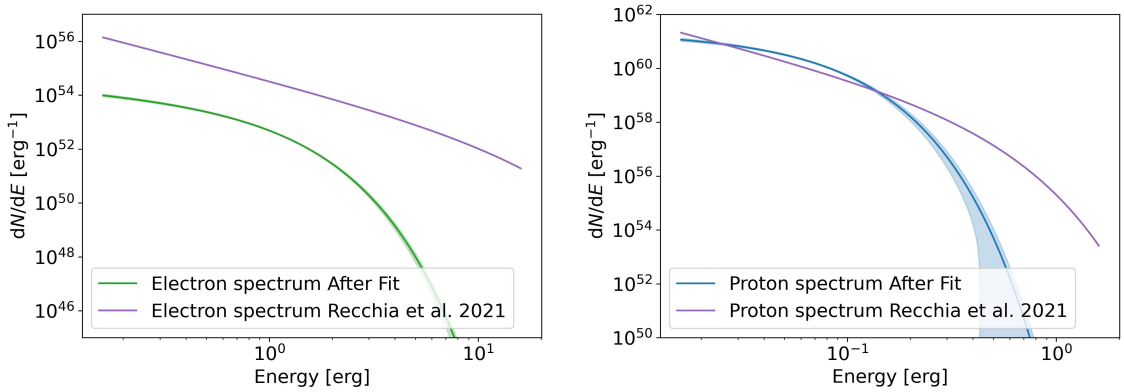

(a) Leptonic source spectrum.

(b) Hadronic source spectrum.

Figure 3.6: Source spectra for the parameters from Recchia et al. 2021 and the best-fit source spectrum resulting from fitting it to the spectra from Karwin et al. 2019 in the case of either leptonic **(a)** or hadronic **(b)** source spectrum.

Chapter 4

Dark Matter

One of the biggest mysteries of the universe is Dark Matter (DM). Many of the observation hint towards "invisible" matter in our universe. Currently, Numerous theories are developed to explain the DM. By investigating gamma rays, the number of potential DM theories can be narrowed down.

In this chapter, I will start with a brief section about the evidence for DM, then potential DM candidates are shown, especially weakly interactive massive particles (WIMPs). Lastly, I will show the current status of DM theories, how DM can be observed and afterwards how DM can be detected. The chapter is based on [26] and [27].

4.1 Evidence for Dark Matter

There is still no conclusive evidence for DM. Nevertheless, there are a lot of different phenomena in astronomy, which could be explained by DM.

4.1.1 Rotation Curves of Galaxies

In 1983, a study was carried out on the rotation curves of 60 different galaxies [28]. The result showed a flattening of the rotation curve, instead of a decrease. This leads to the conclusion that the galaxy's mass surpasses what can be accounted for by its luminosity alone. Further research suggests that galaxies are surrounded by an extensive halo of non-luminous matter, which extends beyond the galaxy itself. In Figure 4.1 the rotation curve for NGC 3198 is shown. By adding a halo model, representing the DM, to the galaxy (disk), the flattening can be accounted for.

4.1.2 Gravitational Lensing

By the principles of general relativity, the presence of massive objects can cause the curvature of space-time, leading to the bending of light. Consequently, the gravitational influence of massive objects, such as galaxies, can mimic the behaviour of optical lenses, causing distortions in the appearance of celestial objects. This phenomenon is referred to as gravitational lensing.

In the case of two galaxies (one in the foreground and the other in the background), the background galaxy gets distorted according to the foreground galaxy and their relative positioning in the line of sight. A particular case happens if both

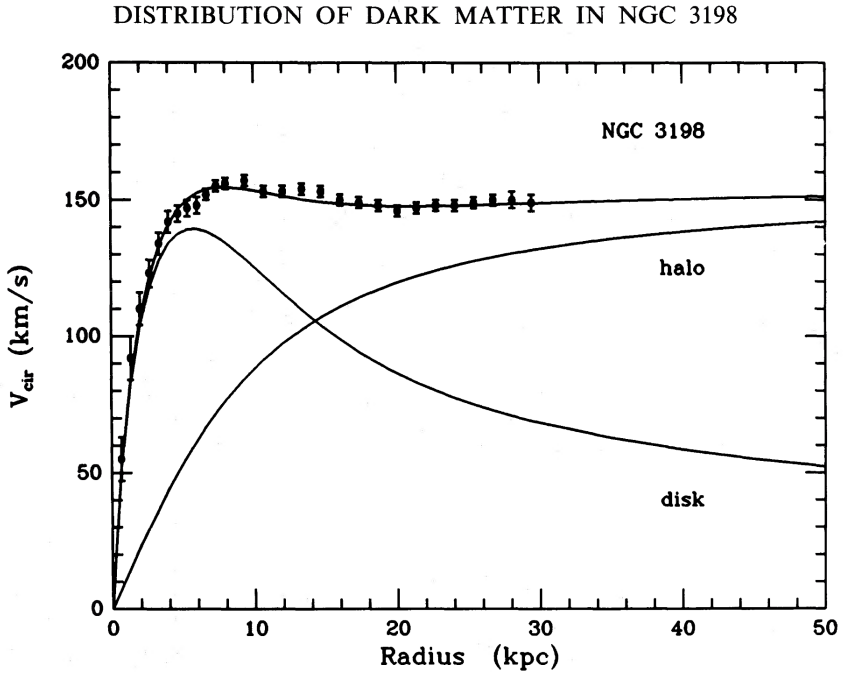

Figure 4.1: Observed rotation speed (black dots) for the galaxy NGC 3198. The expected rotation speed for the galaxy (line labelled disk) and a halo model (line labelled halo) is shown. The halo model was fitted to the data. The figure is taken from [29].

galaxies lay in the line of sight. The background galaxy gets distorted into a ring, the so-called Einstein ring. An almost perfect example of an Einstein ring is shown in Figure 4.2.

By investigating a distorted image, the mass of the lens can be derived. The distortion (θ_{E}) is proportional $\sqrt{M}$ see Equation 4.1. Therefore, by comparing the calculated mass with luminous mass, the amount of dark matter can be estimated.

$$\theta_{\mathrm{E}} = \sqrt{\frac{4GM}{c^2}\frac{D_{\mathrm{LS}}}{D_{\mathrm{L}}D_{\mathrm{S}}}} \tag{4.1}$$

4.1.3 Cosmological Evidence

According to our current understanding, the galaxy started with the Big Bang. The Big Bang Theory states that the universe was compressed into an infinitesimal small point. Following this, the universe expands till today but at different rates at different times. The older the universe gets, the colder it becomes and the formation of bound particle states becomes possible (quarks to hadrons to atoms). After 380,00 years, the universe was cold enough for atoms to form. This period is called the epoch of recombination. The universe was opaque beforehand, and now photons can travel freely through the universe. These photons can now be observed as the cosmic microwave background (CMB). The CMB has an approximate temperature of (2.7300 ± 0.0005) K. In Figure 4.3 a plot of the temperature fluctuation is shown. The Big Bag can be described by the ΛCDM model, which has the baryon density $\Omega_{\mathrm{b}}h^2$ and the dark matter density $\Omega_{\mathrm{dm}}h^2$ as parameters.

The CMB map can then be separated into its spherical harmonic components and from this, the CMB anisotropy power spectrum is derived (see Figure 4.4).

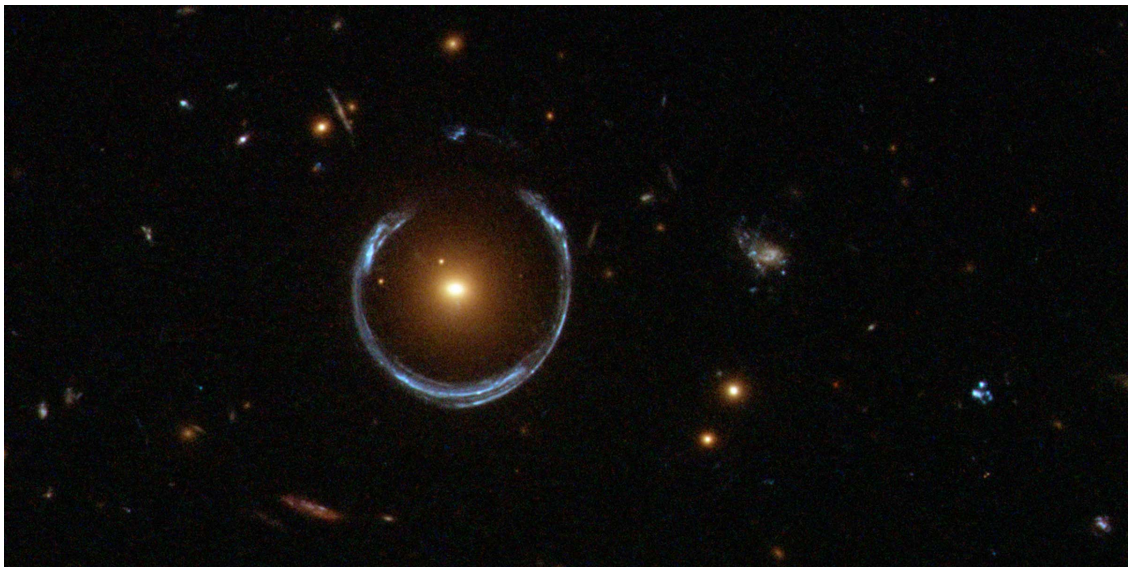

Figure 4.2: The red galaxy in the foreground distorted light from a more distant blue galaxy. Both galaxies are aligned in an almost perfect, straight line from our perspective. This makes the background galaxy appear as a ring (Einstein ring). Taken from [30].

From the ΛCDM the theoretical CMB anisotropy power spectrum is obtained and can be fitted to the measured values. Following the fit, the results give values for $\Omega_{\mathrm{b}}h^2$ and $\Omega_{\mathrm{dm}}h^2$, in particular $\Omega_{\mathrm{dm}}h^2 \neq 0$.

4.1.4 Bullet Cluster

The last piece of evidence presented is by analysing the bullet cluster. The bullet cluster consists of two galaxy clusters, which collided some time ago (see Figure 4.5) During the passing, hot gas got compressed between them and emitted X-rays (red area in Figure 4.5). The X-ray emitting area represents the space with the highest baryonic matter density. The centre of the total mass of the cluster can also be derived by looking for the position of weak gravitational lensing (blue area in Figure 4.5). By comparing these two regions, a discrepancy can be seen. This can be explained by additional non-baryonic matter (DM).

With this analysis, one can also exclude the modified Newtonian dynamics (MOND), which was an alternative theory to DM. MOND explained the rotation curves of galaxies by modifying Newton's law of universal gravitation. MOND is unable to explain the bullet cluster.

4.2 Dark Matter Candidates

From our observation (lack of observation) three characteristics are needed for a DM candidate:

- non-baryonic:
  Only weakly interacting and therefore not carrying any electric charge and colour charge.

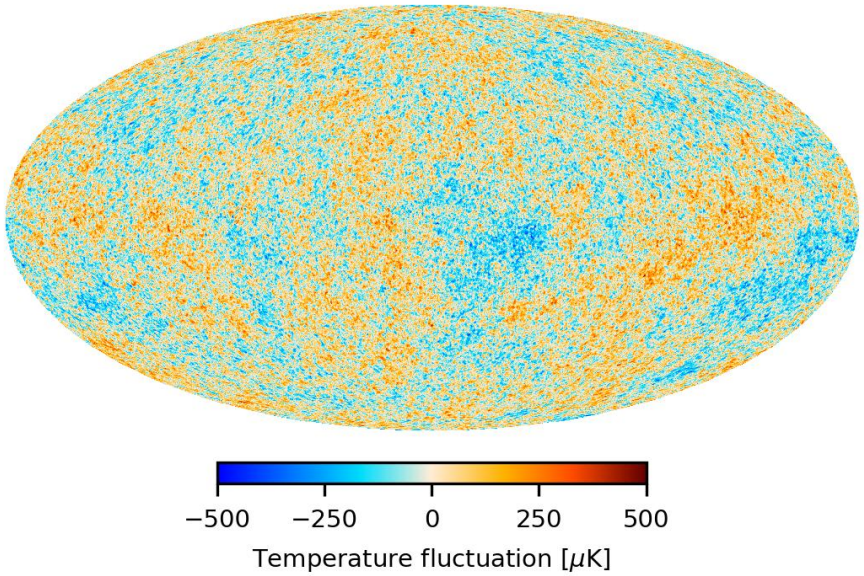

Figure 4.3: Map of the cosmic microwave background temperature fluctuation. The average temperature is approximately 2.73 K and fluctuates about 500 μK. The data is taken by the Planck spacecraft.

- stable:
  DM particle were created at the Big Bang and should be stable or have a very large lifetime (much larger compared to the age of the universe).

- non-relativistic (and therefore massive)
  Relativistic particle are unable to explain the gravitational potential, which resulted in our current observable universe. Neutrinos are ruled out with these characteristics.

In the following sections, two different possible DM candidates will be discussed.

4.2.1 Axions

The quantum chromodynamic (QCD) lagrangian predicts strong charge-parity violations. The Lagrangian term depends on $\bar{\theta}$, which is related to the QCD vacuum. From $\bar{\theta}$ the neutron electric dipole moment can be derived, which results in $\bar{\theta} < 10^{-10}$. Fixing this fine-tuning problem, by creating a spontaneous symmetry breaking, predicts a new particle, the axion.

The axion is a light electric neutral, and weakly interacting particle. Therefore, a good candidate for DM.

4.2.2 WIMP

An extensive class of particles considered for DM are weakly interacting massive particles, short WIMPs. In the following sections, two WIMP candidates will be discussed, proposed by supersymmetry (SUSY) extension to the Standard Model (SM) and Kaluza-Klein theory (KK theory). Beforehand, the process of thermal freeze-out will be explained.

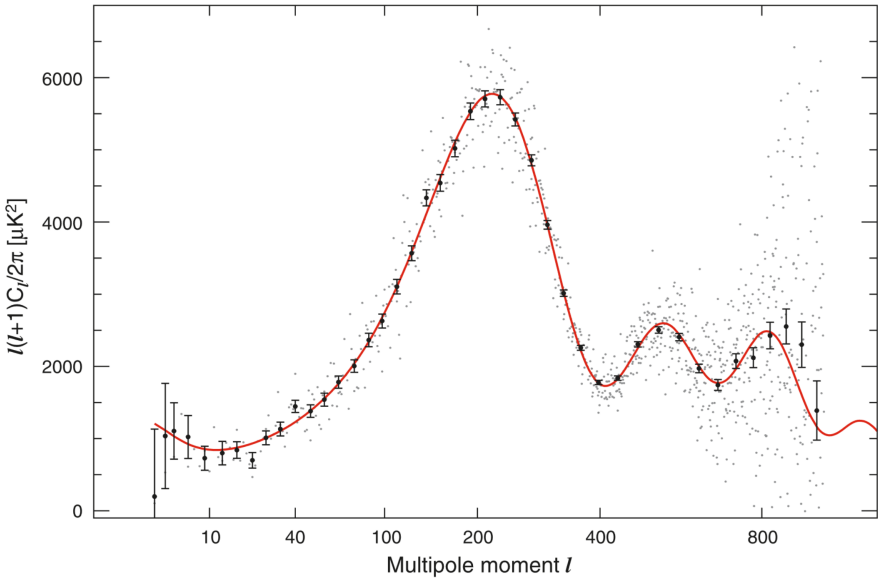

Figure 4.4: The temperature angular power spectrum with the best-fit values for the ΛCDM model (red line). The grey dots represent the measured data and the black the binned data. Taken from [31].

Thermal Freeze-Out

The early universe consisted of hot and dense plasma. If WIMPs exist, then one can assume that in the plasma the production and annihilation of WIMPs were in an equilibrium. As time moved on, the universe expanded and cooled down. This results firstly in a disruption of the equilibrium, because the energy was too low for WIMP production. Secondly, the annihilation of WIMPs is reduced because of the expanding space. Henceforth, the WIMP density approaches a constant value (relic abundance). One can derive $\langle \sigma v \rangle_{\text{thermal relic}} \approx 3 \times 10^{-26}\,\text{cm}^3\,\text{s}^{-1}$ for the self annihilation cross-section. This is what one predicts for particles with electroweak scale interacted. This result gets referred to as WIMP Miracle.

Super Symmetry

By adding another symmetry to the SM, one can easily derive a DM candidate. By proposing a symmetry between fermions and bosons, giving each particle an opposite partner, one expands the SM with SUSY. SUSY solves the hierarchy problem. The measured mass of the Higgs boson is much smaller than expected. SUSY introduces new particles, which would correct the expected Higgs mass to the measured one. Another advantage of SUSY is, that it proposes a viable DM candidate. The neutralino $\chi_1^0 \cdots \chi_4^0$ is a particle state which is a superposition of the neutral superpartners of the Higgs and gauge bosons. The neutralino is stable, only interacts weakly and massive ($m_\chi > 46\,\text{GeV}$), thus, a good WIMP candidate.

Kaluze Klein Theory

A simpler extension to the SM is the Kaluza Klein theory (KK theory). The theory assumes an extra spatial dimension. The extra dimension is curled up into a circle with an extremely small radius R ($\sim 10^{-35}\,\text{m}$). Therefore, the extra dimension can't

Figure 4.5: A picture of the bullet cluster, which consists of two galaxy clusters. A region of hot gas (red area), which emits X-rays, was created during their collision. The location of weak gravitational lensing (centre of the total mass) is shown in blue. Taken from [32].

be observed. Particle are theoretically able to propagate through the dimension. The momentum would be quantized, and each particle has different KK states. By requiring translation invariance along the fifth dimension, a stable KK particle can be derived. The stable KK particle correspond to the first excited photon state and is a good WIMP candidate.

4.3 Dark Matter Detection

A possible interaction for DM is their destruction. In Figure 4.6 the Feynman graph for DM annihilation is shown (left to right). By rotating the Feynman graph by 90° the scattering process is shown, and by repeating the rotation the production graph is constructed. Depending on these three interactions, different detection strategies are used:

- Particle accelerators (Production, see corresponding interaction channel in Figure 4.6)
- Direct detection (Scattering, see corresponding interaction channel in Figure 4.6)
- Indirect detection (Annihilation, see corresponding interaction channel in Figure 4.6)

The different strategies are discussed briefly in the following sections.

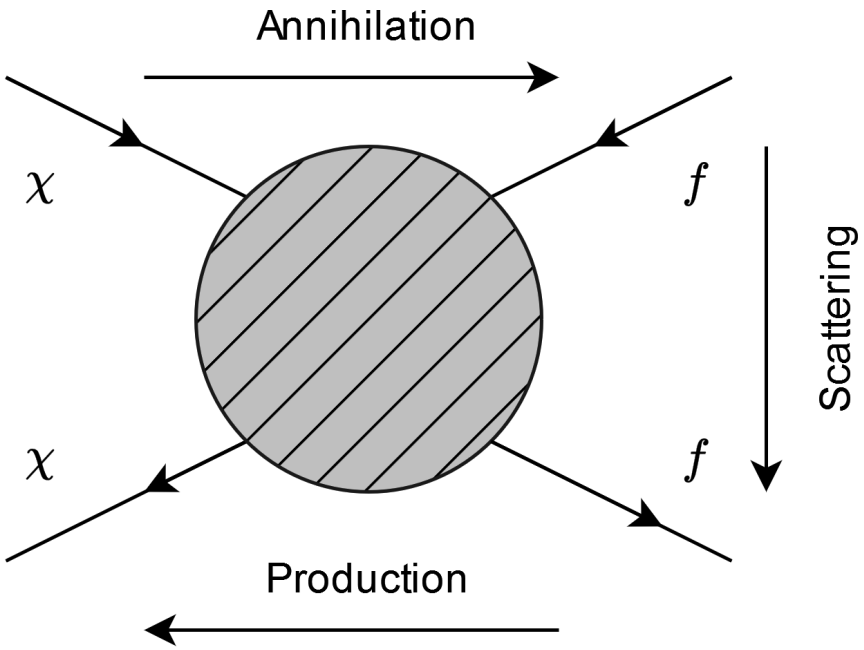

Figure 4.6: Possible interaction for a theoretical WIMP (χ). From left to right the annihilation channel is shown. A WIMP and anti-WIMP interact and annihilate themselves into any standard model particle (f) pair (e.g. $q\bar{q}$ or $\gamma\gamma$). From right to left the production channel is shown, where a f and $\bar{f}$ produce a WIMP pair. The WIMP scattering process is shown from top to bottom.

4.3.1 Particle Accelerator

In particle accelerators (e.g. LHC), particle-particle interactions are produced. In these interactions, DM could be created. The detectors are not able to detect them, but the missing energy and momentum can be detected. From this information, one can only derive a minimal lifetime of $\tau > 1 \times 10^{-7}\,\mathrm{s}$, which is much smaller than the required $\tau_{\mathrm{WIMP}} > 1 \times 10^{17}\,\mathrm{s}$. Nevertheless, the thermal relic density can be determined. If the thermal relic density agrees with the cosmologically observed density, it is strong evidence for dark matter.

4.3.2 Direct Detection

Direct detection experiments aim to detect DM scattering on nuclei. The expected recoil energy is relatively low ($\sim 100\,\mathrm{keV}$) and therefore a very sensitive detector with low background is needed. By building them underground, the background gets reduced. An unsolvable problem are the atmospherical neutrinos, which set a lower limit for the direct interaction cross-section (σ_{SC}) An example is the XENON1T detector. The detector is made out of liquid xenon, which theoretically produces photons by interactions with DM. XENON1T examines the parameter space up to $\sigma \sim 2 \times 10^{-47}\,\mathrm{cm}^2$ [33]. The current and future constraints on the scattering cross-sections are shown in Figure 4.7.

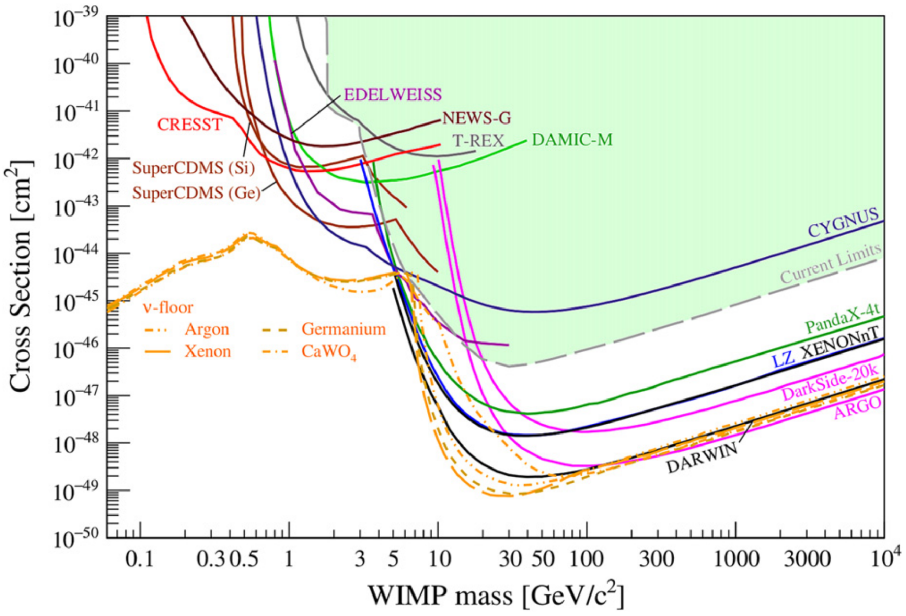

Figure 4.7: Current constraints on the scattering cross-section (spin-independent) of WIMPS. The neutrino scattering background curve is shown in orange. Taken from [34].

4.3.3 Indirect Detection

In the case of indirect detection, one tries to observe the resulting particles from DM annihilation.

If the DM particles decay into neutrinos, an excess flux from the sun is expected. From theoretical calculations, the neutrino flux resulting from DM annihilation depends only on the scattering cross-section. For that reason, by detecting an excess neutrino flux from the sun, the scattering cross-section can be constrained.

A way to derive the annihilation cross-section is by detecting particles beside neutrinos directly. Anomalies of particle fluxes can be interpreted as potential DM sources.

Lastly, a gamma ray flux caused by the DM decay products can be detected. DM can theoretically also decay into two photons, but this process is highly suppressed. The gamma-ray flux can be detected by ground-based (Fermi-LAT) or space-based (CTA) telescopes. By looking at region with a high DM density (dwarf galaxies, galaxy clusters or the galactic centre), the likelihood of significant detections are increased. In Figure 4.8 the current annihilation cross-section upper limit for the $b\bar{b}$-channel is shown. The potential gamma-ray fluxes for different decay channels are discussed in the next section.

4.4 Annihilation Spectrum of WIMPs

The annihilation spectrum for WIMPs depends on the channel into which the DM particle annihilates. Every particle from the SM is possible as long as $m_{\mathrm{SM}} < m_{\chi}$ is valid. In Figure 4.9 the gamma-ray spectrum for a DM particle with a mass $M_{\mathrm{DM}} = 100\,\mathrm{GeV}$ for different products are shown. The simulation of the spectra are done with `CLUMPY` [36, 37]. The spectra show an expected cutoff at the mass of the DM particle. The $b\bar{b}$-channel is commonly used in the literature for the GeV energy

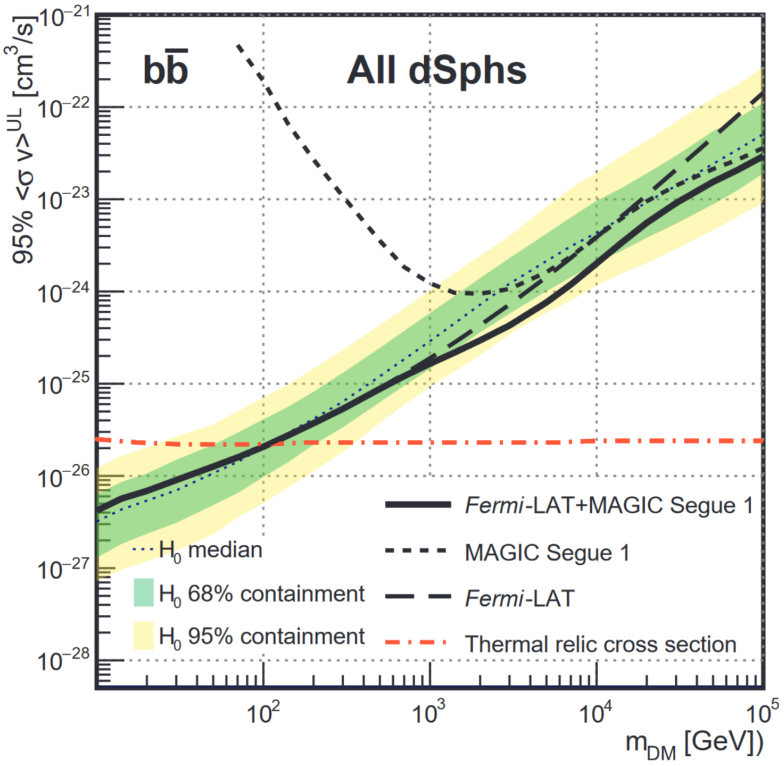

Figure 4.8: Upper limits to the annihilation cross-section for the $b\bar{b}$-channel. The limits are derived by analysing the combined data from MAGIC (a current IACT) and Fermi-LAT. Taken from [35].

range [38, 39, 40] and therefore used for future analysis.

4.5 Differential Flux of Emitted Photons

The gamma-ray flux resulting from DM annihilation for extra galactic sources is calculated by following equation

$$\left\langle \frac{\mathrm{d}^2\Phi}{\mathrm{d}E_\gamma \mathrm{d}\Omega} \right\rangle_{\mathrm{sky}} = \underbrace{\bar{\varrho}^2_{\mathrm{DM},0} \times \int_0^{z_{\max}} c\mathrm{d}z \frac{(1+z)^3}{H(z)} \left\langle \delta^2(z) \right\rangle}_{\text{cosmological-related parameters}} \cdot \underbrace{\frac{\mathrm{d}\Phi_\gamma^{PP}(E,z)}{\mathrm{d}E}}_{\text{source spectrum}}, \tag{4.2}$$

where E_γ represents the observed energy, $\mathrm{d}\Omega$ the elementary solid angle, $\bar{\varrho}^2_{\mathrm{DM},0}$ represents the current DM density of our universe, c the speed of light, $H(z)$ the Hubble constants at the redshift z, $\langle \delta^2 \rangle = 1 + \mathrm{Var}(\delta)$ the intensity multiplier to the DM inhomogeneity δ and $\frac{\mathrm{d}\Phi_\gamma^{PP}(E,z)}{\mathrm{d}E}$ the source spectrum. The source spectrum depends on two terms. Firstly, it depends on a particle physics related part, which describes the shape of the spectra (see Figure 4.9), which depends on the annihilation channel of the DM particle. Secondly, a term related to the DM distribution. This factor is referred to as J-factor. The J-factor related part only scales to spectrum by a scalar quantity.

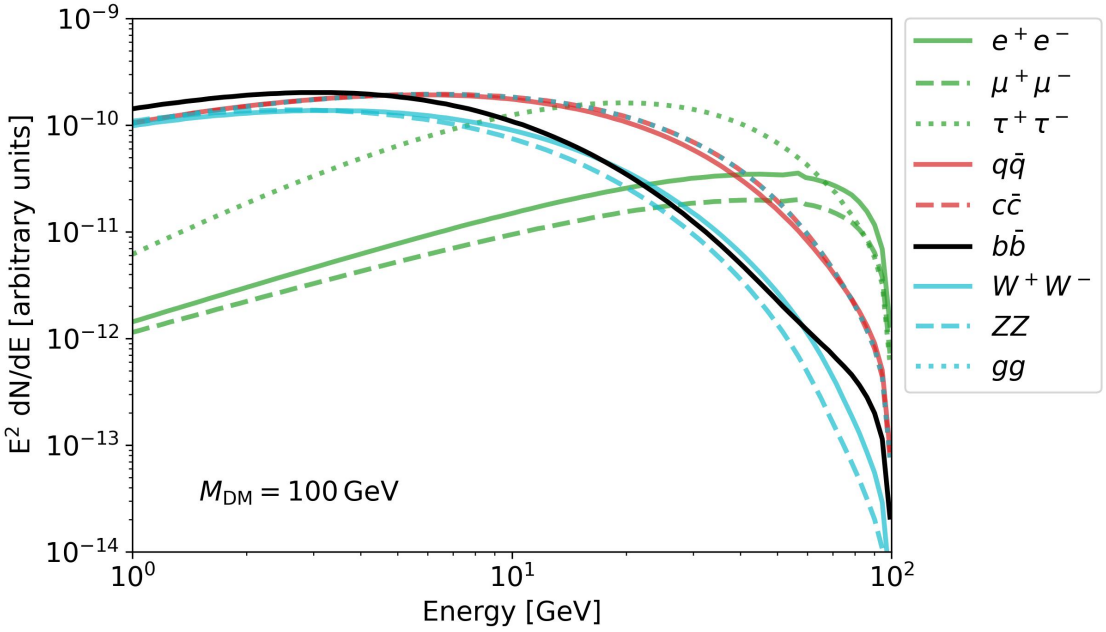

Figure 4.9: DM annihilation spectrum for different decay channels. The DM mass is assumed to be 100 GeV. Shown are the leptonic decay channels without neutrinos (green lines), the quark decay channels with $q = u, c, d$ (red lines), and the gauge bosons without photons (cyan lines). For the future analysis the $b\bar{b}$-channel is used.

4.6 Dark Matter Distribution

For the calculation of the J-Factor, the underlying DM distribution is needed. The distribution cannot be detected, therefore it is simulated. For simplicity, a radial symmetry is assumed for all density profiles. The first density profile was proposed by Nacarro, Frenk and White (NFW [41]). The model results from N-body simulations. The NFW-profile can be labelled as a cusped profile, which refers to a highly dense centre region. Other models in the category are the Einasto-profile and the Moore-profile.

In comparison to the cusped profile are profiles with a flat density profile in the centre. They are motivated by observations of dwarf galaxies, where a flat density profile is expected. Examples for such models are the Burkert-profile and Isothermal-profile.

The profiles are shown in Figure 4.10. The profiles are scaled to a density of $\rho = 0.3\,\mathrm{GeV\,cm^{-3}}$, which is commonly used in literature as DM density in the vicinity of our on solar system [42], at a distance of 8.33 kpc from the galactic centre. The equations with their respective parameters are shown in Table 4.1. The DM profile is referred to as DM halo. For further analysis a NFW-profile with $r_s = 18.9\,\mathrm{kpc}$ and $\rho_s = 2 \cdot 10^6\,\mathrm{M_\odot/kpc^3}$ and an Einasto-profile with $r_s = 178\,\mathrm{kpc}$ and $\rho_s = 8.12 \cdot 10^3\,\mathrm{M_\odot/kpc^3}$ for the Andromeda Galaxy are used [23]. The profiles are shown in Figure 4.11.

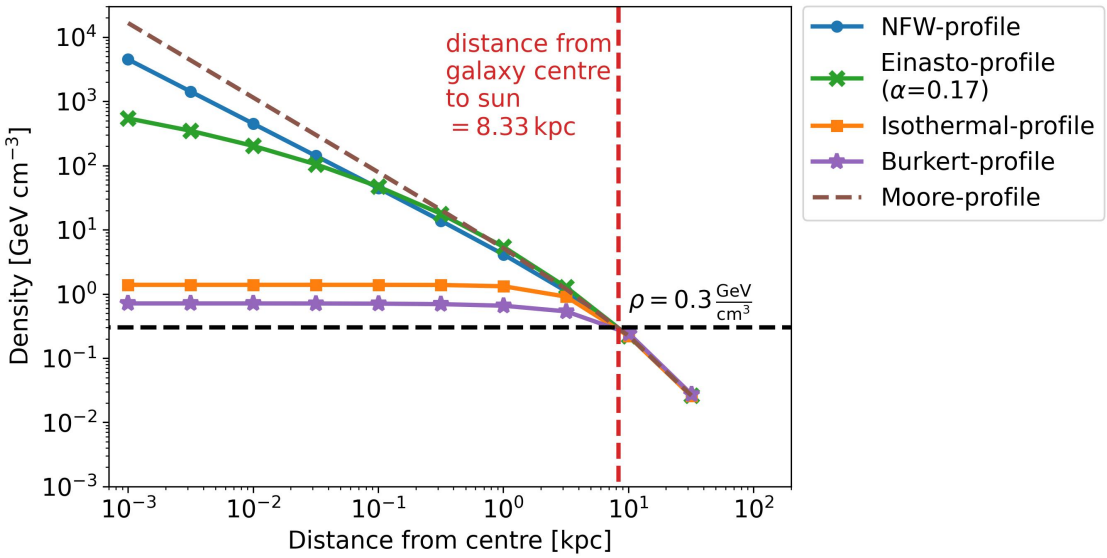

Figure 4.10: SM profiles for different proposed DM profile functions. The profiles are normalized to $\rho = 0.3\,\text{GeV}\,\text{cm}^{-3}$ at a distance equal to the distance from our galactic centre to our sun (8.33 kpc), which is a DM density expected at the vicinity of our own solar system. The exact values used are shown in Table 4.1.

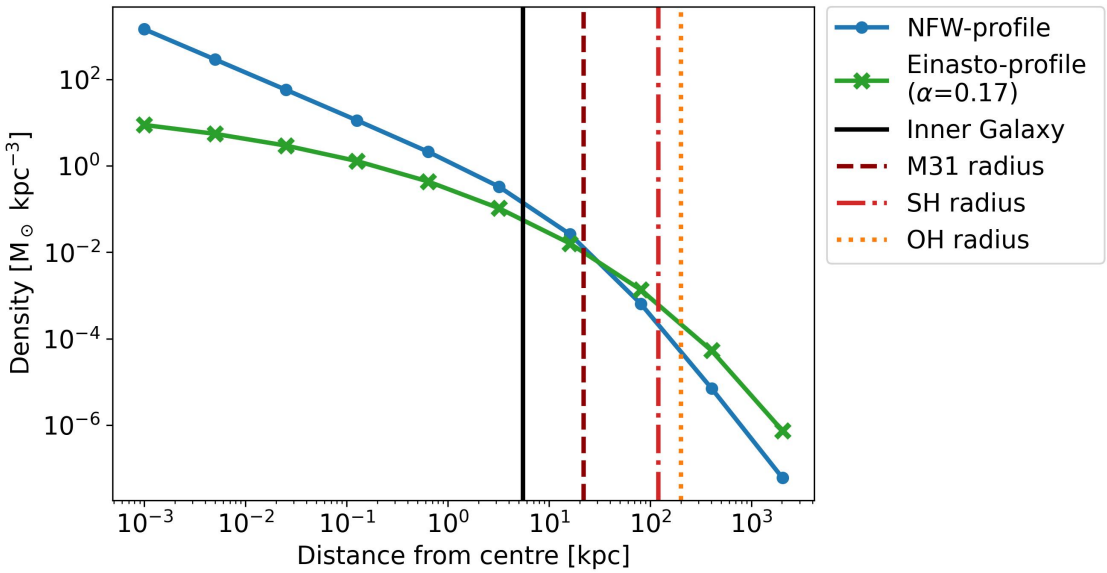

Figure 4.11: Dark Matter profiles used for further analysis (taken from [23]). The size of M31 and other important distances to halo companents of M31 are shown.

DM Halo	Equation	r_s[kpc]	ρ_s[GeV/cm^3]	α
NFW	$\rho_{\mathrm{NFW}}(r) = \rho_S \frac{r_s}{r}\left(1+\frac{r}{r_s}\right)^{-2}$	24.42	0.184	-
Einasto	$\rho_{\mathrm{Ein}}(r) = \rho_s \exp\left\{\left(-\frac{2}{\alpha}\left[\left(\frac{r}{r_s}\right)^{\alpha}-1\right]\right)\right\}$	28.44	0.033	0.17
Isothermal	$\rho_{\mathrm{Iso}}(r) = \frac{\rho_s}{1+(r/r_s)^2}$	4.38	1.387	-
Burkert	$\rho_{\mathrm{Bur}}(r) = \frac{\rho_s}{(1+(r/r_s))(1+(r/r_s)^2)}$	12.67	0.712	-
Moore	$\rho_{\mathrm{Moo}}(r) = \rho_s\left(\frac{r_s}{r}\right)^{1.16}\left(1+\frac{r}{r_s}\right)^{-1.84}$	30.28	0.105	-

Table 4.1: Different DM halo models with their respective equations. Also, parameters to scale the different DM models to $\rho = 0.3\,\mathrm{GeV\,cm^{-3}}$ at a distance equal to the distance from our galactic centre to our sun (8.33 kpc) are given, which is a DM density expected at the vicinity of our own solar system.

Chapter 5

Andromeda Galaxy Analysis

In this chapter, Fermi-LAT data of the region of interest (ROI), which includes the SH, for the Andromeda Galaxy is analysed. Firstly, the statistical method used in the analysis is introduced as well as the background models. After that, the analysis chain with `Fermipy` and `Gammapy` is explained. Further, different halo models with different spectral models are discussed and compared to the previously discussed explanations: DM profiles and CR Halos.

5.1 Binned Maximum Likelihood Analysis

In the case of Fermi-LAT, the data one receives are photon events with their associated direction. These events are then processed into a 3D-histogramm, where the region one observes is divided in spatial bins and energy bins with their corresponding event count. This section is based on [43].

In the next step, one can define several models, which predict gamma rays. By fitting the models simultaneously to the map, one obtains the best-fit model parameters. For this process the likelihood $L(\Xi)$ which depends on model parameters Ξ is defined as

$$L(\Xi) = \prod_{\mathrm{i}=1}^{\mathrm{N}} P(n_\mathrm{i}|\lambda_\mathrm{i}(\Xi)), \tag{5.1}$$

where the $P(n_\mathrm{i}|\lambda_\mathrm{i}(\Xi))$ represents the Poisson distribution (see Equation 5.2). The Poisson distribution gives the probability to measure n_i counts for the model prediction $\lambda_\mathrm{i}(\Xi)$ for the i-th pixel.

$$P(n_\mathrm{i}|\lambda_\mathrm{i}(\Xi)) = \frac{\lambda_\mathrm{i}(\Xi)^{n_\mathrm{i}}}{n_\mathrm{i}!} \cdot e^{-\lambda_\mathrm{i}(\Xi)} \tag{5.2}$$

With the likelihood, the total statistic TS value is defined as

$$TS = -2\ln(L(\Xi)) = -2\sum_{\mathrm{i}=1}^{\mathrm{N}} \ln\left(\frac{\lambda_\mathrm{i}(\Xi)^{n_\mathrm{i}}}{n_\mathrm{i}!} \cdot e^{-\lambda_\mathrm{i}(\Xi)}\right). \tag{5.3}$$

For the fitting, the TS is then minimized, or the likelihood is maximized.

To compare two nested models (model parameters 1 are a subset of model parameters 2) one can calculate their total statistic difference ΔTS :

$$\Delta TS = TS_{\text{model 1}} - TS_{\text{model 2}}. \tag{5.4}$$

If Wilk's theorem applies, it states, that ΔTS is distributed like χ^2_k with k degrees of freedom [44]. Wilk's theorem only holds true if

- the number of events is large
- parameters are not close to values at the boundary conditions
- no degenerate model parameters exist.

One can then estimate the significance σ out of χ^2_k. At first one can calculate the result (p) of the survival function (SF) of χ^2_k. The SF $S(t)$ is defined as

$$S(t) = \int_t^\infty f(u)\mathrm{d}u = p \tag{5.5}$$

where in our case t is ΔTS and $f(u)$ is a probability density function (PDF) of χ^2_k, which is defined as

$$\chi^2_{\text{PDF}}(x,k) = \frac{1}{2^{\frac{k}{2}}\Gamma\left(\frac{k}{2}\right)} x^{\frac{k}{2}-1} e^{-\frac{x}{2}} \tag{5.6}$$

with

$$\Gamma(x) = \int_0^\infty t^{x-1} e^{-t}\mathrm{d}t \tag{5.7}$$

being the gamma function, which is an analytic continuation of the factorial function $\Gamma(n) = (n-1)!$. Then, by taking the inverse survival function, which has the same form as the SF just with the limits from $-\infty$ to t, with $0.5p$ and the normal distribution (see Equation 5.9 with the parameters $\mu = 0$, $\sigma = 1$ and $A = 1$) as PDF, one gets an estimate for the significance. If the number of free parameters is one ($k = 1$), the estimation can be simplified to

$$\sigma = \sqrt{\Delta TS}. \tag{5.8}$$

One has to keep in mind that the significance can only be used to test the null hypothesis, by either reject or accept it. This does not mean that the null hypothesis or the other model describe the phenomena accurately.

$$g(x|\mu,\sigma,A) = \frac{A}{\sqrt{2\pi\sigma^2}} \cdot \exp\left(-\frac{1}{2}\left(\frac{x-\mu}{\sigma}\right)\right) \tag{5.9}$$

5.2 Background Models

During the modelling, one has to take into account background events. These background events can be described by two background models, the galactic background and the isotropic background. The galactic background describes the diffuse gamma-ray emission resulting from various processes from our own galaxy. The version `gll_iem_v07.fits` is used and is explained in more detail in [45].

The isotropic background consists of extragalactic gamma rays and, as the name suggests, is distributed isotropically over the sky (see [45] for more details). The version used in this thesis is `iso_P8R3_SOURCE_V3_v1.txt`.

5.3 Data Pre Fitting With Fermipy

At first, `Fermipy` is used to convert the Fermi-LAT data into a gamma astro data format (GADF). `Fermipy` is an open-source package adapted to be used for analysis of data collected from Fermi-LAT [46]. The data is taken from the Fermi-LAT website[1]. The sources used are taken from the LAT 12-year Source Catalogue (`4FGL-DR3`) [47]. The parameters used for data selection and reduction are shown in Table 5.1.

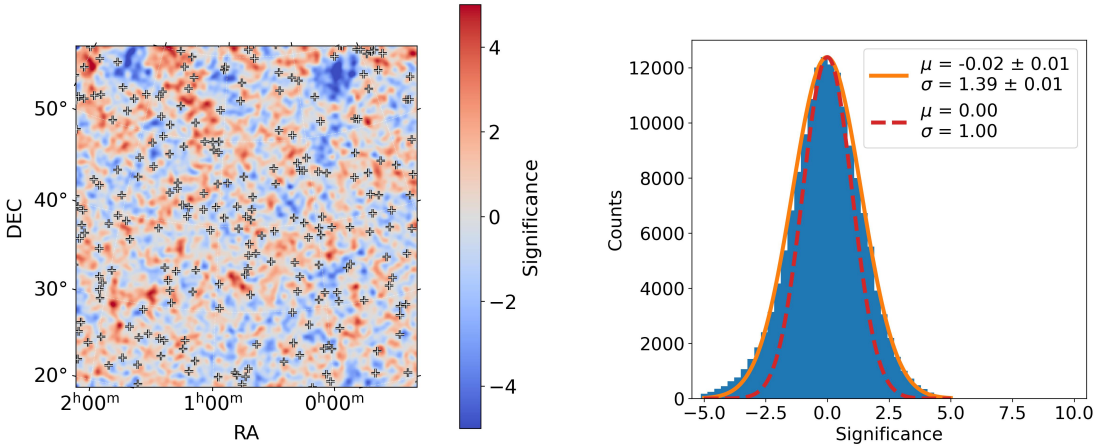

(a) Significance map (correlation radius of 0.3°). **(b)** Significance distribution.

Figure 5.1: **(a)**: LiMa Significance map of the ROI after fitting all models in `Fermipy` with a correlation radius of 0.3°. The plus signs represent a source from the catalogue. **(b)**: Distribution of the significance from the significance map. Also shown is the normal distribution (see Equation 5.9) fit to the data (orange line) with a normal distributed with $\sigma = 1$ and $\mu = 0$ for comparison (red dotted line).

For analysis of the SH of M31 only a ROI of 30° × 30° is needed, but since the Fermi-LAT has a huge PSF ($\sim$ 3° at energies around 1 GeV) models outside the ROI have to be modelled, due to leakage inside the ROI. In `Gammapy` an edge cut is applied, as models outside the ROI are not included. The background models discussed in the previous section are also needed for the data evaluation. In `Fermipy` the ROI is optimized, where sources are frozen with minimal/maximal TS of -1/4 or with a distance of the source bigger than 10°. For the optimization, the amplitudes of the free sources are fitted. The data are then exported for a more convenient use to `Gammapy`. In Figure 5.1 the significance map (**a**) and corresponding significance distribution (**b**) after the fit are shown. The significance is calculated as in [48] with a correlation radius of 0.3°, which is referred to as LiMa significance. If the models were perfectly describing the ROI, only statistical fluctuations would affect the significance distribution. Thus, the significance distribution adheres to a normal distribution with mean at zero and a standard deviation of one. The resulting standard deviation (see Figure 5.1 **(b)**) is $\sim$ 1.4, which is still in an acceptable range. Furthermore, a mean of -0.2 ± 0.1 suggest no further excess counts that are unaccounted for by the models. The fit is good enough to be used as a null hypothesis.

[1] `https://fermi.gsfc.nasa.gov/cgi-bin/ssc/LAT/LATDataQuery.cgi`

Configuration parameter	Value
Data selection	
Object name	Andromeda Galaxy (`4FGL J0043.2+4114`)
Observation time [MET]	239557417 - 710670377
Observation time [yr-m-d]	2008-08-04 - 2023-07-10
Energy range [GeV]	0.74989 - 133.35214
LAT data type	Photon
ROI	$40° \times 40°$
Data reduction	
IRF	`P8R3_SOURCE_V3`
Source catalogue	`gll_psc_v28.xml`
Spacial bin size	0.1°
Energy bins per decade	8

Table 5.1: Most important parameters used for data selection from the Fermi-LAT website[1] (Data selection) and for generating the data with `Fermipy` (Data reduction).

5.4 Data Analysis With Gammapy

The data cubes and IRF's from `Fermipy` are imported to `Gammapy`. `Gammapy` is an open-source python package for high level analysis of gamma-ray data [49, 50]. In Figure 5.2 the count map of the data imported from `Fermipy` is shown. The projection of the data is not considered and, therefore, the edge cut does not resemble a 5° cut at the edges. The edge cut includes most of the ROI, even though the data is not projected correctly on the 2-dimensional space. Since the projection is neglected, the circle, representing the SH, around M31 is not skewed. The differences resulting from the lack of projection can be neglected.

Models located within the SH and those which are uncategorized are both considered in the modelling process, since they have the potential to be part of the SH. For further fitting, these following models are considered:

- Background models:
  Two background models are used, the galactic and isotropic background (see section 5.2 for more details).

- Source galaxy:
  The Andromeda Galaxy model from `Fermipy` is adapted.

- Uncategorized sources:
  The uncategorized sources, located inside the SH, models are adapted from `Fermipy`. In the case of the Andromeda Galaxy, four sources are included with the following catalogue names `4FGL J0026.2+3926`, `4FGL J0039.7+4203`, `4FGL J0042.3+3509` and `4FGL J0112.0+3442`.

- Remainder sources in the ROI:
  All other sources, which aren't the source galaxy or uncategorized inside the SH, are modelled as a template model. This means the models are adapted from `Fermipy` and put together into a single background source. This model is then fixed during further fitting.

- SH model:
  The model describing the SH of the source galaxy. The specific SH model will be discussed in greater detail later in this section.

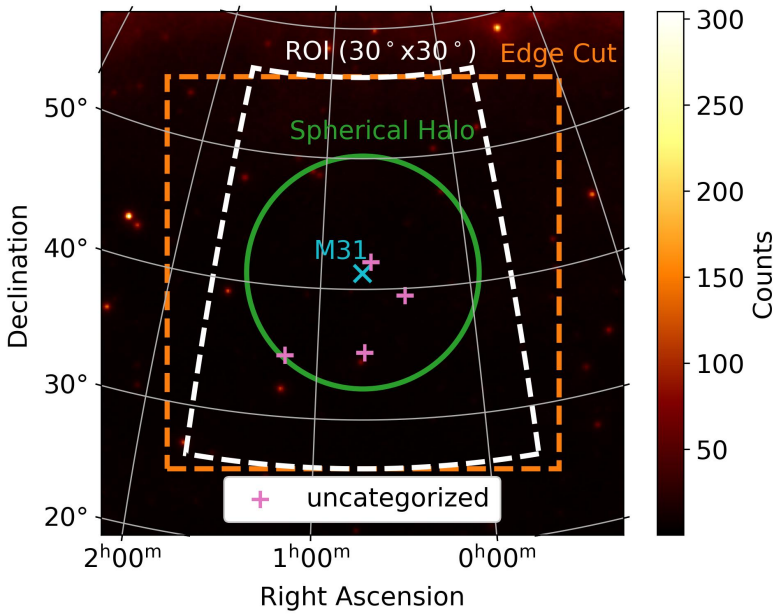

Figure 5.2: Counts Map from `Fermipy` with a $40° \times 40°$ ROI with the important sources shown. For `Gammapy` only a $30° \times 30°$ ROI is needed (white dotted line). Therefore, a spatial cut is applied (orange line), which is similar to the $30° \times 30°$. The source galaxy (M31) is shown in cyan with the SH in green. Also shown are the unknown sources in the SH (pink plusses).

Firstly, all the models except the SH model are fitted to get a flat significance map, which can be used as the null hypothesis. The resulting significance map (smoothing of 0.3°) and the associated spectral residual points are shown in Figure 5.3a and Figure 5.3b. The significance is fairly flat over the ROI, and the residuals fluctuate strongly for lower energies, but flatten for higher energies. The residuals are grouped in four energy bins (indicated by the black dotted lines) for better statistics in further analysis. In Table 5.5 the resulting normal distribution fit values are shown for the energy bins defined in Figure 5.3b. The fit in `Gammapy` improves the significance distribution yielded from `Fermipy`. The lower energy bin deviates the most from the normal distribution, but is still in an acceptable range. The resulting residuals are in an agreeable range and one can start to add the model for the SH.

For the SH, three different spectral models are considered: power law model (PWL-model), exponential cutoff power law model (EXP-model) and log parabola model (LOG-model). The corresponding equations are shown in Table 5.3.

The morphology of the halo is modelled as a flat disk with the radius r and centred around the position of the source galaxy, which is referred to as disk spatial model. This model is chosen since the flux is expected to be emitted uniformly in the disk. The edges are smoothed by the error function (see Equation 3.3).

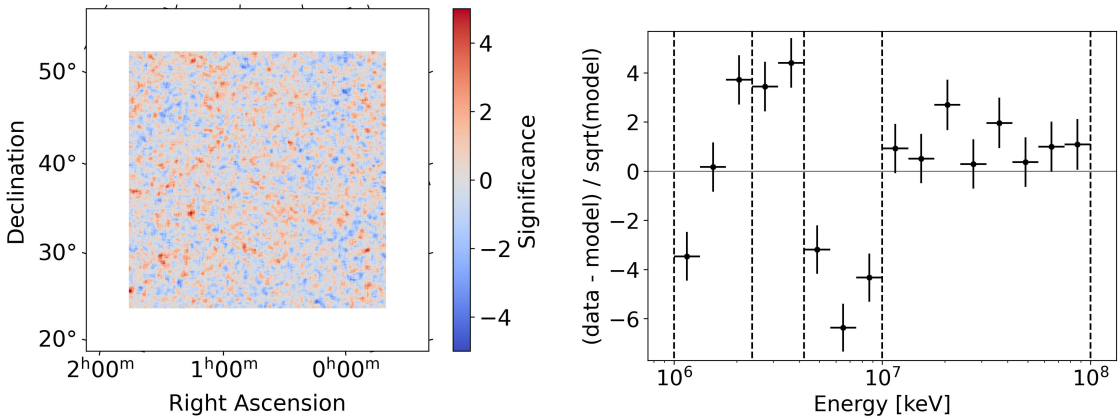

(a) Significance map (correlation radius of 0.3°). **(b)** Spectral residual points.

Figure 5.3: **(a)**: Significance map of the ROI with correlation radius of 0.3°. The significance represents the LiMa significance. **(b)**: Spectral residual points for the significance map. There are eight bins per magnitude, which are evenly distribution in log scale. The dashed black lines show the borders for the newly chosen energy bins (see Table 5.2).

Energy bin [GeV]	μ	σ
1 - 2.37	-0.016 ± 0.015	1.267 ± 0.015
2.37 - 4.22	0.252 ± 0.005	1.103 ± 0.005
4.22 - 10	-0.419 ± 0.005	1.046 ± 0.005
10 - 100	0.036 ± 0.005	1.060 ± 0.005

Table 5.2: Distribution of the LiMa significance in four different energy, chosen for better statistics (see Figure 5.3b). The expected distribution is a normal distribution with $\mu = 0$ and $\sigma = 1$.

The initial parameters for the spectral EXP-model are [6]:

$$\phi(E) = 9.8 \times 10^{-11} \left(\frac{E}{1\,\mathrm{GeV}}\right)^{-1.9} \cdot \exp\left(-\left(\frac{1}{11.6\,\mathrm{GeV}}E\right)^{1}\right) \cdot 3.42 \times 10^{-2}\,\mathrm{sr} \cdot \mathrm{GeV}\,\mathrm{cm}^{-2}\,\mathrm{s}^{-1}\,\mathrm{sr}^{-1} \cdot 2, \tag{5.10}$$

where the factor 2 takes into account that the whole SH is observed and not only the southern part, and $3.42 \times 10^{-2}\,\mathrm{sr}$ is the solid angle of the SH. For the PWL-model, the same function is used without the exponential term. The same amplitude is also used for the LOG-model, and the parameters are set to $\alpha = 2.3$ and $\beta = 0.5$. For the spatial model, the radius $r = 8.86°$ from Karwin et al. 2019 is adapted.

Six different cases are examined, using one of the three models with either a fixed spatial model radius (8.86°) or the radius as a free parameter. The resulting significances are presented in Table 5.3.

Spectral Model	**Equation**	**Significance σ for radius**	
		$r = 8.86°$ $(k = 3)$	**best-fit** r_{bf} $(k = 4)$
PWL-model	$\phi(E) = \phi_0 \left(\frac{E}{E_0}\right)^{-\Gamma}$	4.38	4.13 $(r_{\mathrm{bf}} = (8.983 \pm 0.011)°)$
EXP-model	$\phi(E) = \phi_0 \left(\frac{E}{E_0}\right)^{-\Gamma} \cdot \exp(-(\lambda E)^{\alpha})$	4.67	4.45 $(r_{\mathrm{bf}} = (9.01 \pm 0.24)°)$
LOG-model	$\phi(E) = \phi_0 \left(\frac{E}{E_0}\right)^{-\alpha-\beta \log\left(\frac{E}{E_0}\right)}$	5.61	5.44 $(r_{\mathrm{bf}} = (9.09 \pm 0.18)°)$

Table 5.3: Resulting significances (see section 5.1 for more details) for different spectral models with a disk spatial model either with a fixed radius to 8.86° or a best-fit radius r_{bf}. In the first case the number of free parameters is 3 and in the second case it is 4. The models examined are power law model (PWL-model), exponential cutoff power law model (EXP-model) and log parabola model (LOG-model). The corresponding equation for the spectral model is also listed.

For spectral comparison, each best-fit spectral model is shown in Figure 5.4. The PWL-model matches the model from Karwin et al. 2019 for lower energies (see Figure 5.4), but is unable to match higher energies. This outcome aligns with expectations, because the PWL-model is too simplistic to describe the SH. The two other models predict overall lower flux and also earlier cutoff energies. In the following part, the best-fit model (LOG-model with fixed radius) is discussed in greater detail.

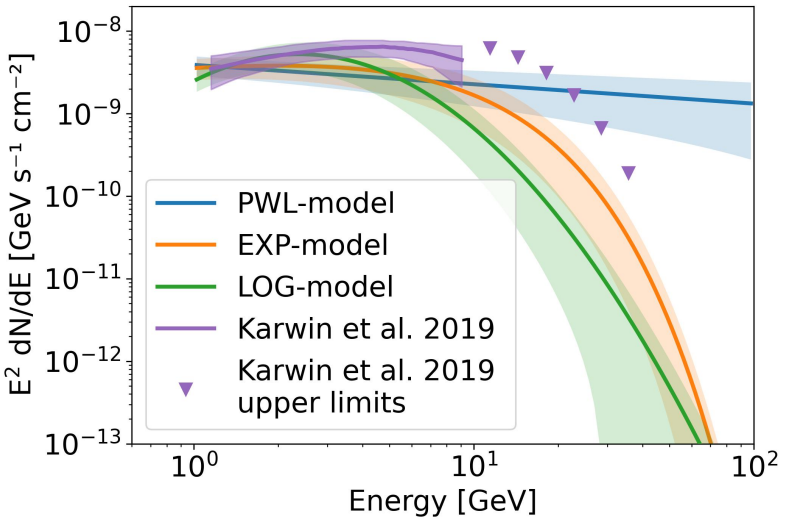

Figure 5.4: Spectral shape comparison of the different models to the best-fit model from Karwin et al. 2019. The shaded regions give the 1σ error band and downward pointing triangles give upper limits.

Parameter	Initial Value	Fit (fixed radius)	Fit (free radius)
Spectral Log Parabola Model			
ϕ_0 [MeV cm^{-2} s^{-1}]	6.7032×10^{-12}	$(2.5 \pm 0.7) \times 10^{-12}$	$(2.7 \pm 0.8) \times 10^{-12}$
E_0 [GeV]	1	-	-
α	2.3	2.71 ± 0.28	2.93 ± 0.28
β	0.5	1.0000 ± 0.0006	1.0000 ± 0.0002
Disk Spatial Model			
longitude (icrs)	$10°49'22''$	-	-
latitude (icrs)	$41°14'29''$	-	-
radius [°]	8.86	8.86	9.09 ± 0.18
Galactic Background			
norm	0.8972	0.972 ± 0.006	0.972 ± 0.006
tilt [10^{-2}]	1.353	4.8 ± 0.6	4.8 ± 0.6
E_0 [GeV]	1	-	-
Isotropic Background			
norm	1.224	1.07 ± 0.08	1.07 ± 0.07
tilt [10^{-2}]	0	1.8 ± 1.3	1.7 ± 1.1
E_0 [TeV]	1	-	-

Table 5.4: Model parameter values for the spectral LOG-model, the disk spatial model and the two background models. Given are the initial values, the values after the fit with a fixed radius (8.86°) and after the fit with the radius as a free parameter.

5.4.1 Log Parabola Spectral Model and Disk Spatial Model

The log parabola spectral model with fixed disk spatial model proved to be the best-fit model (see Table 5.3). Therefore, the analysis chain is discussed in greater detail in this section.

The initial parameters used and resulting best-fit model parameters are shown in Table 5.4. Also shown, are the normalization value, tilt value and the reference energy E_0 for both background models. One expects the normalization value to be located close to 1 and for the spectral tilt around 0. The background models are fitted to the entire ROI, and bigger deviations indicate some errors in the modelling process. All other models, which are not mentioned, have their amplitude as a free parameter, except the remainder sources in the ROI. No discrepancies are seen in the other free parameters, which indicate some problem in the fitting process.

In Figure 5.5 the significance map and the spectral residual points are shown. The distribution values for the four energy bins are shown in Table 5.5. The significance map and distribution values remain relatively similar to the results from the null hypothesis, but definitely don't worsen.

To get a measure of quality of the fit, one can examine the residual before and after the fit. The residual should be flattened after the fit. In Figure 5.5b a comparison of the residual before and after the fit in the area of the SH are shown. The residuals improve on average.

Another aspect to consider are the predicted counts from different sources. In this case, the counts from M31 and the SH are predicted. In Figure 5.6 a counts map of only the prediction of the corresponding source over all energy bins are shown. A ratio of 1:10 can be seen for predicted counts from galaxy to predicted counts from

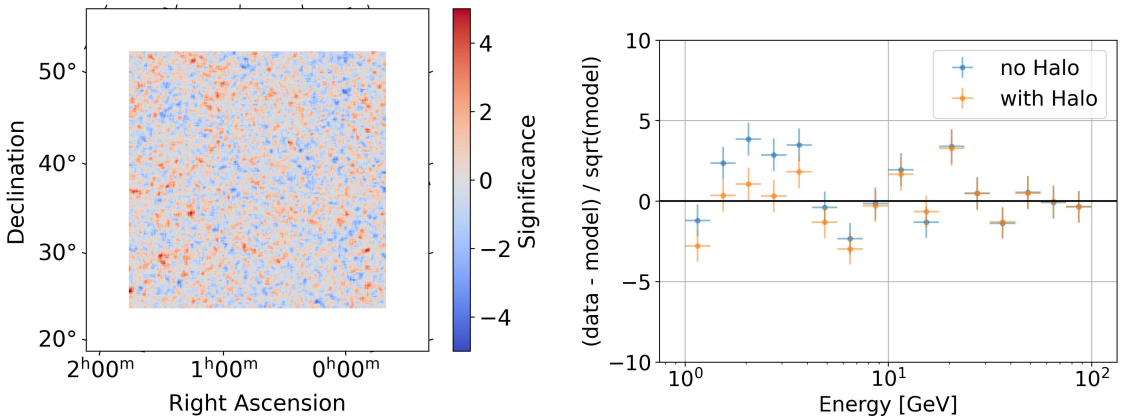

(a) Significance map (correlation radius of 0.3°).

(b) Spectral residual points.

Figure 5.5: **(a)**: Significance map of the ROI with correlation radius of 0.3°. The significance represents the LiMa significance. **(b)**: Spectral residual points inside the SH ($r = 8.86°$) region for the significance map before (without SH model) and after the fit (with SH model).

Energy bin [GeV]	μ	σ
1 - 2.37	-0.026 ± 0.015	1.250 ± 0.015
2.37 - 4.22	0.198 ± 0.005	1.091 ± 0.005
4.22 - 10	-0.408 ± 0.004	1.038 ± 0.004
10 - 100	0.065 ± 0.005	1.060 ± 0.005

Table 5.5: Distribution of the LiMa significance in four different energy, chosen for better statistics (see Figure 5.3b). The expected distribution is a normal distribution with $\mu = 0$ and $\sigma = 1$.

SH.

To further investigate the influence of the uncategorized sources, one can compare their fluxes. In Figure 5.7 are the fluxes shown for the diffuse background, the uncategorized sources, the source galaxy and the SH model. In the lower energy range (1 GeV to 10 GeV) all uncategorized models are insignificant in comparison to the SH model. Whereas, at high energies (10 GeV to 100 GeV) it is the other way around. This leads to the conclusion, that the uncategorized sources are not part of the SH.

Lastly, the flux points are calculated for six different energy bins, which were chosen for better statistics. The result is shown in Figure 5.8 with the best-fit model. For the lower energies (below 10 GeV) the flux points agree with the model from Karwin et al. 2019. At higher energies, the flux points visible deviate from the model. The flux points rather match a PWL-model. Another feature to be noticeable is that the flux points in the middle of the spectrum are less significant. This is referred to as dip and has been observed in different models resulting from analysis of Fermi-LAT data [51]. One possible explanation is that the dip results from some internal systematic errors in the `Fermipy` package. Another possibility is that the spectrum consists of two parts. The first one could dominate the lower energies, and the second one the higher ones. The first model drops before the second significantly rises, thus creating the dip. Overall, the results don't match with Karwin et al. 2019 and the LOG-model is preferred against the EXP-model

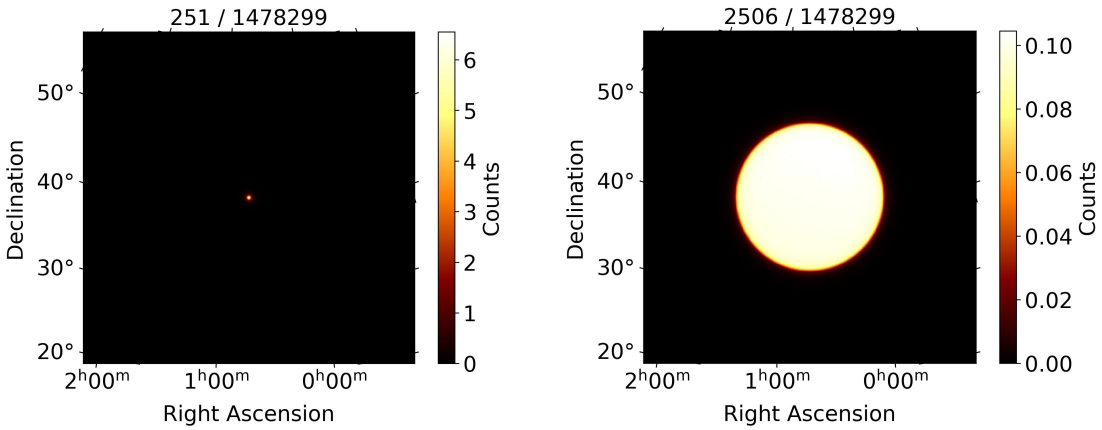

(a) Source galaxy (M31) **(b)** SH (LOG-model with spatial disk model)

Figure 5.6: Predicted counts for the Andromeda Galaxy **(a)** and the corresponding SH **(b)** after the first SH model fit to the data. The first number resembles the predicted counts from the source the second the total predicted gamma-ray count.

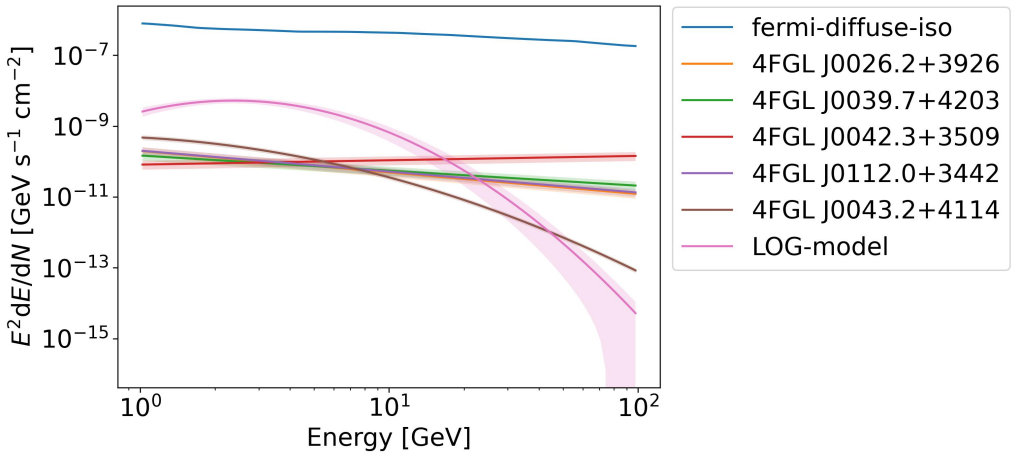

Figure 5.7: Gamma-ray spectra for the isotropic background model, the four uncategorized sources, the Andromeda Galaxy (4FGL J0043.2+4114) and the SH log parabola spectral model (LOG-model) are shown.

used in Karwin et al. 2019.

In the following two sections two possible explanations of the SH are investigated with the best-fit model and flux points.

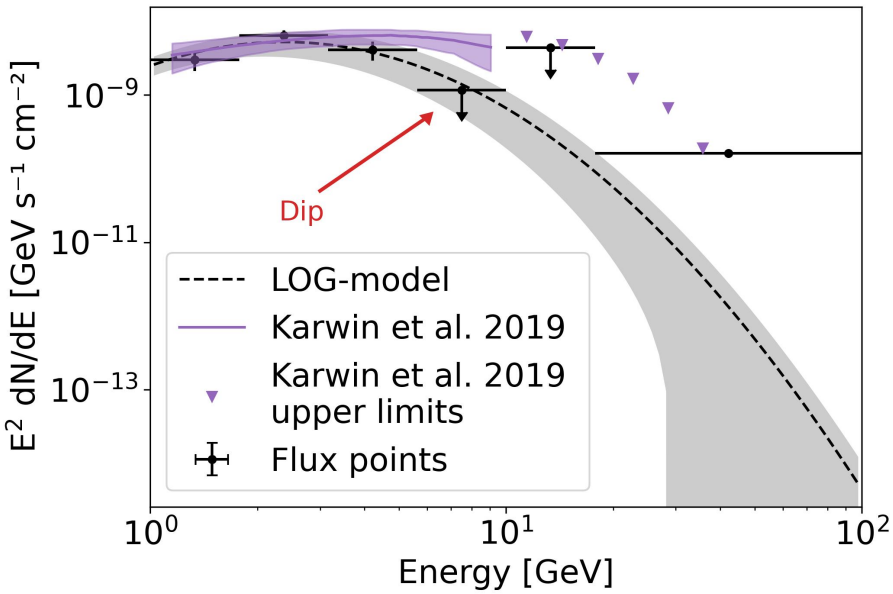

Figure 5.8: Best-fit LOG-model with the corresponding flux points. The flux points are calculated for six energy bins, which where chosen for better statistics. The spectrum plus flux points are compared to the spectrum from Karwin et al. 2019. Also, a visible dip in significance for the flux points is indicated (red arrow).

5.4.2 Cosmic Ray Halo

As discussed in subsection 3.3.2 and subsection 3.3.3, the spectrum observed in the SH region can be described by either a leptonic or hadronic source spectrum. For the M31, the source spectra are fitted to the flux points calculated in last section.

In the case of a leptonic source spectrum, errors are an order of magnitudes higher than the resulting flux and therefore is not discussed in greater detail.

The hadronic case yields useful results. In Figure 5.9 the resulting best-fit spectrum is shown on the right side with the source spectrum from Recchia et al. 2021 on the left side for comparison. The source spectrum is shown in Figure 5.10 with the source spectrum from Recchia et al. 2021 for comparison. The fit results in a high energy cutoff value ($\sim 23\,\mathrm{TeV}$). Hence, the exponential cutoff source spectrum can be approximated by a simple power law spectrum for the energy range from 1 GeV to 100 GeV. A PWL-model would match the flux points better. This can also be seen in Figure 5.10.

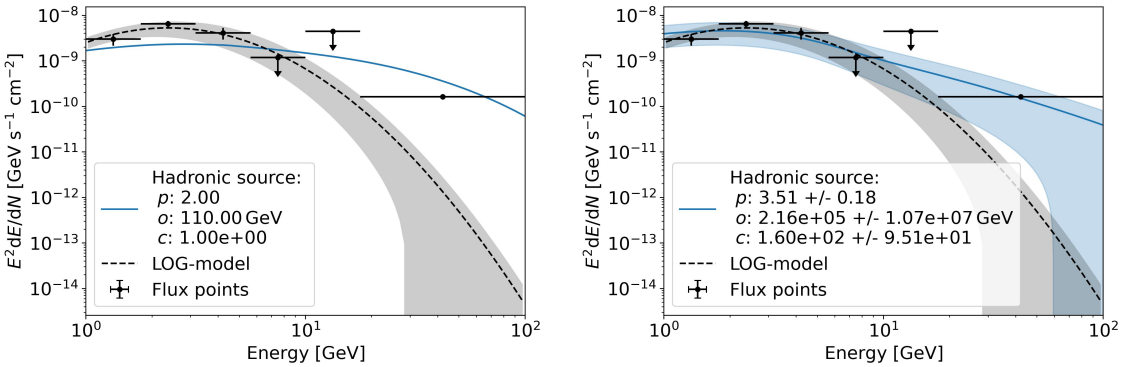

(a) Initial parameters from Recchia et al. 2021.

(b) Best-fit parameters.

Figure 5.9: Resulting gamma-ray spectrum from LOG-model with its flux points. The spectrum plus flux points are compared. The shaded region shows the 1σ error band. The spectrum is compared to **a**: Resulting gamma-ray spectrum from a hadronic source spectrum simulated with the initial parameters given in Recchia et al. 2021. **b**: Resulting gamma-ray spectrum from a hadronic source spectrum simulated with the best-fit parameters resulting from a fit to the flux points.

5.4.3 Dark Matter

Lastly, the LOG-model and the flux points are compared to the Dm halo models defined in section 4.6. For simple systematic estimations, the annihilation cross-section and DM mass are varied. For the cross-section the region $(2-4)\cdot 10^{-26}\,\mathrm{cm}^3/\mathrm{s}$ and for the mass $99-101\,\mathrm{GeV}$ are investigated. A qualitative comparison of the spectral shapes for the DM models and the LOG-model is shown in Figure 5.11. This looks promising and therefore, this can be seen as hint for DM gamma-ray origin but a more intricate DM models analysis has to be performed. If the phenomenon of the dip is a result of a two component spectrum, the DM models are unable to explain it.

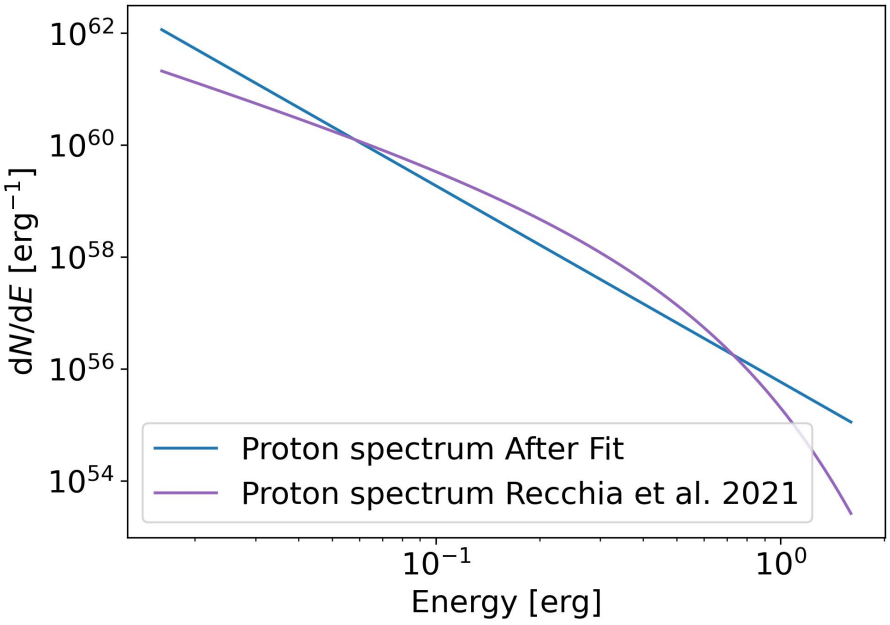

Figure 5.10: Source spectra for the parameters from Recchia et al. 2021 and the source spectrum resulting from fitting it to flux points of the best-fit LOG-model calculated in last section. The error band for the proton spectrum after fit are too small to be visible.

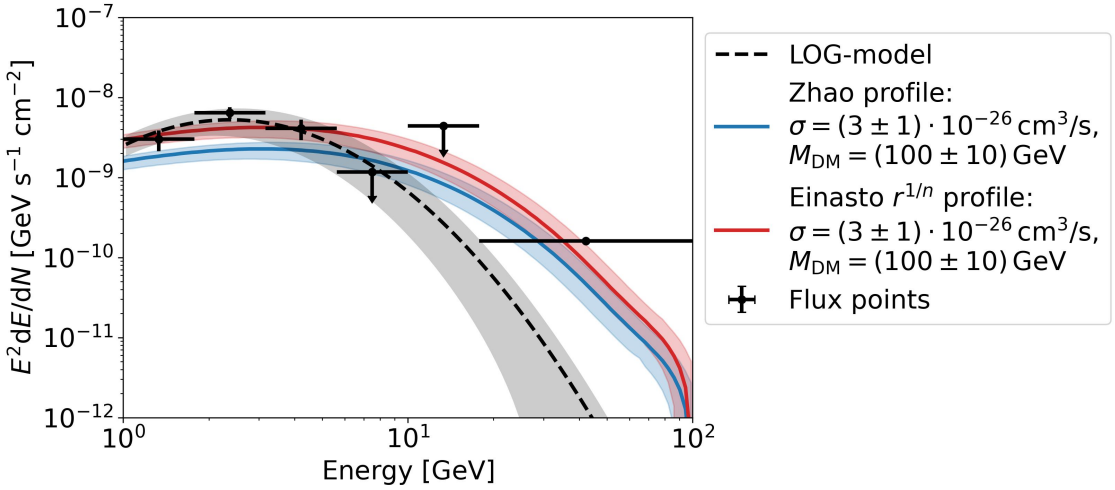

Figure 5.11: Spectral shape comparison of the two profiles (defined in section 4.6) to the best-fit LOG-model and the corresponding flux points. The error bands of the DM models are estimated by doing the simulation with the upper or lower errors of the annihilation cross-section σ and DM mass M_{DM}.

Chapter 6

Nearby Spiral Galaxies

The analysis of the SH is applied to other potential galaxies. In the first section, potential spiral galaxies are identified, and simple prediction about the expected fluxes and SH sizes are made. Afterwards, the potential candidates are discussed.

6.1 Prediction of Nearby Spiral Galaxies Candidates

The sensitivity curves discussed in section 2.2 only apply to point sources. The halo examined in the thesis is a hugely extended source (in the case of M31). For this reason, the sensitivity has to be adjusted by a scaling factor k for extended sources. The SH model from Karwin et al. 2019 give only upper limits after $\sim 10\,\mathrm{GeV}$ and hence one expects an intersection of the model with the sensitivity curve at that point. A simple assumption for the scaling factor would be $\propto \sqrt{\sigma^2_{\mathrm{source}} + \sigma^2_{\mathrm{PSF}}}/\sigma_{\mathrm{PSF}}$ [52], but this would overestimate the sensitivity curve. Therefore, scaling the proportionality by a factor smaller 1 would solve the problem. Yet, this would lead the scaling factor to be smaller than 1 and therefore better than a point source. That's why, following equation is used:

$$\kappa = \frac{\sqrt{(0.2 \cdot \sigma_{\mathrm{source}})^2 + \sigma_{\mathrm{PSF}}(E)^2}}{\sigma_{\mathrm{PSF}}(E)}. \tag{6.1}$$

To get a simple value defining detectability, the fraction of source model flux to sensitivity curve is calculated. A value of over 1 signifies a detectable flux. For the source model, the exponential cutoff power law from [6] gets adapted to

$$\begin{aligned}\frac{\mathrm{d}N(E)}{\mathrm{d}E} = &\left(9.8 \times 10^{-11} \cdot \left(\frac{E}{1\,\mathrm{GeV}}\right)^{-1.9} \cdot e^{-\frac{E}{11.6\,\mathrm{GeV}}}\right) \\ &\times (2 \cdot 3.42 \times 10^{-2}\,\mathrm{sr})\,\mathrm{MeV\,cm^{-2}\,s^{-1}\,sr^{-1}}.\end{aligned} \tag{6.2}$$

The equation can be simplified to

$$\frac{\mathrm{d}N(E)}{\mathrm{d}E} = \left(6.7 \times 10^{-12} \cdot \left(\frac{E}{1\,\mathrm{GeV}}\right)^{-1.9} \cdot e^{-\frac{E}{11.6\,\mathrm{GeV}}}\,\mathrm{MeV^{-1}\,cm^{-1}\,s^{-1}}\right). \tag{6.3}$$

In Figure 6.1 the exponential cutoff power law (labelled Power Law) with the sensitivity curve for the point source and the extended source (scaled with κ) for Fermi-LAT and the model from Karwin et al. 2019 is shown on the left side. On the right side is the resulting fraction shown. The same is shown for CTA in Figure 6.3. The expected spectrum is far below the sensitivity for CTA, and therefore CTA won't be considered any more. In the case of Fermi-LAT, the modelled spectrum is partly above the sensitivity as defined.

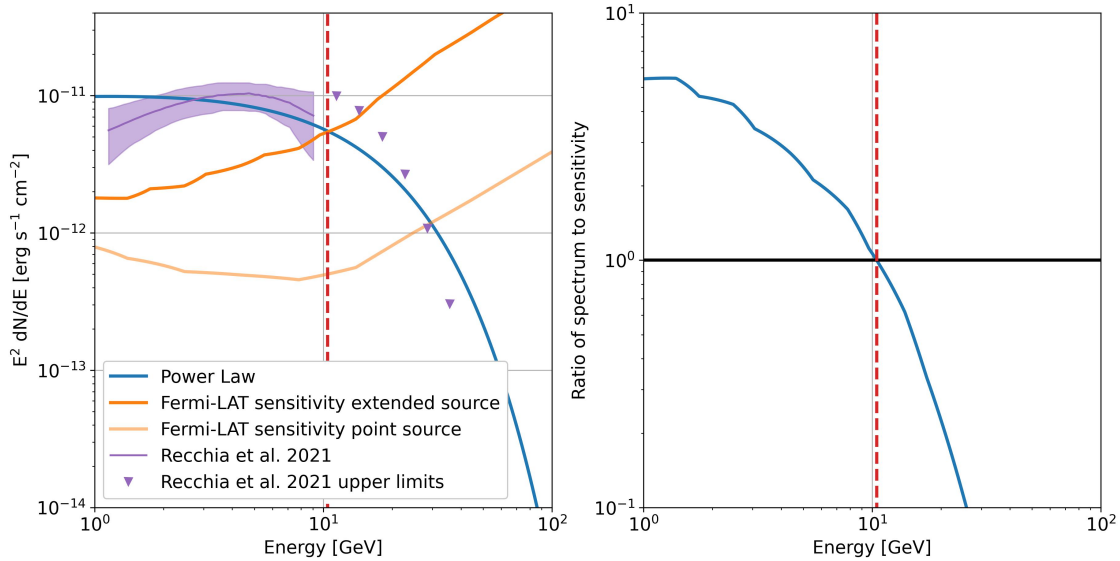

Figure 6.1: Left: The power law defined in Equation 6.3 is shown with the sensitivity for point sources and extended source, which is calculated by multiplying the sensitivity for point sources with κ (see Equation 6.1), for Fermi-LAT and the model from Karwin et al. 2019. The crosspoint of the power law with the extended source sensitivity is marked (red dotted line). Right: The fraction of the power law to the extended source sensitivity is shown.

To estimate the possibility of detecting SH for other galaxies, the spectrum gets scaled by two parameters depending on the galaxy's distance and the galaxy's size. In the first case, a proportionality of $\propto 1/d^2$ is assumed (see Equation 6.4). If the galaxy emits its flux isotropically, the proportionality should arise. In the second case, a proportionality of $\propto s^2$ is assumed (Equation 6.5).

$$k_{\text{distance}} = \left(\frac{d_{\text{galaxy}}}{d_{\text{M31}}}\right)^2 \tag{6.4}$$

$$k_{\text{size}} = \left(\frac{s_{\text{M31}}}{s_{\text{galaxy}}}\right)^2 \tag{6.5}$$

By applying the two scaling factor for all galaxies, the fractions are calculated. The results for Fermi-LAT and CTA are shown in Figure 6.3. For the CTA case, no possible candidates can be identified. In the Fermi-LAT case, one candidate reaches values over 1. This candidate is Messier 33 (M33) better known as Triangulum Galaxy. All other galaxies are below the value of 1 and are therefore not detectable. In Table 6.1 the six most promising candidates and the Andromeda Galaxy are shown with the most important NEARGALCAT data and some predicted values. In

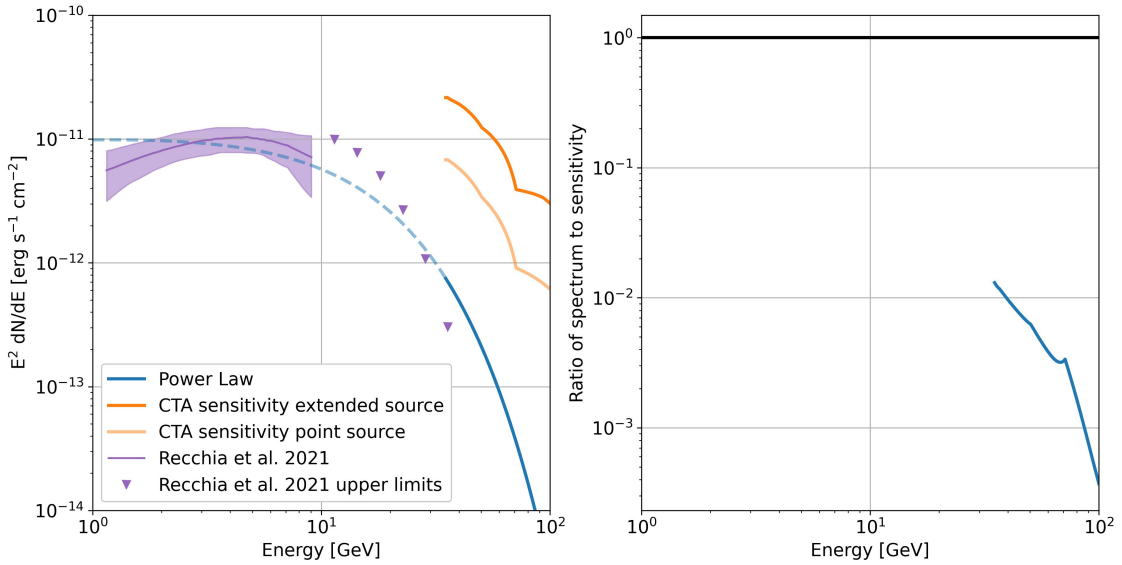

Figure 6.2: Left: The power law defined in Equation 6.3 is shown with the sensitivity for point sources and extended source, which is calculated by multiplying the sensitivity for point sources with κ (see Equation 6.1), for CTA and the model from Karwin et al. 2019. The crosspoint of the power law with the extended source sensitivity is marked (red dotted line). Right: The fraction of the power law to the extended source sensitivity is shown.

the next section, the candidates are analysed. Beforehand, some simple predictions are made.

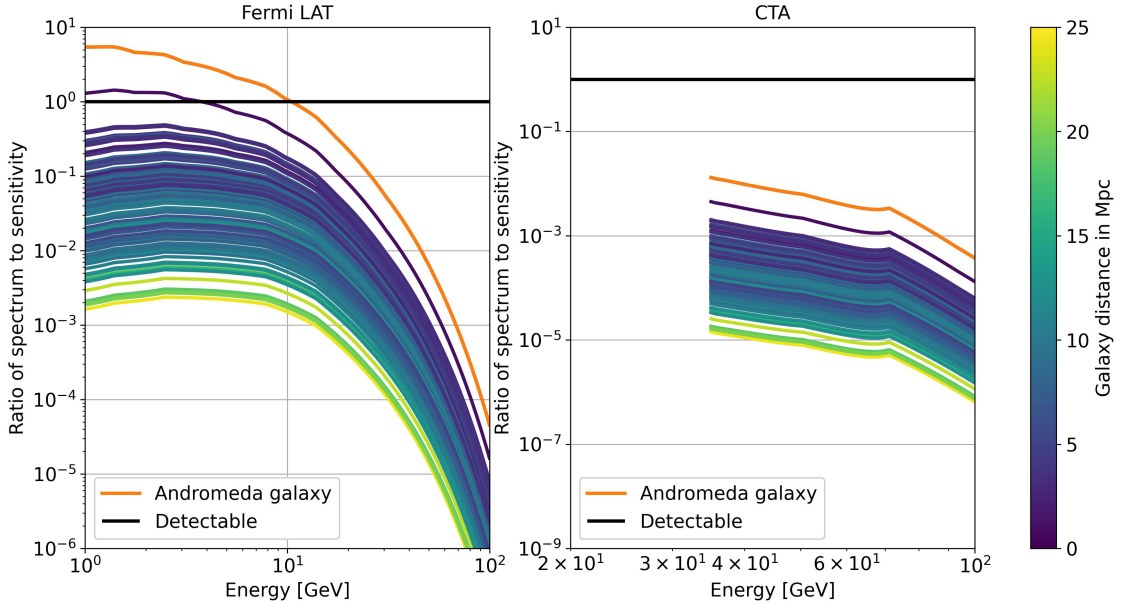

Figure 6.3: Resulting fraction of the expected spectrum, which is represented by Equation 6.3 and scaled by Equation 6.4 or Equation 6.5 for each galaxy, to the sensitivity of extended sources, which is calculated by multiplying the sensitivity for point sources with κ (see Equation 6.1), for the final galaxy selection (see section 3.2) for Fermi-LAT (right side) and CTA (left side). The horizontal at 1 is marked, which indicates a possible detection. The colour bar indicates the distance of the galaxy.

Parameter	**MESSIER031**	**MESSIER033**	**IC0342**	**NGC0253**	**NGC0055**	**NGC4945**	**MESSIER101**
Longitude [°]	121.1749	133.6098	138.1732	97.4350	332.667	305.2681	102.0381
Latitude [°]	-21.5729	-31.3306	10.5800	-87.9695	-75.739	13.3371	59.7696
Diameter [kpc]	43.45	17.38	34.25	40.83	21.71	34.38	65.2
Distance [Mpc]	0.77	0.85	3.28	3.94	2.13	3.80	7.38
Log. Mass [$M_\odot$]	$10^{11.5}$	$10^{10.29}$	$10^{11.15}$	$10^{11.24}$	$10^{10.15}$	$10^{11.5}$	$10^{11.35}$
Abs. Magnitude	-21.4	-18.8	-20.7	-21.3	-18.4	-20.5	-21.1
Inner Galaxy [kpc]	11	4.4	8.68	10.34	5.5	8.7	16.5
Spherical Halo [kpc]	240	96	189.18	225.52	21.71	189.9	360.14
Outer Halo [kpc]	400	160	315.3	375.88	199.86	316.5	600.24
Luminosity [10^{38}erg/s]	17.0	14.0	0.937	0.649	2.22	0.698	1.85

Table 6.1: The six most promising NEARGALCAT candidates (see Figure 6.3) and the Andromeda Galaxy as reference (Messier 31) with their corresponding most important NEARGALCAT data and prediction for their Halo features and luminosity.

For the modelling the SH radius is needed. The SH radius for M31 is 8.86° and can be scaled with the distance by k_{distance} and for the galaxy size with k_{size}. In Figure 6.4 a heatmap for different distances and radii is shown. Also indicated are the contour lines for the PSF of Fermi-LAT at 1 GeV (white dotted line labelled 0.80°) and for 10 GeV (white dotted line labelled 0.15°). The candidates from Table 6.1 also shown in Figure 6.4. Galaxies, which are positioned in the area of the PSF, are indistinguishable to a point source and therefore the spatial feature of the SH can not be examined. Moreover, it will be shown that modelling of these candidates is not achievable.

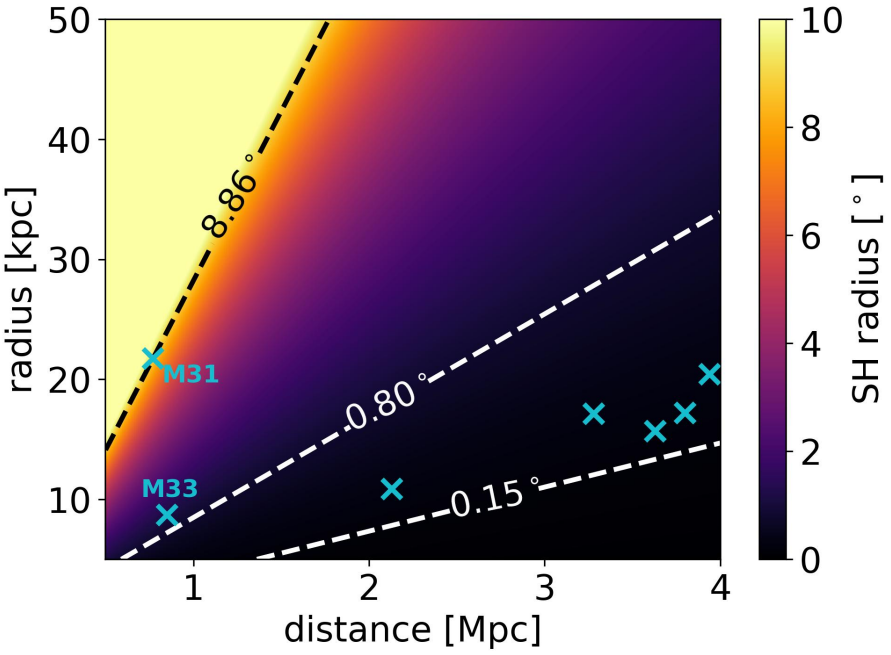

Figure 6.4: Predicted SH size for different distances and galaxy radii. The two white dotted lines, labelled 0.80° and 0.15°, mark the size of the PSF at and 1 GeV and 10 GeV. The cyan crosses represent the galaxies from table Table 6.1. The galaxies positioned in the area of the PSF are not labelled for better clarity.

6.2 Nearby Spiral Galaxies Candidates

Potential candidates from Table 6.1 are investigated, and the same analysis chain is used as shown in last chapter.

6.2.1 Triangulum Galaxy (M33)

Firstly, the models in the ROI are fitted in `Fermipy`. The resulting significance map is shown in Figure 6.5a with the corresponding significance distribution in Figure 6.5b. The resulting mean is -0.11 ± 0.01 and the standard deviation 1.31 ± 0.01. Both are in an acceptable range, and one can start with further analysis in `Gammapy`.

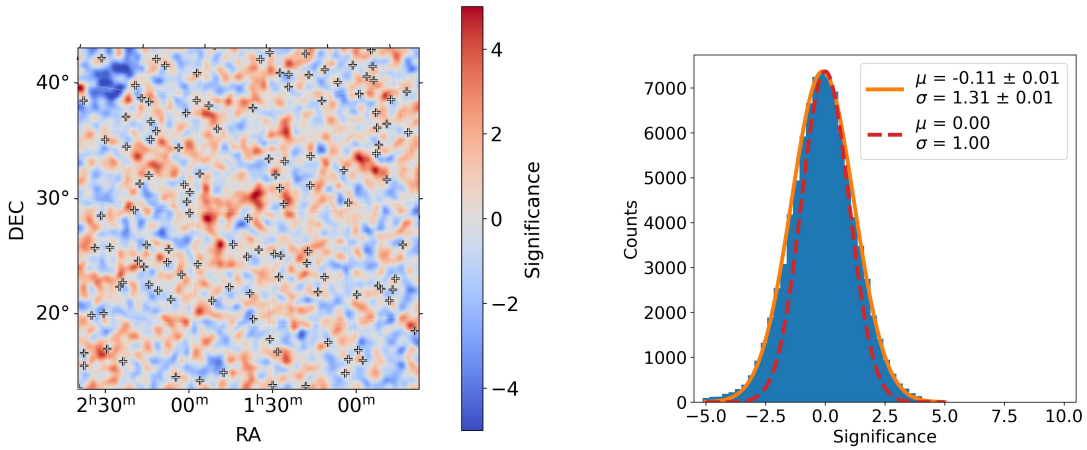

(a) Significance map (correlation radius of 0.3°).

(b) Significance distribution.

Figure 6.5: **(a)**: LiMa Significance map of the ROI after fitting all models in `Fermipy` with a correlation radius of 0.3°. The plus signs represent a source from the catalogue. **(b)**: Distribution of the significance from the significance map. Also shown is the normal distribution (see Equation 5.9) fit to the data (orange line) with a normal distributed with $\sigma = 1$ and $\mu = 0$ for comparison (red dotted line).

In Figure 6.6 the counts map of the ROI is shown. As already discussed, an edge cut is applied (orange dotted line in Figure 6.6). The resulting ROI is approximately $20° \times 20°$. The exact values are not needed, because the area is much bigger than the examined SH (green circle in Figure 6.6). Also shown is the source galaxy (Triangulum Galaxy or M33) as cyan cross in Figure 6.6. M33 is not listed in the provided source catalogue and is therefore not modelled.

After loading the data into `Gammapy` and fitting all models, the two background models and the template background models consisting of all other remaining sources in the ROI, except the SH to the ROI, the significance map (see Figure 6.7a), spectral residual points (see Figure 6.7b) and normal distribution fit to the significance distribution (see Table 6.2) are calculated. The ROI is flattened, and the results are an improvement to the `Fermipy` results. This is used as the null hypothesis to compare the SH model to.

As in the case for M31, the six different models are modelled. In Table 6.3 are the resulting significance shown. The EXP-model and LOG-model have very similar results, but the LOG-model is still more significance by a small margin of 0.01 for

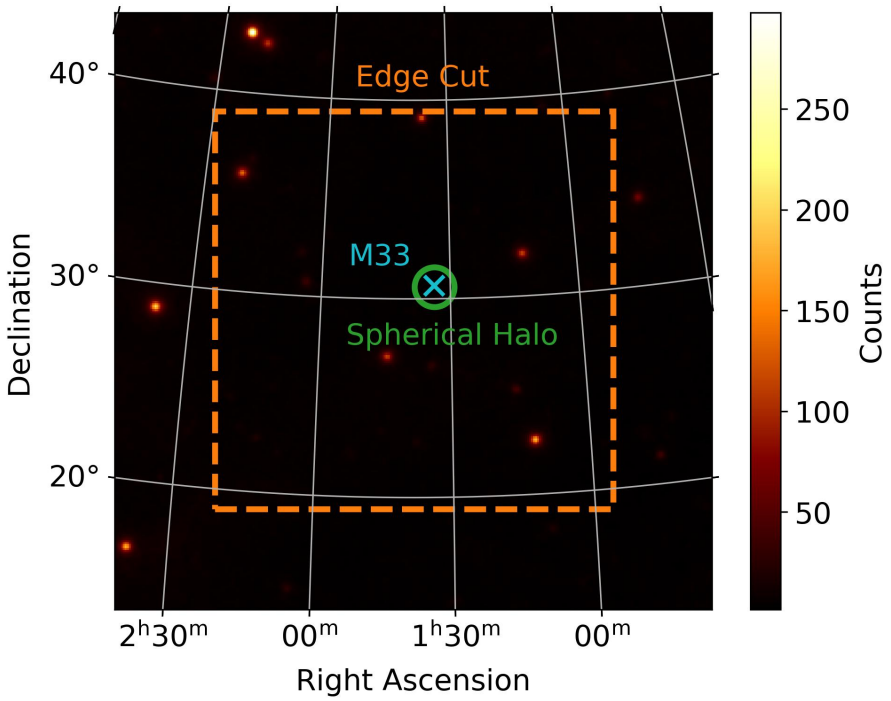

Figure 6.6: Counts Map from `Fermipy` with a $30° \times 30°$ ROI with the source galaxy shown. For `Gammapy` only a $\approx 20° \times 20°$ is needed. Therefore, a spatial cut is applied (orange line), which is similar to the $20° \times 20°$. The source galaxy (M33) is shown in cyan with the SH in green.

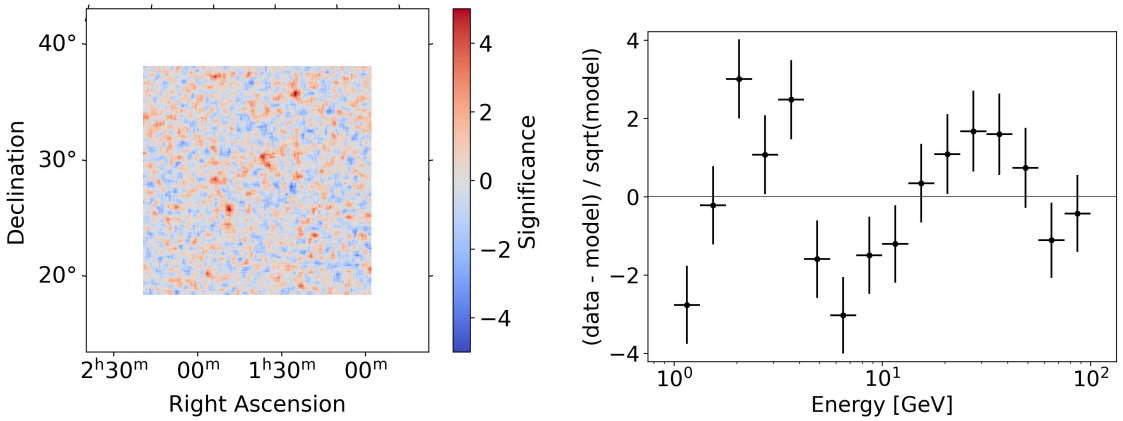

(a) Significance map (correlation radius of 0.3°). **(b)** Spectral residual points.

Figure 6.7: **(a)**: LiMa Significance map of the ROI with correlation radius of 0.3°. **(b)**: Spectral residual points for the significance map.

both cases. The spectra are compared to the spectrum from Karwin et al. 2019, which is scaled by 0.13 resulting from applying Equation 6.4 and Equation 6.5. In Figure 6.8 a comparison of all models for their best-fit result is show. The spectra are in the same order of magnitude as the scaled spectrum from Karwin et al. 2019. Still, the 1σ error range is visibly broader, which is most likely a result of the lower gamma-ray count. In the following the best-fit model, LOG-model with fixed radius, is discussed in greater detail.

In Table 6.4 are the most important model parameters with their initial value

Energy bin	μ	σ
1 GeV - 2.37 GeV	-0.045 ± 0.005	1.025 ± 0.005
2.37 GeV - 4.22 GeV	0.012 ± 0.005	1.018 ± 0.005
4.22 GeV - 10 GeV	-0.170 ± 0.007	1.047 ± 0.007
10 GeV - 100 GeV	-0.095 ± 0.030	1.030 ± 0.030

Table 6.2: Distribution of the LiMa significance in four different energy, chosen for better statistics (see Figure 5.3b). The expected distribution is a normal distribution with $\mu = 0$ and $\sigma = 1$.

Spectral Model	Significance σ for radius	
	$r = 1.0°$ $(k = 3)$	**free** $(k = 4)$
PWL-model	4.26	4.00
EXP-model	4.43	4.16
LOG-model	4.44	4.17

Table 6.3: Resulting significances (see section 5.1 for more details) for different spectral models with a disk spatial model either with a fixed radius to 1.0° or a free radius. The models examined are power law model (PWL-model), exponential cutoff power law model (EXP-model), and log parabola model (LOG-model).

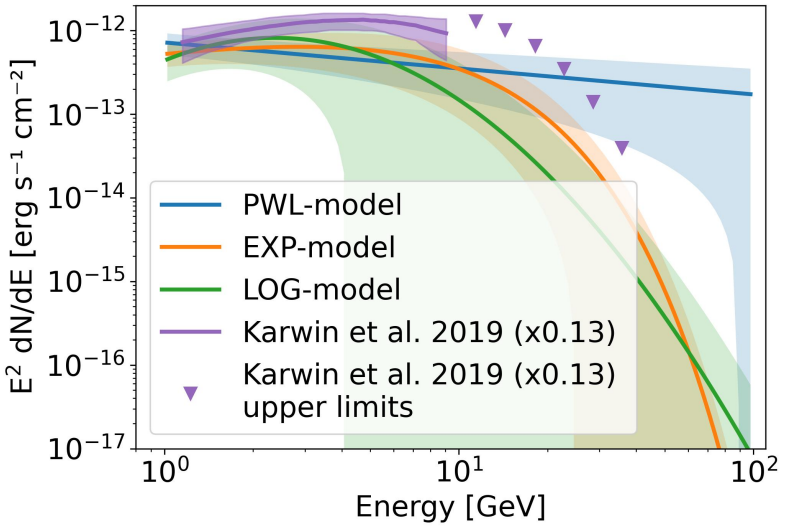

Figure 6.8: Spectral shape comparison of the different models to the best-fit EXP-model from Karwin et al. 2019, which is scaled (×0.13) by distance and size (see Equation 6.4 and Equation 6.5). The shaded regions give the 1σ error and downward pointing triangles give upper limits.

and the resulting values after a fit with fixed or free radius are shown. The same spectral model parameters are chosen as in the case of M31. The amplitude ϕ_0 wasn't adapted, even though one expects a smaller flux, because the fit would still converge to the same values. The radius was set to $r_0 = 1.0°$, which is in the same order as the expected radius $r_{\text{pred.}} = 1.16°$ (see Figure 6.4). The spectral model comparison will be discussed later in this section.

In Figure 6.9a is the significance map and in Figure 6.9b spectral residual points shown. The fit results for the significance distribution are shown in Table 6.5. No significant different can be seen by comparing the significance and the distribution

Parameter	Initial Value	Fit (fixed radius)	Fit (free radius)
Log Parabola Spectral Model			
ϕ_0 [MeV cm^{-2} s^{-1}]	6.7032×10^{-12}	$(0.26 \pm 0.10) \times 10^{-12}$	$(0.26 \pm 0.10) \times 10^{-12}$
E_0 [GeV]	1	-	-
α	2.3	1.0 ± 0.4	1.0 ± 0.4
β	0.5	0.50 ± 0.15	0.50 ± 0.15
Disk Spatial Model			
longitude (icrs)	23°27′43″	-	-
latitude (icrs)	30°39′37″	-	-
radius [°]	1.0	1.0	1.00 ± 0.05
E_0 [GeV]	1	-	-
Galactic Background			
isotropic norm	0.9216	1.024 ± 0.020	1.0241 ± 0.0200
isotropic tilt [10^{-2}]	-1.112	7.0 ± 1.3	7.0 ± 2.0
Isotropic Background			
galactic norm	1.175	1.00 ± 0.01	1.00 ± 0.09
galactic tilt [10^{-2}]	0	2.4 ± 1.7	2.4 ± 1.7
E_0 [TeV]	1	-	-

Table 6.4: Model parameter values for the spectral LOG-model, the disk spatial model and the two background models. Given are the initial values, the values after the fit with a fixed radius (1.0°) and after the fit with the radius as a free parameter.

before and after the fit with fixed radius. By comparing the spectral residual points (see Figure 6.9b), an improvement can be seen over the whole energy range.

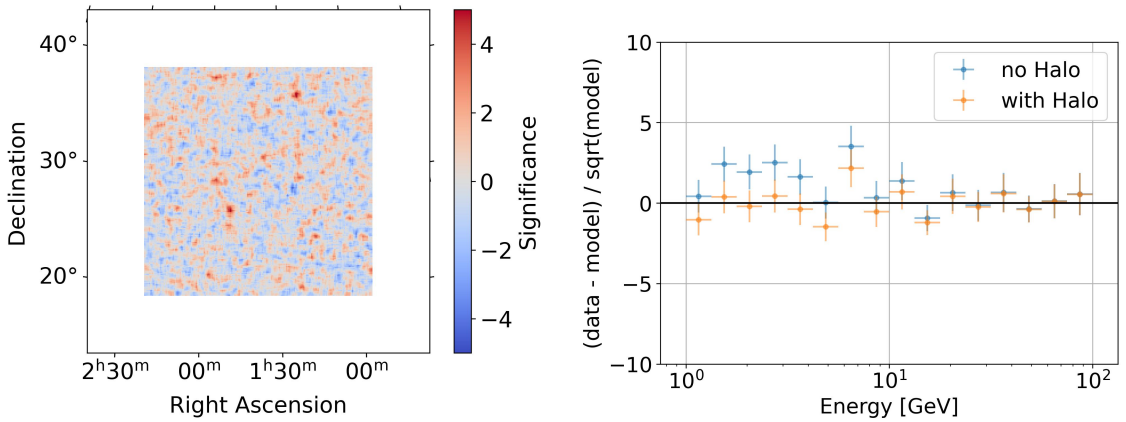

(a) Significance map (correlation radius of 0.3°). **(b)** Spectral residual points.

Figure 6.9: **(a)**: LiMa Significance map of the ROI with correlation radius of 0.3°. **(b)**: Spectral residual points inside the SH ($r = 1.0°$) for the significance map before and after the fit.

Another thing to investigated, is the predicted count rate. In Figure 6.10a the predicted count map for the SH of M33 is shown. Because the source galaxy is not shown, one excepts the count rate to be partly from the source galaxies. In the case of M31, a ratio of 1:10 was derived. This results in 209 counts from the SH and 21 counts from M33.

In Figure 6.10b the spectra for the isotropic background and the LOG-model are

Energy bin	μ	σ
1 GeV - 2.37 GeV	-0.042 ± 0.005	1.023 ± 0.005
2.37 GeV - 4.22 GeV	0.011 ± 0.005	1.018 ± 0.005
4.22 GeV - 10 GeV	-0.167 ± 0.007	1.047 ± 0.007
10 GeV - 100 GeV	-0.093 ± 0.030	1.031 ± 0.030

Table 6.5: Distribution of the LiMa significance in four different energy for the best-fit LOG-model. The expected distribution is a normal distribution with $\mu = 0$ and $\sigma = 1$.

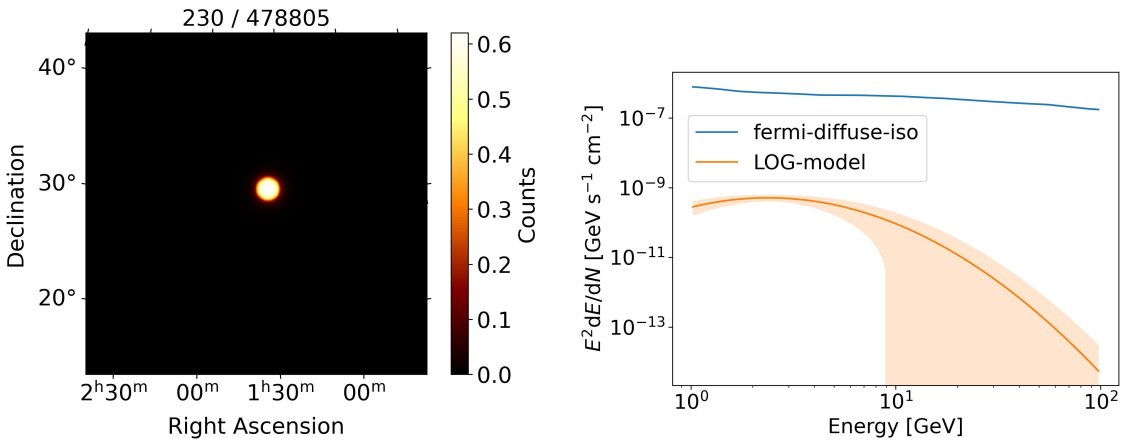

(a) Predicted counts from the SH of M33.

(b) Gamma-ray spectra for all models.

Figure 6.10: **(a)**: Predicted counts for the SH of M33 after the first fit with the LOG-model. The first number resembles the predicted counts from the source the second the total predicted gamma-ray count. **(b)**: Gamma-ray spectra for the isotropic background model and the SH model (LOG-model) for the best-fit LOG-model.

shown. The best-fit model is in an order of 10^{-3} smaller than the background.

Lastly, the flux points are calculated and compared to the spectrum from Karwin et al. 2019 scaled with the factors defined in Equation 6.5 and Equation 6.4 (see Figure 6.11). Last section in the case for the Andromeda Galaxy a dip has been seen, this feature is not visible. Model and flux points in the same order of magnitude as predicted.

Cosmic ray halo model fit results in unreasonable error bands, which spans from $(0 - 1 \times 10^{-8})\,\mathrm{GeV\,s^{-1}\,cm^{-2}}$ and is therefore not pursued further.

Lastly, the second source origin is examined. The DM profile is adapted by scaling the different parameters of the profiles with the size and distance of the galaxy (see Equation 6.4 and Equation 6.5). The results are shown in Figure 6.12, where a qualitative comparison to the previously discussed best-fit model and its corresponding flux points is performed. The shape is promising, but a more detailed DM analysis has to be performed.

6.2.2 IC 0342

The same analysis chain was used for IC 0342 as for both previous galaxies. The LOG-model with a fixed radius (set to 1°), which was the best-fit model in the previous cases, predicts no counts (see Figure 6.13). For this reason further, analysis is not pursued. As expected, modelling of galaxies with further distance than M33,

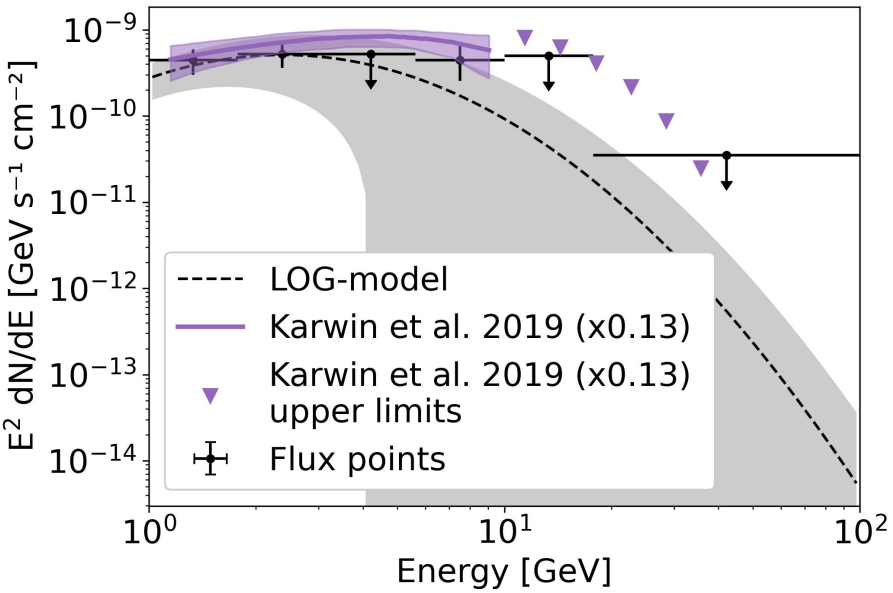

Figure 6.11: Best-fit LOG-model with the corresponding flux points. The flux points are calculated for six energy bins, which where chosen for better statistics. The spectrum plus flux points are compared to the spectrum from Karwin et al. 2019, which is scaled ($\times$0.13) by distance and size (see Equation 6.4 and Equation 6.5). Also, a visible dip in significance for the flux points is indicated (red arrow).

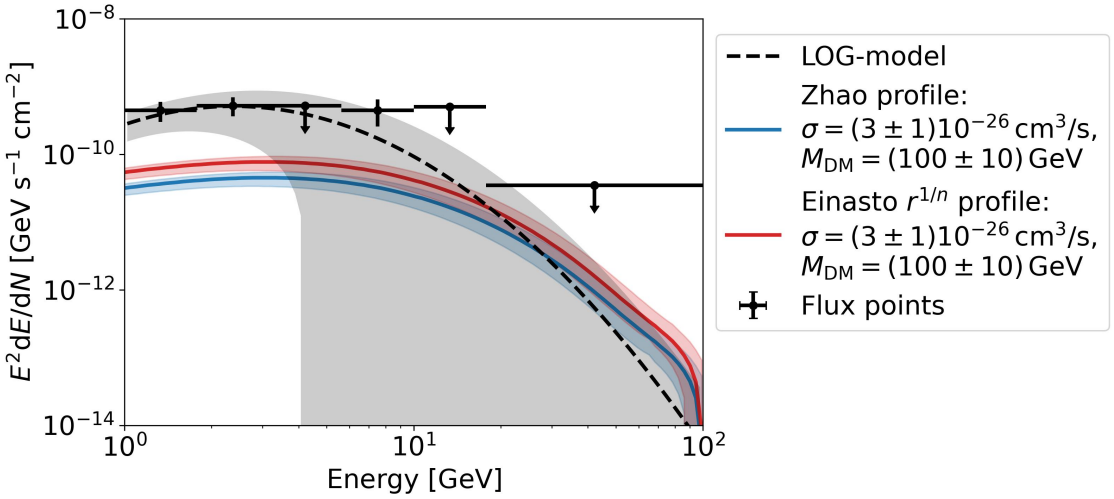

Figure 6.12: Spectral shape comparison of the two profiles (defined in section 4.6) to the best-fit LOG-model and the corresponding flux points. The error band is estimated by doing the simulation with the upper or lower errors of the annihilation cross-section σ and DM mass M_{DM}.

yields no useful results.

6.2.3 Comparison to the Andromeda Galaxy

In the end the results from the analysis of the M31-like galaxies, only M33 in this case, are compared to the Andromeda Galaxy. In Figure 6.14 the LOG-models and

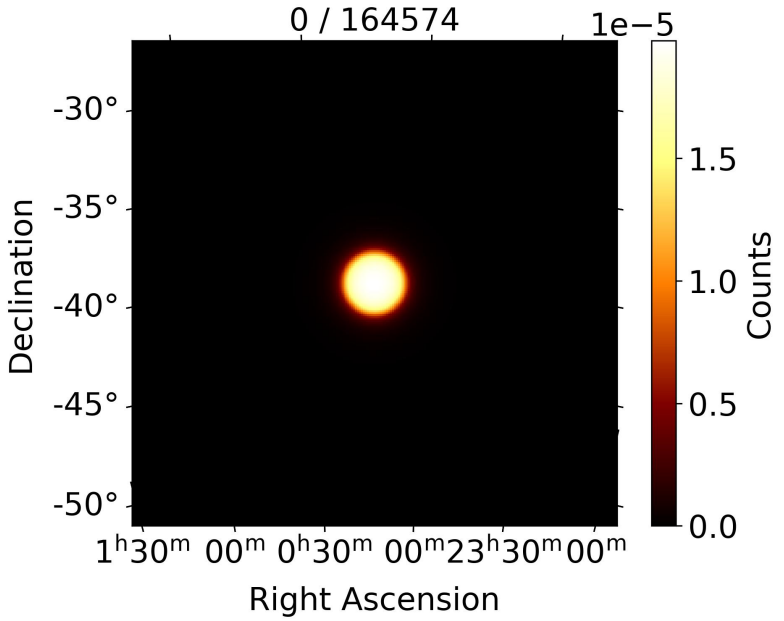

Figure 6.13: Predicted counts for the SH of IC 0342 after the first fit with the LOG-model. The first number resembles the predicted counts from the source the second the total predicted gamma-ray count.

flux points of M33 and M31 are shown. Both spectra follow a similar shape in the lower energy range (below 5 GeV). At higher energies, the uncertainties are too high to make some confident statements.

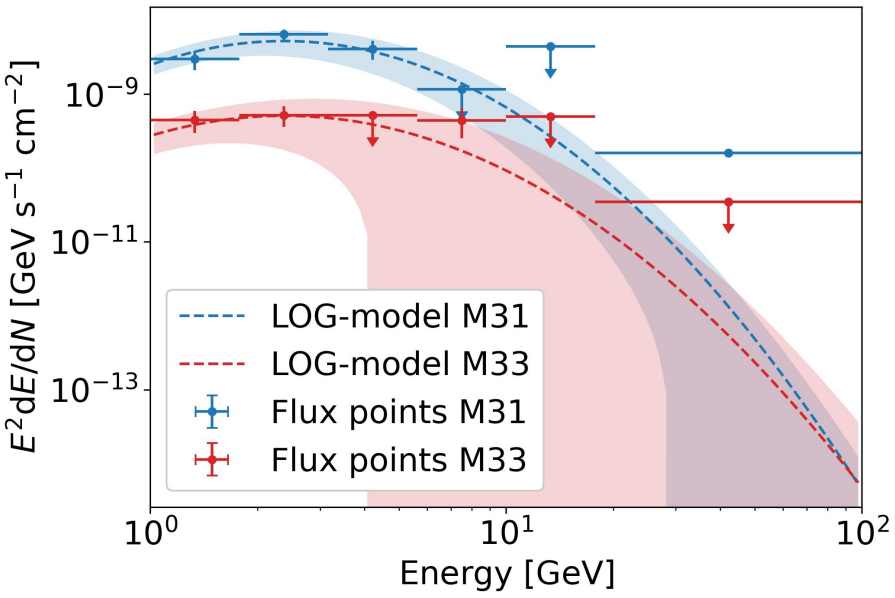

Figure 6.14: Spectral LOG-model and flux point comparison for M31 and M33.

Chapter 7

Summary and Outlook

In this work I have examined the SH of the Andromeda Galaxy, modelled it with different spectral models and compared it to two potential models for the origin of the gamma-ray emission, DM and CRs. The data analysed in the work is detected by Fermi-LAT. Afterwards, potential M31-like galaxy candidates are selected and checked whether the same SH phenomenon exists.

Firstly, the CR scenario is simulated following Recchia et al. 2021, where they describe the hadronic or leptonic source models with a power law with an exponential cutoff. It was not possible to reproduce the results and own best-fit sources were determined, by fitting the source spectra to the SH spectral model used in Karwin et al. 2019, which uses Fermi-LAT data. The resulting values for the power p and energy cutoff o changes in the hadronic case from $p = 2$ to $p = 0.10 \pm 0.17$ and $o = 110\,\mathrm{GeV}$ to $o = (18.3 \pm 1.8)\,\mathrm{GeV}$ and in leptonic case from $p = 2$ to $p = 0.50 \pm 0.06$ and $o = 500\,\mathrm{GeV}$ to $o = (250 \pm 11)\,\mathrm{GeV}$. Afterwards, DM models were adapted from Karwin et al. 2021, where they describe the gamma-ray emission from the area surrounding M31 with NFW-profile or an Einasto-profile ($\alpha = 0.17$). These simulated are used for further analysis.

The next step is to develop the analysis chain that is used to analyse Fermi-LAT data of the region around M31. Data from the Fermi-LAT detector is processed with `Fermipy` and first source optimizations are carried out. Thereafter, the data is converted into a GADF, which is a processable format for `Gammapy`. `Gammapy` is used to model the SH with three distinct spectral models, a power law, a power law with exponential cutoff and a log parabola. The morphology of the SH is modelled as a uniform disk with a radius r and centred around the source galaxy. The log parabola spectral model with a spatial disk model ($r = 8.86°$) turns out to describe the SH the best with a significance of $\sigma = 5.61$, which was not considered in the analyses carried out in Karwin et al. 2019. On the basis of the best-fit model, several steps of the analysis chain are shown. Lastly, in the analysis chain, the flux points are calculated. Then, the model plus the flux points are compared to the two previously mentioned models for the origin of the gamma-ray emission.

In the next part, potential M31-like galaxy candidates are determined from the NEARGALCAT, by applying three selection cuts on the galaxy parameters, diameter, mass and absolute magnitude. The selection cuts are chosen so that only M31-like galaxy remain. By making rough sensitivity estimation for Fermi-LAT and CTA, the candidates are sorted by likelihood of measurement. CTA leads to no candidates, and therefore only the candidates from the Fermi-LAT sensitivity study are

considered. The six most promising candidates are considered and their SH sizes are predicted. The first candidate, the Triangulum Galaxy, is analysed with the same chain as before, and results in a LOG-model with $\sigma = 4.44$. The CR source model was unable to describe the SH, whereas the DM could possibly explain it. Also, the best-fit model resulting from the M31 analysis is compared to the one obtained for M33. In the end, the galaxy IC 342 is analysed with the chain. The predicted gamma-rays from the best-fit model are below 1 and therefore further analysis is no longer pursued.

In the case of the M31, the flux points match the spectral model at lower energies ($< 20\,\mathrm{GeV}$) but at higher energies they deviate from the model. This suggests, that a PWL-model would describe the flux points better. The CR hadronic source model supports that idea, because it also predicts a PWL-model and the resulting spectrum follows the source spectrum. A qualitative comparison with DM model and the LOG-model was performed. The DM model shape looks promising, but a more detailed DM analysis has to be done. Another feature that can be recognized is a dip in the medium energy range ($\sim 10\,\mathrm{GeV}$) of the source flux. This has been seen in other spectra resulting from analysis of Fermi-LAT data [51]. It could be either a result of some internal systematics in `Fermipy` or could be a hint for a two component spectrum. A detailed study about this dip is out of scope for this work. Both gamma-ray origin models discussed aren't able to explain a two component spectrum. The chance to detect the SH structures at other SGs is currently not possible, but a detector with a ten times lower sensitivity would resolve in potential candidate in the double-digit range. The predicted size is currently in the order of a point-source, and therefore analysis of the spatial structure is not feasible. However, this was the first analysis of the SH of M33 with data taken by Fermi. Once again, the LOG-model with a proved to be the most significant, albeit at a very small margin to the EXP-model (0.01). Fitting the CR model to the data was not possible, because the errors were orders of magnitude higher than the expected flux. The DM models looks again promising, but a more detailed DM analysis has to be carried out. However, the models display considerable uncertainties and no final conclusions should be drawn.

For the future, a more detailed analysis for the gamma-ray origin could be done. In the case of DM, the simulations were done with commonly used parameters (σ and M_{DM}) in the literature. The CR scenario used a simple source spectrum with an EXP-model, which could also be modelled in more detail. For the data analysis of the Fermi data, a systematic study could be carried, because for hugely extended sources with low flux one expects high systematics.

Bibliography

[1] C. M. Karwin, S. Murgia, S. Campbell, and I. V. Moskalenko. "Fermi-LAT Observations of γ-Ray Emission toward the Outer Halo of M31". In: *Astrophysical Journal* 880.2, 95 (Aug. 2019), p. 95. DOI: 10.3847/1538-4357/ab2880. arXiv: 1812.02958 [astro-ph.HE].

[2] T. J. Cox and Abraham Loeb. "The collision between the Milky Way and Andromeda". In: *MNRAS* 386.1 (May 2008), pp. 461–474. DOI: 10.1111/j.1365-2966.2008.13048.x. arXiv: 0705.1170 [astro-ph].

[3] NASA. *The Fermi Science Support Center (FSSC)*. https://fermi.gsfc.nasa.gov/ssc/. [Online; accessed 20-September-2023]. 2023.

[4] Particle Data Group, P A Zyla, R M Barnett, J Beringer, et al. "Review of Particle Physics". In: *Progress of Theoretical and Experimental Physics* 2020.8 (Aug. 2020), p. 083C01. ISSN: 2050-3911. DOI: 10.1093/ptep/ptaa104. eprint: https://academic.oup.com/ptep/article-pdf/2020/8/083C01/34673722/ptaa104.pdf. URL: https://doi.org/10.1093/ptep/ptaa104.

[5] A. M. Baldini, Y. Bao, E. Baracchini, C. Bemporad, et al. "Measurement of the radiative decay of polarized muons in the MEG experiment". In: *European Physical Journal C* 76, 108 (Mar. 2016), p. 108. DOI: 10.1140/epjc/s10052-016-3947-6.

[6] S. Recchia, S. Gabici, FA. Aharonian, and V. Niro. "Giant Cosmic-Ray Halos around M31 and the Milky Way". In: *The Astrophysical Journal* 914.2 (2021), p. 135.

[7] G. R. Blumenthal and R. J. Gould. "Bremsstrahlung, Synchrotron Radiation, and Compton Scattering of High-Energy Electrons Traversing Dilute Gases". In: *Reviews of Modern Physics* 42.2 (Jan. 1970), pp. 237–271. DOI: 10.1103/RevModPhys.42.237.

[8] Y. W. Wong. *Diffuse γ-Ray Emission from the Galactic Centre with H.E.S.S.* https://ecap.nat.fau.de/wp-content/uploads/2023/03/2023_PhD_YuWunWong.pdf. [PhD thesis, Friedrich-Alexander-Universität Erlangen-Nürnberg]. 2023.

[9] M. Ackermann, M. Ajello, W. B. Atwood, L. Baldini, et al. "Fermi LAT observations of cosmic-ray electrons from 7 GeV to 1 TeV". In: *Phys. Rev. D* 82 (9 2010), p. 092004. DOI: 10.1103/PhysRevD.82.092004. URL: https://link.aps.org/doi/10.1103/PhysRevD.82.092004.

[10] Standford | The Fermi Large Area Telescope. *The Fermi LAT instrument*. https://www-glast.stanford.edu/instrument.html. [Online; accessed 1-September-2023]. 2023.

[11] Nasa. *Spacecraft Icons*. https://science.nasa.gov/get-involved/toolkits/spacecraft-icons. [Online; accessed 7-September-2023]. 2023.

[12] Fermi LAT Performance. *Fermi LAT Performance*. https://www.slac.stanford.edu/exp/glast/groups/canda/lat_Performance.htm. [Online; accessed 3-September-2023]. 2023.

[13] M. Ackermann, M. Ajello, A. Allafort, K. Asano, et al. "Determination of the Point-spread Function for the Fermi Large Area Telescope from On-orbit Data and Limits on Pair Halos of Active Galactic Nuclei". In: *Astrophysical Journal* 765.1, 54 (Mar. 2013), p. 54. DOI: 10.1088/0004-637X/765/1/54. arXiv: 1309.5416 [astro-ph.HE].

[14] W. Hofmann and R. Zanin. *The Cherenkov Telescope Array*. To appear in "Handbook of X-ray and Gamma-ray Astrophysics" by Springer (Eds. C. Bambi and A. Santangelo). 2023. arXiv: 2305.12888 [astro-ph.IM].

[15] CTA. *CTAO's site in the southern hemisphere*. https://www.cta-observatory.org/about/locations/ctao-south/. [Online; accessed 1-September-2023]. 2023.

[16] R. M. Wagner. "Measurement of very high energy gamma-ray emission from four blazars using the MAGIC telescope and a comparative blazar study". PhD thesis. Max-Planck-Institute for Physics, Munich, Jan. 2006.

[17] CTA. *CTAO's expected "Alpha Configuration" performance*. https://www.cta-observatory.org/science/ctao-performance. [Online; accessed 17-October-2023]. 2023.

[18] B. W. Carroll and D. A. Ostlie. *An introduction to modern astrophysics, Second Edition*. 2017.

[19] Cosmogoblin. *Hubble Tuning Fork diagram*. https://commons.wikimedia.org/wiki/File:Hubble_Tuning_Fork_diagram.svg. [Online; accessed 17-October-2023]. 2023.

[20] I. D. Karachentsev, D. I. Makarov, and E. I. Kaisina. "Updated Nearby Galaxy Catalog". In: *Astronomical Journal* 145.4, 101 (Apr. 2013), p. 101. DOI: 10.1088/0004-6256/145/4/101. arXiv: 1303.5328 [astro-ph.CO].

[21] E. Holmberg. "A photographic photometry of extragalactic nebulae." In: *Meddelanden fran Lunds Astronomiska Observatorium Serie II* 136 (Jan. 1958), p. 1.

[22] M. S. Longair. *High Energy Astrophysics*. 2011.

[23] C. M. Karwin, S. Murgia, I. V. Moskalenko, S. P. Fillingham, et al. "Dark matter interpretation of the Fermi-LAT observations toward the outer halo of M31". In: *Phys. Rev. D* 103.2, 023027 (Jan. 2021), p. 023027. DOI: 10.1103/PhysRevD.103.023027. arXiv: 2010.08563 [astro-ph.HE].

[24] J. Hahn, C. Romoli, and M. Breuhaus. *GAMERA: Source modeling in gamma astronomy*. Astrophysics Source Code Library, record ascl:2203.007. Mar. 2022. ascl: 2203.007.

[25] Dembinski H. and P. Ongmongkolkul et al. "scikit-hep/iminuit". In: (2020). DOI: 10.5281/zenodo.3949207. URL: https://doi.org/10.5281/zenodo.3949207.

[26] J. L. Feng. "Dark Matter Candidates from Particle Physics and Methods of Detection". In: *ARA&A* 48 (Sept. 2010), pp. 495–545. DOI: 10.1146/annurev-astro-082708-101659. arXiv: 1003.0904 [astro-ph.CO].

[27] K. Garrett and G. Dūda. "Dark Matter: A Primer". In: *Advances in Astronomy* 2011, 968283 (Jan. 2011), p. 968283. DOI: 10.1155/2011/968283. arXiv: 1006.2483 [hep-ph].

[28] V. C. Rubin. "Dark matter in spiral galaxies". In: *Scientific American* 248 (June 1983), pp. 96–106. DOI: 10.1038/scientificamerican0683-96.

[29] T. S. van Albada, J. N. Bahcall, K. Begeman, and R. Sancisi. "Distribution of dark matter in the spiral galaxy NGC 3198." In: *Astrophysical Journal* 295 (Aug. 1985), pp. 305–313. DOI: 10.1086/163375.

[30] NASA: Hubblesite. *Gravitational Lensing*. https://hubblesite.org/contents/articles/gravitational-lensing. [Online; accessed 17-October-2023]. 2023.

[31] J. Dunkley, E. Komatsu, M. R. Nolta, D. N. Spergel, et al. "Five-Year Wilkinson Microwave Anisotropy Probe Observations: Likelihoods and Parameters from the WMAP Data". In: *Astrophysical Journal, Supplement* 180.2 (Feb. 2009), pp. 306–329. DOI: 10.1088/0067-0049/180/2/306. arXiv: 0803.0586 [astro-ph].

[32] NASA: Chandra X ray observatory. *Bullet Cluster*. https://apod.nasa.gov/apod/ap170115.html. [Online; accessed 17-October-2023]. 2023.

[33] E. Aprile, J. Aalbers, F. Agostini, M. Alfonsi, et al. "The XENON1T Dark Matter Experiment". In: *The European Physical Journal C* 77.12 (Dec. 18, 2017), p. 881. ISSN: 1434-6052. DOI: 10.1140/epjc/s10052-017-5326-3. URL: https://doi.org/10.1140/epjc/s10052-017-5326-3.

[34] J. Billard, M. Boulay, S. Cebrián, L. Covi, et al. "Direct detection of dark matter-APPEC committee report". In: *Reports on Progress in Physics* 85.5, 056201 (May 2022), p. 056201. DOI: 10.1088/1361-6633/ac5754. arXiv: 2104.07634 [hep-ex].

[35] MAGIC Collaboration. "Limits to dark matter annihilation cross-section from a combined analysis of MAGIC and Fermi-LAT observations of dwarf satellite galaxies". In: *J. Cosmology Astropart. Phys.* 2016.2 (Feb. 2016), pp. 039–039. DOI: 10.1088/1475-7516/2016/02/039. arXiv: 1601.06590 [astro-ph.HE].

[36] A. Charbonnier, C. Combet, and D. Maurin. "CLUMPY: A code for γ-ray signals from dark matter structures". In: *Computer Physics Communications* 183.3 (Mar. 2012), pp. 656–668. DOI: 10.1016/j.cpc.2011.10.017. arXiv: 1201.4728 [astro-ph.HE].

[37] M. Hütten, C. Combet, and D. Maurin. "CLUMPY v3: γ-ray and ν signals from dark matter at all scales". In: *Computer Physics Communications* 235 (Feb. 2019), pp. 336–345. DOI: 10.1016/j.cpc.2018.10.001. arXiv: 1806.08639 [astro-ph.CO].

[38] A. E. Egorov. "Updated constraints on WIMP dark matter annihilation by radio observations of M31". In: *Phys. Rev. D* 106.2, 023023 (July 2022), p. 023023. DOI: 10.1103/PhysRevD.106.023023. arXiv: 2205.01033 [astro-ph.CO].

[39] Juan A. Aguilar S., R. Abbasi, M. Ackermann, J. Adams, et al. "Search for Dark Matter annihilation in the center of the Earth with IceCube". In: *Proceedings of 38th International Cosmic Ray Conference — PoS(ICRC2023)*. Vol. 444. 2023, p. 1393. DOI: 10.22323/1.444.1393.

[40] G. A. Gómez-Vargas, M. A. Sánchez-Conde, J. Huh, M. Peiró, et al. "Constraints on WIMP annihilation for contracted dark matter in the inner Galaxy with the Fermi-LAT". In: *J. Cosmology Astropart. Phys.* 2013.10, 029 (Oct. 2013), p. 029. DOI: 10.1088/1475-7516/2013/10/029. arXiv: 1308.3515 [astro-ph.HE].

[41] J. F. Navarro, C. S. Frenk, and S. D. M. White. "The Structure of Cold Dark Matter Halos". In: *ApJ* 462 (May 1996), p. 563. DOI: 10.1086/177173. arXiv: astro-ph/9508025 [astro-ph].

[42] M. Cirelli, G. Corcella, A. Hektor, G. Hütsi, et al. "PPPC 4 DM ID: a poor particle physicist cookbook for dark matter indirect detection". In: *J. Cosmology Astropart. Phys.* 2011.3, 051 (Mar. 2011), p. 051. DOI: 10.1088/1475-7516/2011/03/051. arXiv: 1012.4515 [hep-ph].

[43] C. Weniger. *Advanced Statistical Methods - Lecture 3*. https://staff.fnwi.uva.nl/c.weniger/data/stats1/slides3.pdf. [Online; accessed 20-October-2023]. 2022.

[44] S. S. Wilks. "The Large-Sample Distribution of the Likelihood Ratio for Testing Composite Hypotheses". In: *The Annals of Mathematical Statistics* 9.1 (1938), pp. 60 –62. DOI: 10.1214/aoms/1177732360. URL: https://doi.org/10.1214/aoms/1177732360.

[45] The Fermi-LAT Collaboration. *Galactic Interstellar Emission Model for the 4FGL Catalog Analysis*. https://fermi.gsfc.nasa.gov/ssc/data/analysis/software/aux/4fgl/Galactic_Diffuse_Emission_Model_for_the_4FGL_Catalog_Analysis.pdf. [Online; accessed 23-October-2023]. 2019.

[46] M. Wood, R. Caputo, E. Charles, M. Di Mauro, et al. "Fermipy: An open-source Python package for analysis of Fermi-LAT Data". In: *35th International Cosmic Ray Conference (ICRC2017)*. Vol. 301. International Cosmic Ray Conference. July 2017, 824, p. 824. DOI: 10.22323/1.301.0824. arXiv: 1707.09551 [astro-ph.IM].

[47] J. Ballet, P. Bruel, T. H. Burnett, B. Lott, and The Fermi-LAT collaboration. "Fermi Large Area Telescope Fourth Source Catalog Data Release 4 (4FGL-DR4)". In: *arXiv e-prints*, arXiv:2307.12546 (July 2023), arXiv:2307.12546. DOI: 10.48550/arXiv.2307.12546. arXiv: 2307.12546 [astro-ph.HE].

[48] T. P. Li and Y. Q. Ma. "Analysis methods for results in gamma-ray astronomy." In: *ApJ* 272 (Sept. 1983), pp. 317–324. DOI: 10.1086/161295.

[49] A. Donath, R. Terrier, Q. Remy, A. Sinha, et al. "Gammapy: A Python package for gamma-ray astronomy". In: *A&A* 678 (2023), A157. DOI: 10.1051/0004-6361/202346488. URL: https://doi.org/10.1051/0004-6361/202346488.

[50] A. Aguasca-Cabot, A. Donath, K. Feijen, L. Gréaux, et al. *Gammapy: Python toolbox for gamma-ray astronomy*. Version v1.1. June 2023. URL: https://zenodo.org/records/8033275.

[51] T. Unbehaun. *Private communication*. tim.unbehaun@fau.de. 2023.

[52] L. Ambrogi, S. Celli, and F. Aharonian. "On the potential of Cherenkov Telescope Arrays and KM3 Neutrino Telescopes for the detection of extended sources". In: *Astroparticle Physics* 100 (July 2018), pp. 69–79. DOI: 10.1016/j.astropartphys.2018.03.001. arXiv: 1803.03565 [astro-ph.HE].

Appendix A

Cut Criteria for the Nearby Spiral Galaxies

Three cut criteria are applied on the SGs from NEARGALCAT to get galaxies which are similar to the Andromeda Galaxy. The criteria are chosen in such a way to exclude most dwarf SGs, because some SGs are not labelled as dwarf galaxies. More precise cuts are not applied, because the Andromeda Galaxy is an outlier in the three categories and therefore this would result in almost no remainder galaxies.

The distribution of the parameter on which the cut is applied in reference to the galaxy's distance are shown in Figure A.1, Figure A.2 and Figure A.3 for the absolute magnitude, linear diameter and mass, respectively.

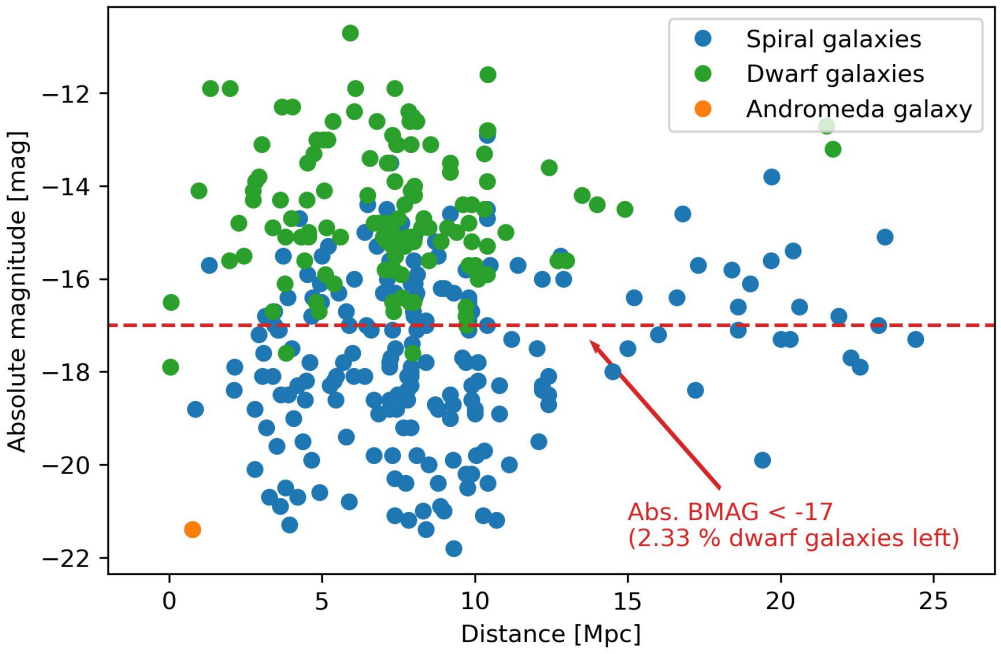

Figure A.1: Distribution of the absolute magnitude values in reference to the galaxy's distance are shown. Shown are all SGs in blue the SGs labelled as dwarf galaxies in green and the Andromeda Galaxy as a reference in orange. The cut criterium for the absolute magnitude is shown as a red dotted line. Every galaxy above the line is excluded.

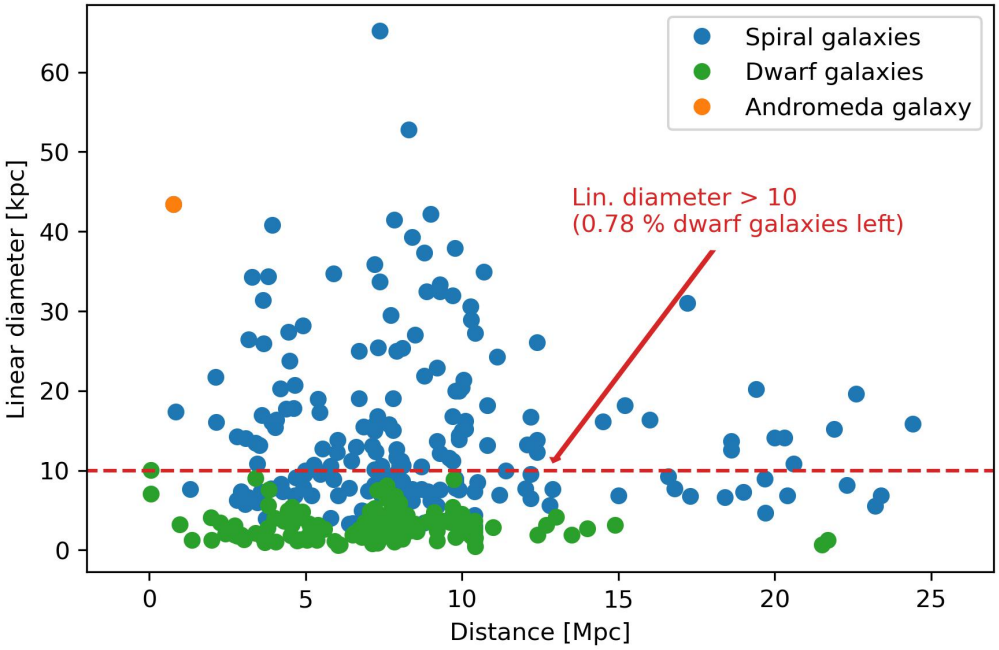

Figure A.2: Distribution of the linear diameter values in reference to the galaxy's distance are shown. Shown are all SGs in blue the SGs labelled as dwarf galaxies in green and the Andromeda Galaxy as a reference in orange. The cut criterium for the linear diameter is shown as a red dotted line. Every galaxy below the line is excluded.

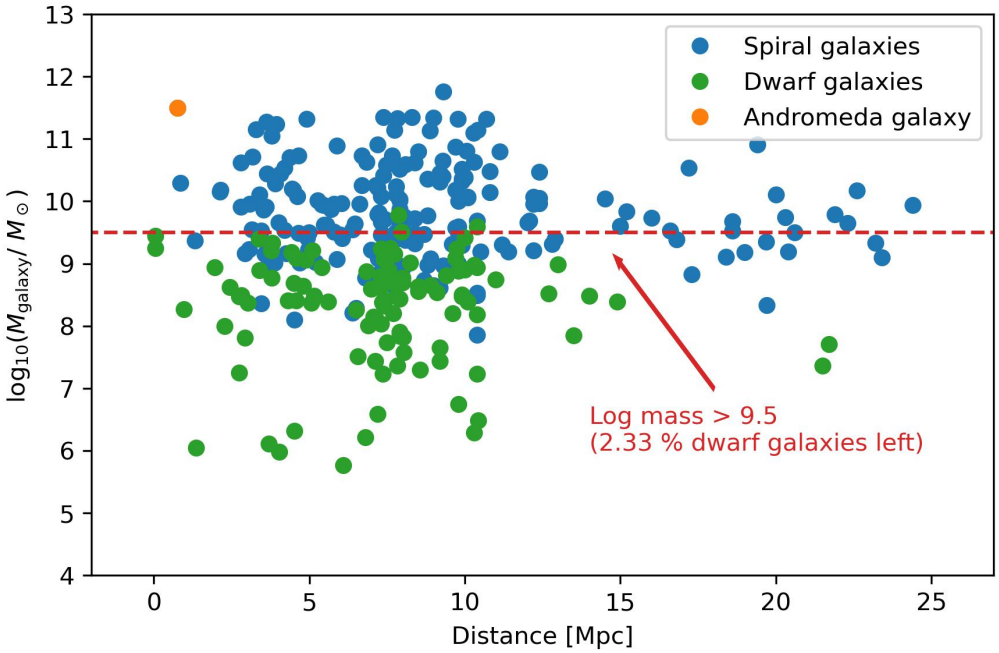

Figure A.3: Distribution of the mass values in reference to the galaxy's distance are shown. Shown are all SGs in blue the SGs labelled as dwarf galaxies in green and the Andromeda Galaxy as a reference in orange. The cut criterium for the mass is shown as a red dotted line. Every galaxy below the line is excluded.

Appendix B

Leptonic Source Spectrum Components

As discussed in subsection 2.1.2 can a leptonic source produce gamma rays with three different mechanism. The simulation with `Gamera` can calculate the portion each mechanism has on the total flux. In Figure B.1 the flux for the SH is calculated for the leptonic case with the singular fluxes resulting from the distinct production mechanism. The flux resulting from synchrotron radiation is not shown, because it falls off at lower energies and therefore contributes nothing to the total flux. One can see that in the energy range from 1 GeV to 100 GeV the ICS is dominant.

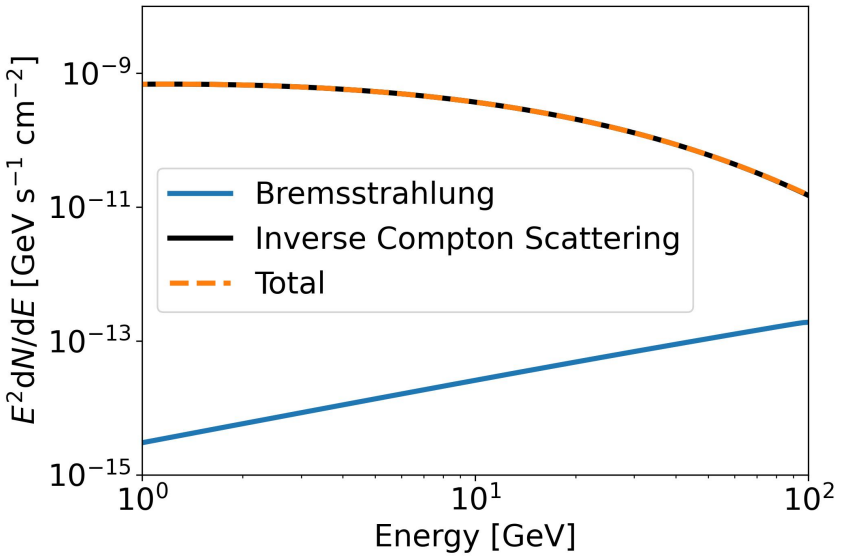

Figure B.1: Gamma-ray spectra resulting from a leptonic source, where the resulting spectra for each distinct production mechanism and the total is shown. The synchrotron radiation is not shown, because the flux drop too much at lower energies.

Appendix C

Fit Results for Remainder Models

C.1 M31

In the following section resulting fit parameter for the SH of M31 with a PWL-model (see Table C.1) and EXP-model (see Table C.2) are shown.

Parameter	Initial Value	Fit (fixed radius)	Fit (free radius)
Power Law Spectral Model			
ϕ_0 $[10^{-12}\,\mathrm{MeV\,cm^{-2}\,s^{-1}}]$	6.7032	3.9 ± 1.0	4.0 ± 1.0
E_0 [GeV]	1	-	-
Γ	1.9	2.23 ± 0.16	2.24 ± 0.16
Disk Spatial Model			
longitude (icrs)	$10°49'22''$	-	-
latitude (icrs)	$41°14'29''$	-	-
radius [°]	8.86	8.86	8.983 ± 0.011
Galactic Background			
norm	0.8972	0.969 ± 0.006	0.972 ± 0.006
tilt $[10^{-2}]$	1.353	4.8 ± 0.6	4.4 ± 0.6
E_0 [GeV]	1	-	-
Isotropic Background			
norm	1.224	1.00 ± 0.08	0.999 ± 0.006
tilt $[10^{-2}]$	0	2.9 ± 1.3	2.90 ± 0.11
E_0 [TeV]	1	-	-

Table C.1: Model parameter values for the spectral PWL-model, the disk spatial model and the two background models. Given are the initial values, the values after the fit with a fixed radius (8.86°) and after the fit with the radius as a free parameter.

Parameter	Initial Value	Fit (fixed radius)	Fit (free radius)
Exponential Cutoff Power Law Model			
ϕ_0 $[10^{-12}\,\mathrm{MeV\,cm^{-2}\,s^{-1}}]$	6.7032	4.2 ± 1.2	4.4 ± 1.2
E_0 [GeV]	1	-	-
λ $[\mathrm{GeV}^{-1}]$	8.6207×10^{-2}	$(1.724 \pm 0.007) \times 10^{-1}$	$(1.724 \pm 0.002) \times 10^{-1}$
α	1	-	-
Disk Spatial Model			
longitude (icrs)	$10°49'22''$	-	-
latitude (icrs)	$41°14'29''$	-	-
radius [°]	8.86	8.86	9.01 ± 0.24
Galactic Background			
norm	0.8972	0.971 ± 0.006	0.971 ± 0.006
tilt $[10^{-2}]$	1.353	4.7 ± 0.6	4.7 ± 0.6
E_0 [GeV]	1	-	-
Isotropic Background			
norm	1.224	1.05 ± 0.08	1.05 ± 0.07
tilt $[10^{-2}]$	0	2.1 ± 1.3	2.1 ± 1.1
E_0 [TeV]	1	-	-

Table C.2: Model parameter values for the spectral EXP-model, the disk spatial model and the two background models. Given are the initial values, the values after the fit with a fixed radius (8.86°) and after the fit with the radius as a free parameter.

C.2 M33

In the following section resulting fit parameter for the SH of M33 with a PWL-model (see Table C.3) and EXP-model (see Table C.4) are shown.

Parameter	Initial Value	Fitt (fixed radius)	Fit (free radius)
Power Law Spectral Model			
ϕ_0 $[10^{-12}\,\mathrm{MeV\,cm^{-2}\,s^{-1}}]$	6.7032	0.52 ± 0.15	0.46 ± 0.13
E_0 [GeV]	1	-	-
Γ	1.9	2.39 ± 0.24	2.30 ± 0.21
Disk Spatial Model			
longitude (icrs)	$23°27'43''$	-	-
latitude (icrs)	$30°39'37''$	-	-
radius [°]	1.0	1.0	1.053 ± 0.016
Galactic Background			
isotropic norm	0.9216	1.024 ± 0.020	1.024 ± 0.020
isotropic tilt $[10^{-2}]$	-1.112	6.8 ± 1.3	6.8 ± 1.3
E_0 [GeV]	1	-	-
Isotropic Background			
galactic norm	1.175	1.0 ± 0.1	1.0 ± 0.1
galactic tilt $[10^{-2}]$	0	2.5 ± 1.7	2.5 ± 1.7
E_0 [TeV]	1	-	-

Table C.3: Model parameter values for the spectral PWL-model, the disk spatial model and the two background models. Given are the initial values, the values after the fit with a fixed radius (1.0°) and after the fit with the radius as a free parameter.

Parameter	Initial Value	Fitt (fixed radius)	Fit (free radius)
Exponential Cutoff Power Law Model			
ϕ_0 $[10^{-12}\,\mathrm{MeV\,cm^{-2}\,s^{-1}}]$	6.7032	0.49 ± 0.14	0.42 ± 0.15
E_0 [GeV]	1	-	-
λ $[\mathrm{GeV}^{-1}]$	8.6207×10^{-2}	$(1.724 \pm 0.006) \times 10^{-1}$	$(1.724 \pm 0.004) \times 10^{-1}$
α	1	-	-
Disk Spatial Model			
longitude (icrs)	$23°27'43''$	-	-
latitude (icrs)	$30°39'37''$	-	-
radius [°]	1.0	1.0	1.055 ± 0.024
Galactic Background			
isotropic norm	0.9216	1.025 ± 0.020	1.025 ± 0.020
isotropic tilt $[10^{-2}]$	-1.112	6.9 ± 1.3	7.0 ± 1.3
E_0 [GeV]	1	-	-
Isotropic Background			
galactic norm	1.175	1.0 ± 0.1	1.0 ± 0.1
galactic tilt $[10^{-2}]$	0	2.3 ± 1.7	2.3 ± 1.7
E_0 [TeV]	1	-	-

Table C.4: Model parameter values for the spectral EXP-model, the disk spatial model and the two background models. Given are the initial values, the values after the fit with a fixed radius (1.0°) and after the fit with the radius as a free parameter.

Acknowledgement

Finally, I would like to express my gratitude to all those who have supported me during the preparation of this thesis and throughout my studies. In particular, I would like to thank:

- Dr. Alison Mitchell for providing the interesting topic and for supervising the entire Master's thesis
- Katrin Streil for supervising me throughout the whole time, being ready to help me with every problem and for proofreading my thesis
- Tim Unbehaun and Tina Wach for helping me with every fermipy problem I had
- Dr. Johannes Schäfer for helping me with every minor problem and for proofreading my thesis
- Anna Eimer, Pedro Silva Batista, Bastian Setter and Martin Schneider for also proofreading my thesis
- Christian Elflein for being a nice office mate from another office with weird video game taste
- Matheus Genaro Dantas Xavier for being a nice office mate with very good video game taste
- Timo Nesser for always reminding me that the One Piece is real
- Dr. Samuel Spencer, Karen Terveer, Janna Vischer, Phillip Laub and Frederik Andersen for spending time with regularly me at the coffee breaks
- Every other person from the gamma-ray group in the ECAP in general for providing a nice environment

Erklärung

Ich erkläre hiermit an Eides statt, dass ich die vorliegende Arbeit selbständig verfasst und dabei keine anderen als die angegebenen Hilfsmittel benutzt habe. Sämtliche Stellen der Arbeit, die im Wortlaut oder dem Sinn nach Publikationen oder Vorträgen anderer Autoren entnommen sind, habe ich als solche kenntlich gemacht.

Erlangen, November 15, 2023 Mario Engelmann